

ROBUST CARRIER PHASE DGPS NAVIGATION
FOR SHIPBOARD LANDING OF AIRCRAFT

BY

MOON BEOM HEO

Submitted in partial fulfillment of the
requirements for the degree of
Doctor of Philosophy in Mechanical and Aerospace Engineering
in the Graduate College of the
Illinois Institute of Technology

Approved _____
Adviser

Chicago, Illinois
December 2004

ACKNOWLEDGEMENTS

First and foremost, I would like to thank my advisor, Professor Boris S. Pervan, for providing me opportunity, guidance, encouragement and support during the entire period of my doctorate work. He led me into the great field of GPS-based Navigation and taught me how to do research as an engineer. I am fortunate to have him as my mentor. I believe that the training under his supervision will benefit my engineering career for life. I can't find any words to express all of my appreciation to him. I would also like to thank my defense and reading committees, including Professor Nair, Professor Dix, Professor Qian, and Professor Kallend, for their careful reading and helpful advice on this thesis.

I would like to thank Navigation and Guidance Laboratory members, Fang-Chen Chan, Livio Gratton, Mathieu Joerger, Samer Khanafseh, Bart Kempny, and former members John Andreacchi, Irfan Sayim, as well as John Christ for their friendship and valuable insights.

I would like to thank my parents Seung-Moo and Soon-Ja Heo, for their support and motivation during my Ph.D. study. Finally, I would like to thank my wife, Shinyoung, and daughter Jennifer and Sarah for advice and encouragement. Their patience and love made this dissertation possible.

TABLE OF CONTENTS

	Page
ACKNOWLEDGEMENTS	iii
LIST OF TABLES	vii
LIST OF FIGURES	viii
LIST OF SYMBOLS	xi
LIST OF ABBREVIATIONS	xii
ABSTRACT	xiii
CHAPTER	
1. INTRODUCTION	1
1.1 Global Positioning System	1
1.2 Shipboard Relative GPS	5
1.3 Previous Works	9
1.4 Contributions	12
2. CARRIER PHASE DIFFERENTIAL GPS	14
2.1 Carrier Phase Differential GPS	14
2.2 Dual Frequency CDGPS	25
2.3 Cycle Ambiguity Estimation	29
2.4 Real-Time CDGPS Kinematic Positioning Algorithm	30
2.5 Real-Time CDGPS Static Positioning Algorithm	34
2.6 CDGPS Test Results	38
3. CYCLE SLIP DETECTION	42
3.1 Introduction	42
3.2 RAIM-based Fault Detection	43
3.3 Single Frequency Architecture	45
3.4 Dual Frequency Architecture	53
3.5 Summary of Cycle Slip Detection	55
4. EPHEMERIS ERROR DETECTION	57
4.1 Introduction	57
4.2 Limit Case 1	59

CHAPTER	Page
4.3 Limit Case 2	61
4.3 Availability of Ephemeris Error Detection	64
4.5 Summary of Ephemeris Error Detection	67
5. IONOSPHERIC ERROR DETECTION	68
5.1 Introduction	68
5.2 Direct Observation Method	69
5.3 Effect of Ionospheric Gradient on Carrier Phase Positioning.....	71
5.4 Availability of Ionospheric Gradient Detection	72
5.5 Summary of Ephemeris Error Detection	75
6. ROBUST NAVIGATION ALGORITHM	78
6.1 Introduction	78
6.2 Geometry-Free Code-Carrier Filtering	79
6.3 Double Difference Widelane Landing	87
6.4 Double Difference Widelane Landing with Geometric Redundancy.....	93
6.5 Double Difference L1/L2 Landing with Geometric Redundancy	96
6.6 Experimental Results	102
6.7 Summary of Robust Navigation Algorithm.....	103
7. CONCLUSIONS.....	105
7.1 Autonomous Fault Detection	105
7.2 Robust Navigation Algorithm.....	106
7.3 Recommendation and Future Work	107
 APPENDICES	
A. BASIC RAIM CONCEPTS	109
B. COMPUTATION OF MISSED DETECTION PROBABILITY	112
C. RANGE MEASUREMENT ERROR DUE TO IONOSPHERIC GRADIENT	115
D. VARIANCE ESTIMATE	118
E. WIDELANE IONOSPHERE FREE ESTIMATION	121

APPENDICES	Page
F. WEIGHTED RAIM.....	125
G. AVAILABILITY OF EPHEMERIS ERROR DETECTION FOR DIFFERENT SHIP LOCATIONS	128
H. AVAILABILITY OF IONOSPHERIC ERROR DETECTION FOR DIFFERENT SHIP LOCATIONS	131
BIBLIOGRAPHY	134

LIST OF TABLES

Table	Page
3.1. GPS Constellation Availability.....	48
3.2. Summary of Cycle Slip Detection	56
4.1. Summary of Orbit Ephemeris Error Detection	67
5.1. Cycle Resolution and Effective Ranging Measurement Errors	71
5.2. Summary of Ionospheric Error Detection.....	77

LIST OF FIGURES

Figure	Page
1.1. The Global Positioning System (GPS).....	2
1.2. Three Segments of the GPS-based Navigation System.....	3
1.3. SRGPS Nominal Approach	7
1.4. ACLS Mode I Landing Sequence.....	8
2.1. DGPS Concept.....	17
2.2. Single Difference Sigma of Thermal Receiver Noise	20
2.3. Multipath and Receiver Noise (Double Difference).....	22
2.4. Doppler Effect on L1 Carrier Phase Measurement	24
2.5. Distance Estimation using CDGPS	39
2.6. 3-D Position Estimation Error	39
2.7. 2-D Kinematic Position Estimation.....	40
2.8. AGV CDGPS Kinematic Positioning Real-Time Test.....	41
3.1. RAIM Detection Thresholds	44
3.2. Normal Condition.....	45
3.3. Cycle Slip Occurs on a Single Channel.....	45
3.4 Basic RAIM Algorithm	46
3.5. Service Availability at Longitude at 60° E	49
3.6. Service Availability at Longitude at -60° E.....	50
3.7. Service Availability at Longitude at -135° E.....	50
3.8. Service Availability vs. Elevation Mask	51

Figure	Page
3.9. Service Availability vs. Required Probability of Cycle Slip Missed Detection	52
3.10. Availability vs. Measurement Error	52
3.11. Normal Condition.....	53
3.12. Cycle Slips Occur on L1 Channels 3 and 5	53
3.13. Differencing Between L1 and L2	54
4.1. Service Entry Point and Synthetic Baseline	58
4.2. Vertical Position Error Due to Orbit Ephemeris Error For Limit Case 1.....	60
4.3. Effect of Increasing α	61
4.4. Vertical Position Error Due to Orbit Ephemeris Error For Limit Case 2.....	62
4.5. Effect on RAIM of Increasing $x_0 - x_1$	63
4.6. Service Availability of Orbit Ephemeris Detection.....	65
4.7. x vs. x_0 for Limit Case 1	66
4.8. x_1 vs. x_0 for Limit Case 2	66
5.1. Illustrated Position Error Histories Due to Ionospheric Gradient	72
5.2. Service Availability vs. β	74
5.3. Constraint on Cycle Resolution Distance.....	76
5.4. Maximum Effective Cycle Resolution Distance Constraint.....	76
6.1. Availability vs. VDOP.....	83
6.2. Widelane Cycle Resolution	85
6.3. Availability of Double Difference Widelane, $\psi = 20$	91
6.4. Availability of Double Difference Widelane, $\psi = 30$	91
6.5. Availability of Double Difference Widelane, $\psi = 40$	92

Figure	Page
6.6. Availability of Double Difference Widelane using Geometric Redundancy, $\psi = 20$	94
6.7. Availability of Double Difference Widelane using Geometric Redundancy, $\psi = 30$	95
6.8. Availability of Double Difference Widelane using Geometric Redundancy, $\psi = 40$	95
6.9. Availability of Double Difference L1/L2 Carrier Phase using Geometric Redundancy, $\psi = 20$	98
6.10. Availability of Double Difference L1/L2 Carrier Phase using Geometric Redundancy, $\psi = 30$	99
6.11. Availability of Double Difference L1/L2 Carrier Phase using Geometric Redundancy, $\psi = 40$	99
6.12. Availability of Double Difference L1/L2 Carrier Phase using Geometric Redundancy at the North Pacific Ocean with $\psi = 30$	100
6.13. Availability of Double Difference L1/L2 Carrier Phase using Geometric Redundancy Near China with $\psi = 30$	101
6.14. Availability of Double Difference L1/L2 Carrier Phase using Geometric Redundancy at the Atlantic Ocean with $\psi = 30$	101
6.15. Widelane Integer Estimation	103
6.16. Geometry-Free Prefiltering Algorithm Diagram.....	104
G.1. Availability of Ephemeris Error Detection at Lat = 20° N and Long = 60° W	129
G.2. Availability of Ephemeris Error Detection at Lat = 5° N and Long = 135° W	130
G.3. Availability of Ephemeris Error Detection at Lat = 10° N and Long = 30° W.....	130
H.1. Availability of Ephemeris Error Detection at Lat = 5° N and Long = 135° W.....	132

Figure	Page
H.2. Availability of Ionospheric Error Detection at Lat = 20° N and Long = 60° W	133
H.3. Availability of Ionospheric Error Detection at Lat = 10° N and Long = 30° W	133

LIST OF SYMBOLS

Symbol	Definition
ϕ	Carrier Phase Measurement
PR	Code Phase Measurement
Δ	Difference between Measurements Once
$\nabla\Delta$	Difference between Measurements Twice
σ	Standard Deviation
e	Line of Sight Vector
N	Cycle Ambiguity Integer
τ	Receiver Clock Bias
I^i	Ionospheric Effect on Measurement for Satellite i
T^i	Tropospheric Effect on Measurement for Satellite i
λ	GPS Signal Wavelength
v	Measurement Noise
H	Geometry Matrix
C/N_o	Receiver Carrier to Noise Ratio
L1	L1 Frequency
L2	L2 Frequency
f	Frequency of GPS signal
r	Residual Vector
K_{ffd}	Integrity Multiplier
P	Covariance Matrix
ψ	Nondimensional Ratio
η	Local Index of refraction
$\Delta E_{doppler}$	Doppler Effect on Single Difference Measurement
c	Speed of Light
H^+	Pseudoinverse of H

LIST OF ABBREVIATIONS

Abbreviation	Definition
ACLS	Automatic Carrier Landing System
ARNS	Aeronautical Radio Navigation Services
AGV	Autonomous Ground Vehicle
CDGPS	Carrier Phase Differential Global Positioning System
CONUS	Conterminous United States
DGPS	Differential Global Positioning System
DH	Decision Height
FAA	Federal Aviation Administration
FMS	Failure Mode Slope
GPS	Global Positioning System
ILS	Instrument Landing System
JPALS	Joint Precision Approach and Landing System
LAAS	Local Area Augmentation System
LCCS	Landing Control Central System
LDGPS	Local Differential GPS
MCS	Master Control Station
NGL	Navigation and Guidance Laboratory
PPS	Precise Position Service
RAIM	Receiver Autonomous Integrity Monitoring
RHCP	Right-Hand Circularly Polarized
SPS	Standard Positioning Service
SRGPS	Shipboard Relative GPS
TEC	Total Electron Contents
VAL	Vertical Alert Limit
VPL	Vertical Protection Level
VDOP	Vertical Dilution of Precision
WAAS	Wide Area Augmentation System

ABSTRACT

Shipboard-Relative GPS (SRGPS) is an architectural variant of the Joint Precision Approach and Landing System (JPALS) that will provide high accuracy and high integrity differential GPS (DGPS) navigation for automatic shipboard landings. It is required that the vertical position error be bounded to 1.1 m with an associated integrity risk of 10^{-7} . Because of the stringent nature of these specifications, carrier phase DGPS (CDGPS) solutions are being pursued.

In this dissertation, prototype algorithms for a high accuracy and integrity CDGPS precision approach and landing system are described in detail. It consists of two fundamental components, which are the airborne autonomous fault detection algorithm and the terminal navigation algorithm.

The first part of this dissertation focuses on airborne integrity algorithms for Shipboard Relative GPS (SRGPS) navigation. Airborne autonomous detection is required for navigation threats that are undetectable by integrity monitors at a shipboard differential reference station. These threats can be separated into two basic categories: (1) aircraft receiver failures, and (2) signal-in-space anomalies whose effects depend on the displacement between the user and the ship. For the anticipated carrier phase SRGPS navigation architecture, tracking loop cycle slips are well-known threats in the first category. Ionospheric gradient and satellite orbit ephemeris anomalies are relevant threats of the second type. Airborne autonomous monitor algorithms designed to detect these threats are described in this dissertation. Monitor performance is directly evaluated relative to the integrity requirements for aircraft shipboard landing navigation applications.

The second part of this dissertation focuses on the design of robust airborne algorithms for SRGPS terminal navigation. In this context, a processing methodology is defined to optimally combine the complementary benefits of geometry-free filtering and geometric redundancy. Specifically, when the aircraft is far from the ship (inside or outside the SRGPS service volume), geometry-free filtering is used for cycle estimation of widelane integers. For dual frequency implementations, the advantage of code/carrier divergence-free filtering prior to SRGPS service volume entry can be especially significant because long filter durations can be used. In this dissertation, the robust navigation architecture is detailed, and necessary and sufficient conditions are defined to ensure navigation performance for shipboard landing of aircraft.

CHAPTER 1

INTRODUCTION

1.1 Global Positioning System

The Global Positioning System (GPS) is a passive satellite-based radio navigation system for military and civil users (Figure 1.1). GPS consists of three segments [Parkinson96]*: the space segment, the control segment and the user segment, shown in Figure 1.2. The space segment consists of a nominal constellation of 24 satellites [Spilker94] with four satellites in each of six orbit planes having inclinations of 55 degrees. Each orbit is nearly circular with a period of 11.97 hours and a nominal altitude of approximately 20,000 km. The control segment consists of five monitor stations, four ground antenna upload stations, and an Operational Control Center. The objectives of the ground segment include maintaining each satellite in its proper orbit, generating and uploading navigation data to each satellite, and keeping the satellite clock error within requirements. The user segment includes all user receivers. These user receivers track the ranging signal of selected satellites and calculate user positions.

GPS satellites broadcast the ranging signals along with navigation data in two different frequency bands: a primary signal centered at 1575.42 MHz (L1) and a secondary signal centered at 1227.6 MHz (L2). The L1 signal is modulated with a Coarse/Acquisition code (C/A) and a Precision code (P or Y) in phase quadrature. The L2 signal is modulated with P(Y) code. Civil users can only access C/A code because P(Y)

* Corresponding to the Bibliography

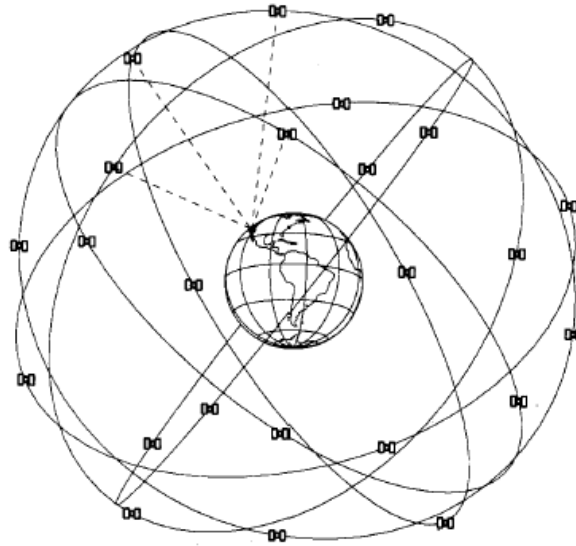


Figure 1.1. The Global Positioning System (GPS)

code is restricted to military uses (based on national security considerations). Both the L1 and L2 frequencies are also modulated with navigation data (50 bps) which include satellite orbit ephemerides. The services provided by C/A and P(Y) codes are called the Standard Position Service (SPS) and the Precise Position Service (PPS), respectively.

A multi-channel digital signal processing function is typically used in a receiver for GPS signal processing. Each digital signal channel is dedicated to a single satellite and consists of a delay-lock loop (DLL) and a phase-lock loop (PLL). The DLL generates an estimate of the code phase (pseudorange) and delivers a punctual C/A code signal to the PLL for reconstruction of the incoming carrier. The PLL provides a phase-locked carrier to the DLL for coherent detection of the modulated C/A code and generates an estimate of the carrier phase.

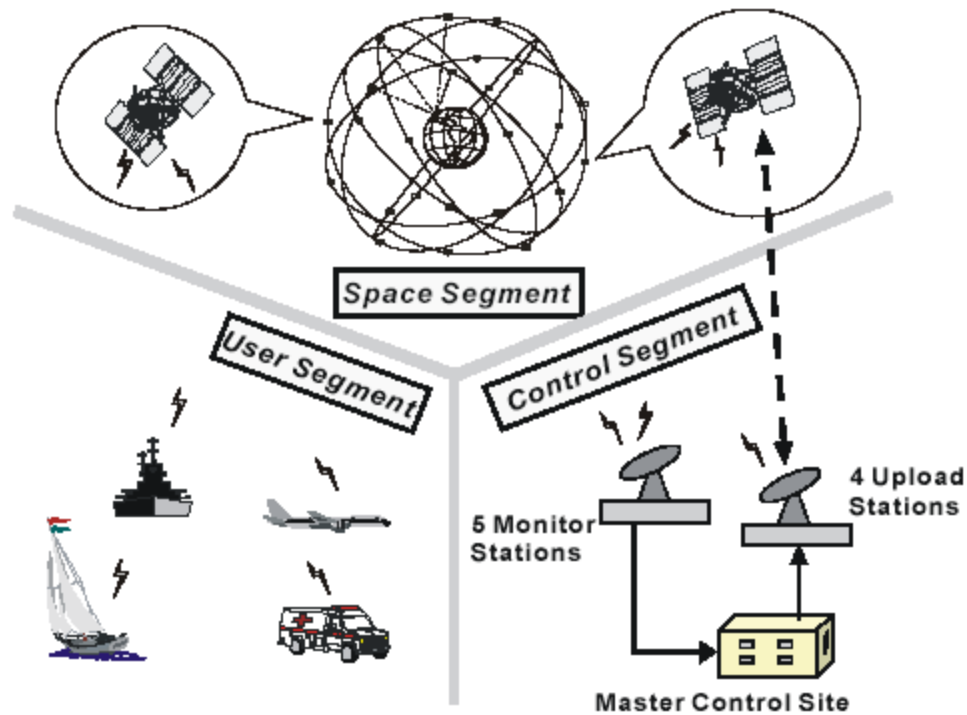


Figure 1.2. Three Segments of the GPS-based Navigation System

The precision of code phase measurements is typically 0.5-1 m (the code chip length of 300 m). In contrast, because of the much smaller wavelength of the carrier (19 cm for L1), carrier phase measurement precision at the millimeter-level is possible.

The carrier measurement contains the measured fractional cycle and the integer number of cycles between the receiver and the satellite. However, when the receiver acquires the GPS signal, it provides no information regarding the correct integer number of cycles. The unknown integer is known as a cycle ambiguity, and the process of its estimation is known as cycle ambiguity resolution.

A user can estimate his position (three unknown states) by obtaining ranges to the GPS satellites in view. The range from the satellite is found by measuring the transit time

of the signal being broadcast. However, because the receiver clock is not precisely synchronized to the satellite clocks, the clock bias must be treated as an additional unknown state in position estimation. Consequently, the user must have four or more satellites in view to resolve the state vector--three for user position states and one for the clock bias state.

In order to improve the accuracy and integrity of SPS, the differential GPS (DGPS) technique was proposed and developed [Beser82, Teasley80] in the early 1980s. The concept of DGPS is based on using the correlation in ranging errors between a reference station receiver and DGPS user receivers to eliminate co-existing ranging errors in the user ranging measurement. Usually DGPS applications require a surveyed location for the reference station. This reference station estimates the slowly varying measurement errors and forms a ranging correction for each satellite in view. The correction is broadcast to all DGPS users in an operational service radius centered at the reference station. This differential correction greatly improves accuracy for all DGPS users within the service radius. However, there are some limitations to DGPS. Because the reference station is geographically separated from the user, these corrections are not the exact corrections for users' ranging errors. The differences between reference ranging corrections and user ranging errors are called differential ranging errors. The Local Area Augmentation System (LAAS) is an example of using the DGPS concept [MASPS98]. The LAAS is an aircraft precision landing system being developed by the Federal Aviation Administration (FAA) with the objective of replacing the current Instrument Landing System (ILS).

1.2 Shipboard Relative GPS

The Joint Precision Approach and Landing System (JPALS) is designed to enable U.S. military forces to be highly mobile and capable of "rapid response" on a global basis to a wide range of military scenarios. Similar in concept to the civilian LAAS, JPALS will be based on differential Global Positioning System technology. Aircraft will receive ranging and navigation data from the satellite and differential ranging data or corrections from a ground/shipboard station via data link.

The JPALS consists of two programs, which are Local Differential GPS (LDGPS) and Shipboard Relative GPS (SRGPS). The LDGPS program supports multiple types of operations: fixed base (permanent installations), tactical (rapid deployment to existing airstrips), and special mission (transportable to remote locations). SRGPS is designed for shipboard operations. JPALS must provide this support in a potentially hostile environment.

1.2.1 Shipboard Relative GPS. SRGPS is being developed to provide DGPS navigation for automatic shipboard landings in zero-visibility conditions and will replace the existing automatic shipboard landing system, Automatic Carrier Landing System (ACLS). While the system promises great practical benefit, a number of key technical challenges must first be addressed. Foremost among these is the need to ensure compliance with stringent requirements for SRGPS navigation integrity. The required vertical protection level for the navigation system is 1.1 m, with an associated integrity risk of approximately 10^{-7} [JPALSTPWG]. It is desired that these integrity requirements be satisfied with a system availability of at least 99.7 percent for the nominal case when

dual frequency signals are available [ORD]. In the event of interference or jamming on one frequency, the target availability is 95 percent. Unlike landing on a ground airport, the shipboard (aircraft carrier) landing requires higher accuracy because of the ship's mobility. Because of the stringent nature of these specifications and the ship motion conditions, *carrier phase* DGPS (CDGPS) (see Chapter 2) solutions are being pursued. The nominal aircraft approach for SRGPS is illustrated in Figure 1.3.

1.2.2 Automatic Carrier Landing System. The Automatic Carrier Landing System is the current aircraft precision approach and landing system used by the US navy in shipboard environments [AFCS]. ACLS consists of two main components, which are the Landing Control Central System (LCCS) and Instrument Landing System (ILS) radars. The LCCS radar system tracks the aircraft using a conical scan antenna and compares the aircraft position to the desired glide path. ILS radar transmits the glide path from the ship to the aircraft. ILS uses two antennas that transmit the azimuth and elevation information, respectively.

During an ACLS operation, the pilot can select one of three options: Mode I, Mode II, or Mode III. Mode I (see Figure 1.4) is a fully automatic approach from entry point to touchdown. Mode II occurs when the pilot controls the aircraft using the cockpit display. Mode III is when the pilot controls the aircraft aided by a shipboard controller using verbal information. Nominally, the pilot can use Mode I with Modes II and III as backups.

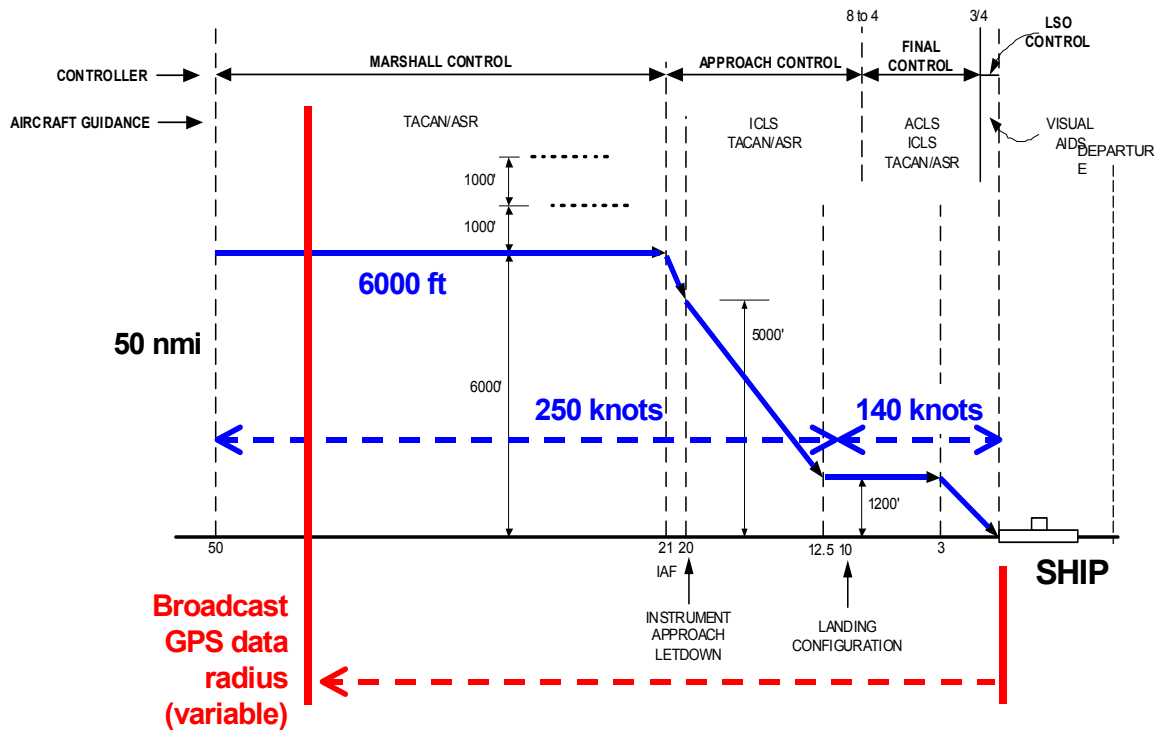


Figure 1.3. SRGPS Nominal Approach

Mode I landing begins when the aircraft is at the marshal point where the data link channel is assigned. As the aircraft passes the acquisition radar window (4 miles away from the ship), LCCS radar acquires the aircraft. Then, LCCS begins sending vertical and lateral error signals, which are the displacement from the actual aircraft approach path. The aircraft is coupled with the LCCS for automatic approach and landing. For the integrity monitoring system, ACLS uses the ILS radar system to independently check the LCCS flight path progress. If a large maneuver is required of the aircraft to bring it back on course, the ground controller sends a wave-off message.

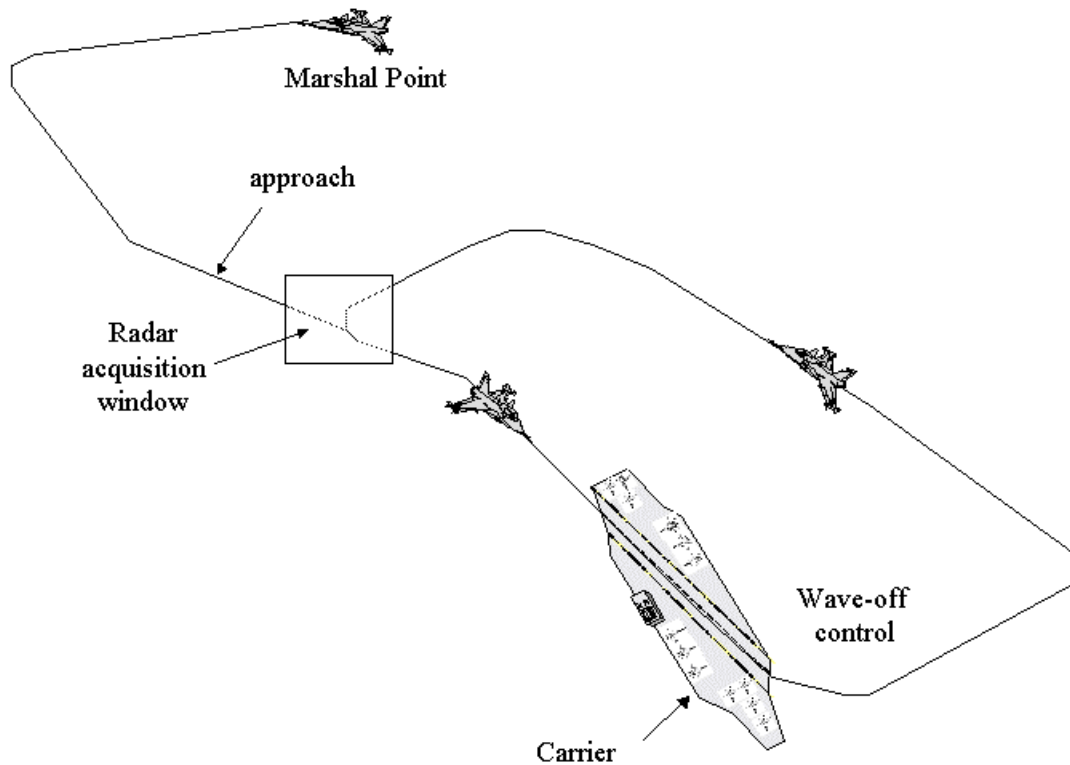


Figure 1.4. ACLS Mode I Landing Sequence

1.2.4 Shortcomings of Existing System. Existing systems do not satisfy JPALS requirements because they have a number of shortcomings and limit joint operations. The deficiencies of existing systems are summarized as follows [PALC]:

1. Current systems are manpower intensive and require extensive training of operators and/or support personnel.
2. Current systems have limited rapid deployment capability, are difficult to transport, require extended periods of time to set up, and require favorable weather conditions during assembly and system checkout.

3. Current precision approach systems do not provide covert, jam-resistant, data transmission and reception capability.
4. Vulnerability of current systems in hostile areas is very high.
5. The variety of systems in use makes it difficult to realize logistics and support savings and results in higher life cycle costs as systems are upgraded.

In this context, GPS-based aircraft navigation system, spanning all aspects of flight, is attractive as a new aircraft precision approach and landing system. It can provide seamless aircraft navigation, from takeoff to touchdown, with low cost and high availability.

1.3 Previous Work

A significant amount of work has been done toward improving GPS-based aircraft precision approach and landing systems. These accomplishments were made possible through the utilization of the DGPS concept with carrier phase measurements and advanced integrity monitoring systems.

1.3.1 Receiver Autonomous Integrity Monitoring (RAIM). RAIM is a well-known approach to GPS fault detection, which can be effective against many different types of failures. The RAIM concept is based on the verification of the consistency of redundant satellite measurements by the GPS user. In 1988, Parkinson and Axelrad introduced the least-squares pseudorange residual as a test statistics for the fault detection and isolation [Parknson88]. In the same year, Sturza formalized the residual-based approach using parity space methodology [Sturza88]. In 1995, Walter [Walter95]

developed “Weighted RAIM.” In this method, a priori information to weight certain satellites over other satellites was used. In 1996, Pervan [Pervan96] generalized RAIM for application to carrier phase cycle ambiguity resolution. He also introduced a new parity space algorithm to provide the capability for high integrity failure isolation.

1.3.2 Cycle Slip Detection. Important prior cycle slip (see Chapter 3) detection work was focused on the use of geometry-free linear combinations of available observables to test for abrupt discontinuities in the measurements. For example, Blewitt [Blewitt90] used the undifferenced geometry-free phase to detect cycle slips, whereas Gao [Gao99] and Bisnath [Bisnath00] used the double difference widelane carrier phase (see Section 6.3) minus narrowlane pseudorange (see APPENDIX E) for this purpose. Both of these approaches require extensive filtering to detect cycle slips with high integrity.

1.3.3 Ground Based Ephemeris Error Detection. In 2003, Pervan [Pervan03a] proposed a real-time ephemeris integrity monitoring system based on the use of carrier-phase ranging measurements made by two or more ground-based reference receivers separated by short baselines. A dual-frequency, geometry-free widelane approach was used to resolve cycle ambiguities present in the carrier-phase measurements. These results were applicable for LAAS Category II and III landings. (Details of LAAS Category I, II and III are described in [ORDLAAS].) Gratton [Gratton04], in 2004, provided a new ephemeris monitoring method for LAAS Category I. His work included

the verification of the consistency of new and old ephemeris messages, and measurement-based detection.

1.3.4 Ionospheric Error Detection. Most prior works in this area were based on characterization of the random properties of the ionospheric effect on GPS measurement such as Total Electron Contents (TEC). However, this work is mainly applicable to the Wide Area Augmentation System (WAAS). The WAAS was commissioned by the Federal Aviation Administration (FAA), and started operations over a large part of the Conterminous United States (CONUS) on July 10, 2003.

In 1999, Christie, et al. [Christie99] analyzed the effect of differential ionospheric gradient on the Carrier Smoothed Code Algorithm (CSC) for LAAS. In 2002, Luo [Luo02] focused precisely on the code-carrier divergence monitoring system for ionospheric error detection.

1.3.5 Precision Approach and Landing. In 1993, Paielli, et al. at NASA Ames [Paielli93], Van Grass, et al. of Ohio University [Van Grass93], and Romrell, et al., in 1995, at E-System [Romrell95], independently applied differential carrier phase coupled with an ‘on-the-fly’ (OTF) cycle resolution algorithm for a series of test flights. In 1994, Cohen [Cohen93] applied the Integrity Beacons Landing System (IBLS) to aircraft precision landing for high integrity real-time cycle ambiguity resolution. In 1999, Hwang [Hwang99] proposed that the effect of prior measurement filtering can be especially important because long filter time constants can be used. In 2003, Pervan [Pervan03b]

evaluated the performance of single- and dual-frequency architectures for both floating-ambiguity and fixed-integer carrier-phase differential GPS (DGPS) navigation.

1.4 Contributions

Despite the impressive accomplishments and efforts, the described previous works do not satisfy the stringent requirements of the aircraft precision approach and landing system in shipboard environment.

This dissertation is focused on the airborne navigation algorithm for SRGPS. It is divided into two parts: the airborne autonomous fault detection algorithm and the robust navigation algorithm. Specific contributions were made in the following areas:

1. The effectiveness of carrier phase Receiver Autonomous Integrity Monitoring (RAIM) for cycle slip detection was explored. Single and multiple channel cycle slip threat models were considered for both single and dual frequency SRGPS architectures. The traditional RAIM concept was extended by applying integer and half-integer constraints on failure magnitude, and the detection algorithm proposed was shown to be effective both before and after cycle ambiguity resolution. In addition, the availability of the RAIM-based cycle slip detection function was directly evaluated in this work (Chapter 3).
2. The carrier phase RAIM was developed to detect the ephemeris error. The basis for observability of ephemeris failures using RAIM is that the magnitude of the residual test statistic will change proportionally during an approach as the distance between the aircraft and ship decreases. The effectiveness of such a

‘relative’ RAIM method is therefore dependent on the magnitude of the observed change in the test statistic, which in turn is dependent on total change in displacement during the approach within the SRGPS service radius. In this dissertation the autonomous ephemeris detection algorithm is described in detail, and the minimum SRGPS service radius to ensure effectiveness of the monitor is quantified (Chapter 4).

3. The carrier phase measurements were used to directly detect anomalous ionospheric gradients in real time during the aircraft approach. In this work, we consider an ionospheric threat model consisting of an anomalously large, constant spatial gradient during the approach for SRGPS. The effectiveness of relative RAIM and direct detection algorithms with respect to these threat models is explicitly quantified in this work (Chapter 5).
4. Robust airborne algorithms for SRGPS terminal navigation were designed, implemented and tested. In this context, a processing methodology was defined to optimally combine the complementary benefits of geometry-free filtering and geometric redundancy. Specifically, when the aircraft is far from the ship (inside or outside the SRGPS service volume), geometry-free filtering was used for cycle estimation of widelane integers. For dual frequency implementations, the advantage of code/carrier divergence-free filtering prior to SRGPS service volume entry can be especially significant because long filter durations can be used (Chapter 6).

CHAPTER 2

CARRIER PHASE DIFFERENTIAL GPS

2.1 Carrier Phase Differential GPS

SRGPS uses the DGPS concept, but the reference station broadcasts its GPS measurements directly rather than the computed differential correction. These GPS measurements are actually carrier phase measurements. Although the DGPS eliminates the common errors, the cycle ambiguities still remain. These cycle ambiguities must be resolved before the carrier can be used directly for positioning.

If cycle ambiguities are resolved, the carrier phase DGPS enables centimeter level user navigation accuracy. Such performance is possible since carrier ranging measurement errors are normally very small (typically sub-centimeter), but its realization is dependent on the successful resolution of cycle ambiguities corresponding to the GPS satellites in view. The following sections will explain the details of carrier phase DGPS and some details of its specific application to SRGPS.

2.1.1 Carrier Phase Observable. The raw carrier phase GPS measurement is the sum of the true range to the satellite, the cycle ambiguity and a number of error sources, which are the satellite and receiver clock bias, the spatial decorrelation errors and measurement noise, etc. At a given time index, k , the carrier phase measurement, ϕ_k^i , for satellite i can be expressed as

$$\lambda_{L1}\phi_k^i = \rho_k^i + \tau_{R,k} + \tau_k^i + \lambda_{L1}N^i - I_k^i + T_k^i + v_k^i \quad (2.1)$$

where,

ϕ_k^i is the carrier phase observable for the satellite i at an arbitrary GPS time k ,

λ_{L1} is the wavelength of the L1 frequency,

ρ_k^i is the true range between phase center of the antenna and satellite i ,

$\tau_{R,k}$ is the receiver clock offset from nominal GPS time,

N^i is the integer cycle ambiguity for satellite i ,

τ_k^i is the clock offset of satellite i from nominal GPS time at the time of signal transmission,

I_k^i is the carrier phase advance due to free electrons in the ionosphere along the signal path,

T_k^i is the carrier phase delay due to tropospheric refraction, and

v_k^i is the error due to multipath and receiver noise ($\sim N(0, \sigma_{\Delta\phi, L1}^2)$).

Equation (2.1) is expressed in units of meters, and λ_{L1} is defined as c/f_{L1} , where c is the vacuum speed of light and f_{L1} is the frequency of L1 measurements.

2.1.2 Differential Carrier Phase Observable. The basic concept of CDGPS is that the reference and the user receive the signal from a given GPS satellite, and then the reference station broadcasts its measurement to the user as shown in Figure 2.1. The user computes a ‘single difference’ phase by taking the difference between the user and reference carrier phase measurements at time k from GPS satellite i . The mathematical expression of single difference carrier phase is following:

$$\lambda_{L1} \Delta \phi_{L1,k}^i = -e_k^{iT} x_k + \Delta \tau_k + \lambda_{L1} \Delta N_{L1}^i - \Delta I_k^i + \Delta T_k^i + \Delta v_k^i \quad (2.2)$$

where,

e_k^i is the line of sight (unit) vector to satellite i ,

x_k is the displacement vector from the reference station to the user,

ΔN_{L1}^i is the single difference cycle ambiguity (integer),

$\Delta \tau_k$ is the single difference receiver clock bias,

ΔI_k^i is the single difference carrier phase advance due to free electrons in the ionosphere along the signal path,

ΔT_k^i is the single difference carrier phase delay due to tropospheric refraction, and

Δv_k^i is the single difference measurement error (typically sub-centimeter).

The single difference carrier phase results in elimination of the satellite clock bias. But the rest of the terms still remain in single difference form. Among the single difference error sources, the receiver clock bias can be eliminated by the difference in the single difference measurements between two given satellites. This is known as the ‘double difference.’ The double difference carrier phase measurement is the sum of the double difference range, the double difference cycle ambiguity, the double difference spatial decorrelation errors, and the double difference measurement noise. Equivalently, the receiver clock bias can be eliminated by direct estimation using single difference form.

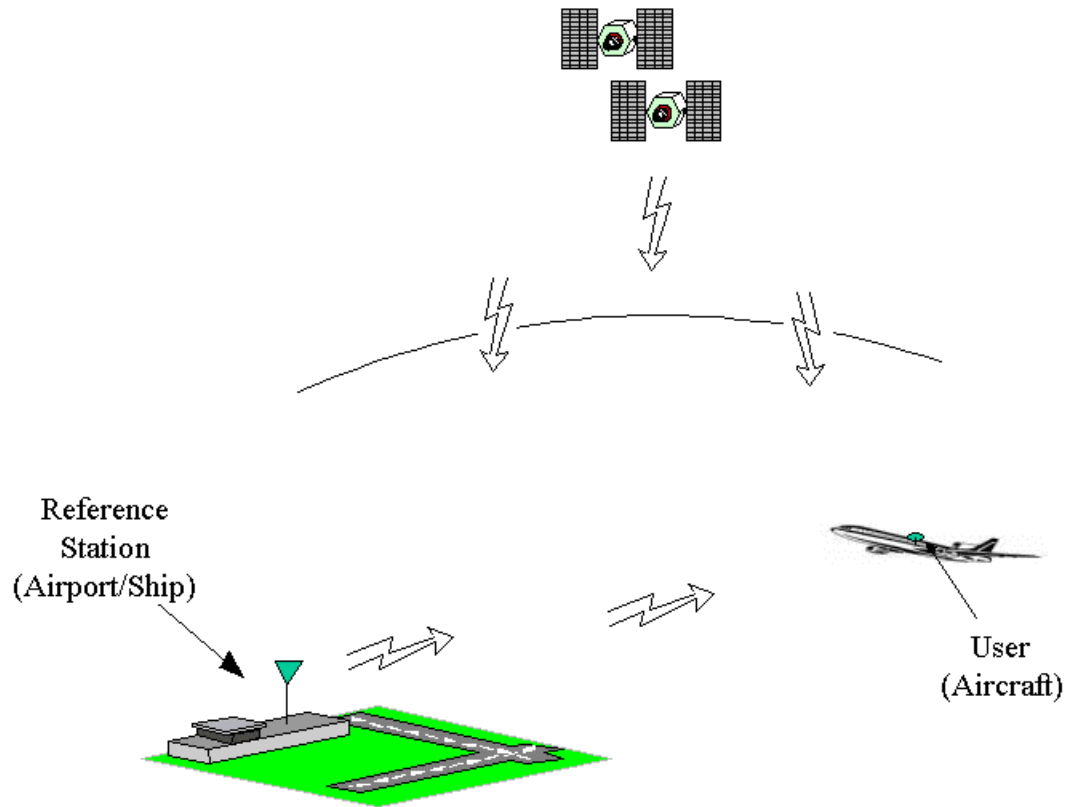


Figure 2.1. DGPS Concept

The single difference carrier phase measurement equations for several satellites can be written in the vector form as follows:

$$\Delta\phi = \begin{bmatrix} \Delta\phi_k^1 \\ \vdots \\ \Delta\phi_k^n \end{bmatrix} = [H \quad I] \begin{bmatrix} x_k \\ \tau_k \\ N_{L1}^1 \\ \vdots \\ N_{L1}^n \end{bmatrix} + \begin{bmatrix} v_k^1 \\ \vdots \\ v_k^n \end{bmatrix} \quad (2.3)$$

where H is the GPS geometry matrix

$$H = \begin{bmatrix} -e_k^1 & 1 \\ \vdots & \vdots \\ -e_k^n & 1 \end{bmatrix} \quad (2.4)$$

and n is the number of satellites in view. Spatial decorrelation errors (differential ionosphere and troposphere) are assumed to be small in this equation. When four or more satellites are in view, and cycle ambiguities are known, the user position can be estimated with respect to the reference station with centimeter level accuracy.

2.1.3 Differential Code Phase Observable. The use of code phase measurements is relatively easy to implement because they don't have cycle ambiguities. However, these measurements are much noisier than the carrier phase measurements. The single difference code phase is the sum of the single difference range, the single difference receiver clock bias, the single difference spatial decorrelation errors, and the single difference measurement noise. The matrix form of the differential code phase measurement is similar to Equation (2.3) without the cycle ambiguities.

$$\Delta PR = \begin{bmatrix} \Delta PR_k^1 \\ \vdots \\ \Delta PR_k^n \end{bmatrix} = [H] \begin{bmatrix} x_k \\ \tau_k \end{bmatrix} + \begin{bmatrix} v_{PR,k}^1 \\ \vdots \\ v_{PR,k}^n \end{bmatrix} \quad (2.5)$$

where ΔPR is the single difference code phase measurement and $v_{\Delta PR}^1$ is the code phase measurement noise for satellite 1. Spatial decorrelation errors are again assumed to be small.

2.1.4 Carrier Phase DGPS Error Sources. Although the nature of differential carrier phase GPS eliminates most common errors, some error sources still remain and affect the position accuracy. In this section, these error sources are described.

2.1.4.1 Receiver Noise. Thermal white noise for carrier phase measurements is typical and constitutes a small portion of the error. It is dependent on the phase-lock loop bandwidth and carrier signal power. The standard deviation of single difference carrier receiver noise [Carlson86] can be described by:

$$\sigma_r = \sqrt{\frac{B_{PLL}}{C/N_0} \frac{\lambda_{L1}}{2\pi}} \quad (2.6)$$

where,

σ_r is the carrier receiver noise due to thermal noise,

B_{PLL} is the phase-lock loop bandwidth (Hz), and

C/N_0 is the receiver carrier to noise ratio.

Figure 2.2 quantifies the single difference receiver thermal noise with respect to the elevation angle of satellite. We collected 5 hours of data across a short baseline (25.68 m) on the Engineering One building rooftop at the Illinois Institute of Technology (IIT). We used two Novatel GPS antennas and OEM 3 receivers with PLL bandwidth of 15 Hz. Based on the experimental results, as the satellite elevation angle increases, the error due to thermal noise decreases. The reason is that a higher satellite elevation angle provides higher receiver signal power strength.

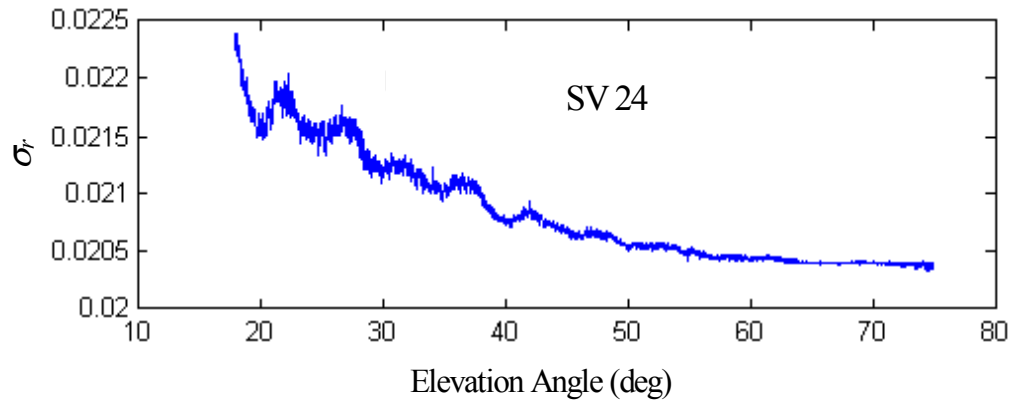


Figure 2.2. Single Difference Sigma of Thermal Receiver Noise

2.1.4.2 Cycle Slip. When the signal strength is low, the receiver phase lock loop may cause loss of lock in the GPS receiver phase lock loops. Although the receiver may reacquire the satellite signal quickly, a sudden integer cycle jump exists in the carrier phase observable. Such an event is known as a cycle slip. In CDGPS, because cycle slips affect the position estimation, they must be detected. Cycle slip detection will be discussed later in Chapter 3.

2.1.4.3 Multipath Error. Multipath error is due to reflected signal reaching the receiver. The reflected signal is delayed and usually weaker than the direct signal. The range measurement error due to multipath depends on the strength of the reflected signal and the delay between the direct and reflected signals.

For example, when the aircraft approaches the ship, it is in high dynamic motion. Because the satellite geometry is changing rapidly, the multipath error on the aircraft is relatively more akin to white noise. As a result, the time correlation of multipath is

shorter. In contrast, the time correlation of multipath on the ship is longer due to the slow geometry motion. The different time correlations may therefore require different filtering times to reduce the measurement errors due to multipath.

Figure 2.3 shows the double difference carrier error due to multipath using the IIT rooftop data. The double difference carrier phase measurement error roughly exhibits normal distribution behavior with standard deviation of approximately 5 mm (corresponding to a 3.5mm single difference).

2.1.4.4 Tropospheric Error. The troposphere is an atmospheric region between sea level and about 12 km. It affects code and carrier phase measurement delay identically. A first order model for this delay is often used to describe differential tropospheric error. This model is only a function of elevation angle and relative user height when the earth is assumed to be flat (on a local scale applicable to DGPS). The differential tropospheric error model is described by:

$$\Delta T = \frac{(\eta - 1)h}{\sin(el_i)} \quad (2.7)$$

where h is user height relative to the reference station, el_i is the elevation angle for satellite i , and η is the local index of refraction of the air (typically: 1.0003 ± 0.00005). For example, the differential tropospheric delay for an aircraft at 1000 feet with a 15 degree elevation satellite is about 1 foot.

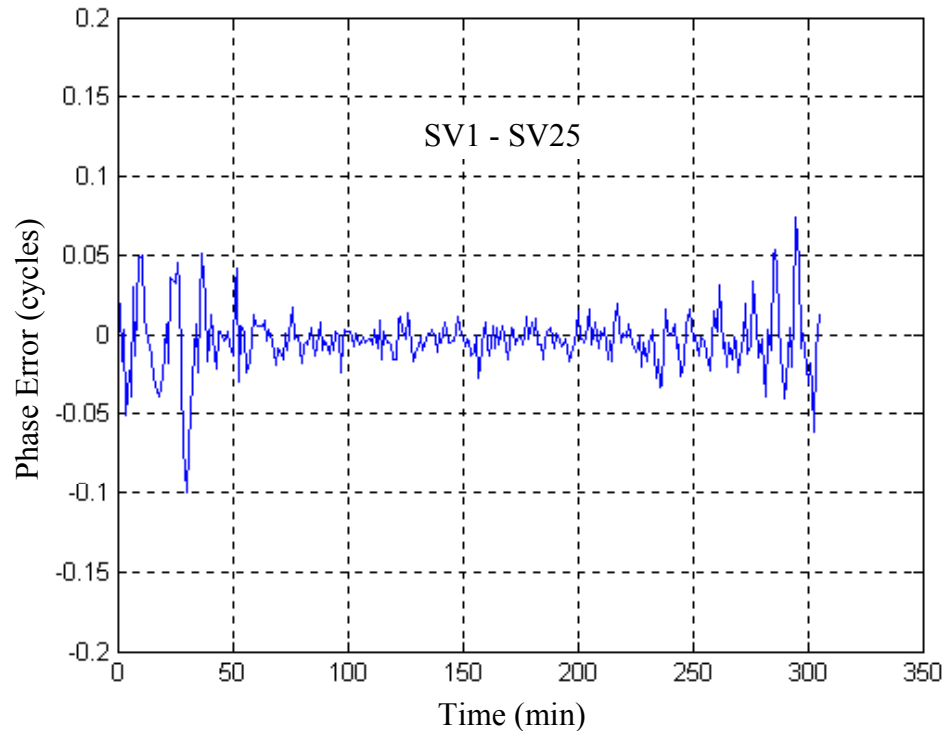


Figure 2.3. Multipath and Receiver Noise (Double Difference)

2.1.4.5 Ionospheric Error. The ionosphere layer is approximately at a height of 50 to 1000 km above the Earth's surface. The free electrons in the ionosphere cause a code phase delay and carrier phase advance. The amount of delay in the GPS signals is dependent on the total electron content (TEC) of the signal path through the ionosphere. Differential GPS navigation performance is degraded when ionospheric anomalies such as sharp spatial gradients exist due to the variations in the strength of the equatorial electrojet [Doherty97]. Such sharp gradients are most common near the auroral and equatorial region where the highest value of range delay is expected.

Nominally the effects of ionospheric errors are eliminated by the use of differential GPS. However, large or sharp ionospheric spatial gradients will remain and cause

differential position errors that are dependent on the displacement of the user from the reference. Detection of such ionospheric errors will be discussed later in Chapter 5.

2.1.4.6 Ephemeris Error. An ephemeris error occurs when the GPS satellite broadcasts the incorrect navigation message and incorrect satellite orbit parameters. This error can be caused in a number of ways: Master Control Station (MCS) uploads erroneous data, navigation data transmission errors from the satellite, scheduled or unscheduled satellite maneuvering, etc. Each satellite broadcasts its own orbit ephemeris so users can compute the satellite location at any time of interest. Because the satellite locations are used to calculate user position, an error in the satellite ephemeris will result in a navigation error. Ephemeris error detection will be described later in Chapter 4.

2.1.4.7 Doppler Effect. A change in the frequency of the signal received by the receiver due to relative motion between the satellite and the receiver is called the Doppler effect. The difference between the frequency of received and transmitted signal is defined as Doppler shift.

As an example, the GPS satellite ranges are between 20,000 and 25,000 km from the user on the surface of the earth. The range rate is changing while the satellites rise and set. This change in the range rate is the cause of Doppler shift. The single difference error on L1 carrier measurement due to the Doppler Effect (in meters) can be expressed as

$$\Delta E_{doppler} = (\lambda_{L1} \phi_u^i - \lambda_{L1} \phi_r^i) - (\lambda_{true,u} \phi_u^i - \lambda_{true,r} \phi_r^i) \quad (2.8)$$

where ϕ_u^i is the raw carrier phase measurement of L1 for satellite i on the user, ϕ_r^i is the raw measurement of L1 for satellite i on the reference, $\lambda_{true,u}$ is the true wavelength of the received L1 signal on the user, $\lambda_{true,r}$ is the true wavelength of the received L1 signal on the reference. The mathematical expression of true wavelength for the L1 signal can be written as

$$\lambda_{true} = \frac{c}{f_{true}} = \frac{c}{f_{L1}(1 - \frac{\dot{r}}{v_s})} = \frac{\lambda_{L1}}{1 - \frac{\dot{r}}{c}} \quad (2.9)$$

where \dot{r} is the range rate, and v_s is the speed of propagation of the waves. Figure 2.4 shows an example of the single difference error due to the Doppler Effect using a static baseline of 14.213 km. The user data was collected at the north side of downtown Chicago while the reference data was taken at the IIT rooftop antenna.

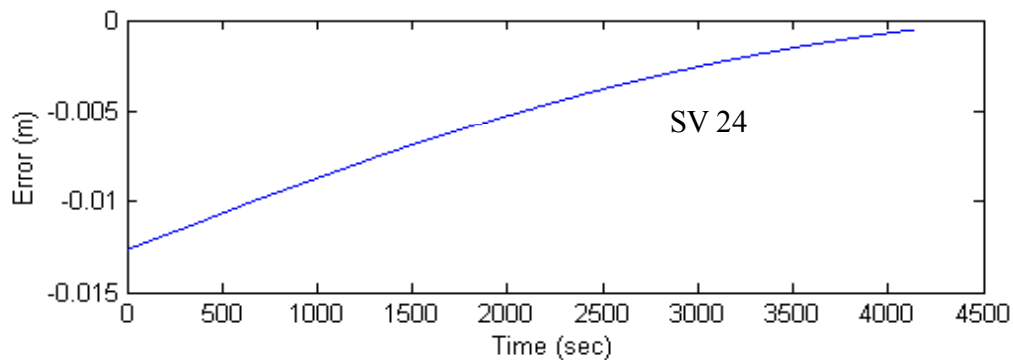


Figure 2.4. Doppler Effect on L1 Carrier Phase Measurement

2.1.4.8 Circular Polarization Error. The GPS satellites transmit a Right-Hand Circularly Polarized (RHCP) signal [SPS]. Therefore, the antennas are designed to receive the RHCP signals. Because the carrier signals are circularly polarized, differential range errors in the DGPS measurements are caused by the relative antenna orientation and relative satellite azimuth.

In the case of identically oriented antennas between the user and reference, the effects of the circular polarization on the phases of the signals received by the antennas are equal; therefore, the single-difference measurements are unaffected by the circular polarization. In contrast, when the antennas are not aligned, the phase effects of the circular polarization on the antennas are different.

When a rotation of either reference or user antenna around its boresight happens, it will change the carrier-phase by one cycle (one wavelength), for each complete rotation of the antenna. This effect is called “phase wind-up” [Wu 93]. As an example, let’s suppose that the aircraft flies doing three circles while the ship or ship antenna for SRGPS does not rotate. In this case, the magnitude of wind-up correction for the single difference carrier phase range measurement is about 57 cm. However, the wind-up effect is identical for all satellites and can be eliminated, along with the receiver clock bias, by double differencing.

2.2 Dual Frequency CDGPS

Unlike the L1 civil signal, the L2 signal is primarily intended for military use and is not within a protected Aeronautical Radio Navigation Services (ARNS) band. Fortunately, the dual frequency measurements will nominally be available with SRGPS.

2.2.1 Single Difference Carrier Phase Measurement on L2. The single difference measurement on L2 is similar to Equation (2.2), but has an additional inter-frequency bias term, which will be explained in the next section. At a given time index k , the differential carrier phase measurement of L2 for satellite i can be expressed as

$$\lambda_{L2} \Delta \phi_{L2,k}^i = -e_k^{iT} x_k + \Delta \tau_k + \Delta \tau_{IFB} + \lambda_{L2} \Delta N_{L2}^i - \gamma_{12} \Delta I_k^i + \Delta T_k^i + \Delta v_{L2,k}^i \quad (2.10)$$

where,

λ_{L2} is the wavelength of the L2 signal,

$\Delta \tau_{IFB}$ is the single difference inter-frequency bias in the receiver,

Δv is the single difference measurement error for L2 ($\sim N(0, \sigma_{\Delta \phi, L2}^2)$),

$\gamma_{12} = f_{L1}^2 / f_{L2}^2$ with f_{L1} and f_{L2} equal to the frequencies of the L1 and L2 carriers, respectively.

2.2.2 Inter Frequency Bias. Because the L1 and L2 phase path lengths within the receiver and satellite are different, relative errors may be introduced into the GPS measurements. These errors are called the inter frequency bias. The satellite inter frequency bias term is removed by the single difference in raw measurements as shown in Equation (2.10). The receiver clock bias and inter frequency bias can be eliminated by the double difference.

2.2.3 Carrier Phase Widelane Measurement. We have defined the single and double difference under Section 2.1.2. In this section, the additional difference between

L1 and L2 measurements produces a new signal with longer wavelength. It is called ‘widelane.’ Given the L1 and L2 single difference measurements in Equations (2.2) and (2.10), the single difference widelane carrier measurements can be constructed as follows:

$$\begin{aligned}
\Delta\phi_w^i &= (\Delta\phi_{L1}^i - \Delta\phi_{L2}^i) \\
&= \left(-e^{iT} x + \Delta\tau + \Delta T^i\right) \left(\frac{1}{\lambda_{L1}} - \frac{1}{\lambda_{L2}}\right) - \gamma\Delta I^i - \frac{\Delta\tau_{IFB}}{\lambda_{L2}} + (\Delta N_{L1}^i - \Delta N_{L2}^i) + \Delta\nu_w^i \quad (2.11) \\
&= \frac{\left(-e^{iT} x + \Delta\tau + \Delta T^i\right)}{\lambda_w} - \gamma\Delta I^i - \frac{\Delta\tau_{IFB}}{\lambda_{L2}} + (\Delta N_w^i) + \Delta\nu_w^i
\end{aligned}$$

where,

$\Delta\tau$ is the single difference receiver clock bias,

$$\gamma = \frac{1 - \beta_\phi}{\lambda_w},$$

ΔN_w^i is the single difference widelane cycle ambiguity for satellite i ,

$\Delta\nu_w$ is the single difference widelane measurement error in cycles, and

$$\lambda_w = \frac{c}{(f_{L1} - f_{L2})}$$

is the wavelength of the widelane.

The wavelength of the widelane is about 86 cm, and its frequency is $f_w = (f_{L1} - f_{L2}) = 347.8$ MHz [Misra01].

If Equation (2.11) is multiplied by its wavelength λ_w , we can express the widelane measurement in meters. The mathematical expression is shown in below.

$$\begin{aligned}
\Delta\Phi_w &= \lambda_w \left(\frac{\Delta\Phi_{L1}}{\lambda_{L1}} - \frac{\Delta\Phi_{L2}}{\lambda_{L2}} \right) \\
&= -e^T x + \Delta\tau + \Delta T - (1 - \gamma_{12})\Delta I + \frac{\Delta\tau_{IFB}}{\lambda_{L2}} + \lambda_w N_w + v_{w,meter}
\end{aligned} \tag{2.12}$$

where $\Delta\Phi_w = \lambda_w \Delta\phi_w$, $\Delta\Phi_{L1} = \lambda_{L1} \Delta\phi_{L1}$, $\Delta\Phi_{L2} = \lambda_{L2} \Delta\phi_{L2}$, and $v_{w,meter}$ is the single difference carrier phase widelane measurement error, which is normally distributed with zero mean and standard deviation of $\sigma_{w,meter}$. Given Equation (2.12), the relation between the widelane and L1/L2 carrier phase measurement error is simply obtained as shown in Equation (2.13).

$$\sigma_{w,meter} = \sqrt{\left(\frac{\lambda_w}{\lambda_{L1}} \sigma_{\Delta\phi,L1}^2 + \frac{\lambda_w}{\lambda_{L2}} \sigma_{\Delta\phi,L2}^2 \right)}. \tag{2.13}$$

where L1 and L2 carrier phase measurements errors are uncorrelated. If we assume that $\sigma_{L1,\Delta\phi} = \sigma_{L2,\Delta\phi} \equiv \sigma_{\Delta\phi}$, the sigma of single difference widelane carrier phase measurement can be expressed as follows

$$\sigma_{w,meter} = \sqrt{\left(\frac{\lambda_w}{\lambda_{L1}} + \frac{\lambda_w}{\lambda_{L2}} \right)} \sigma_{\Delta\phi}. \tag{2.14}$$

It is clear from (2.14) that the widelane measurements are significantly (about six times) noisier than the L1 or L2 measurements. More details on the widelane will be discussed in Chapter 6.

2.3 Cycle Ambiguity Estimation

In the CDGPS-based aircraft approach and landing system, performance is dependent on the success of cycle ambiguity resolution. In this section, general cycle ambiguity resolution methods will be discussed.

2.3.1 Using Redundancy of Carrier Measurements. If four or more satellites are in view, we may use the redundancy of carrier measurement to estimate the cycle ambiguity. In CDGPS, typically $n - 4$ redundant measurements can be used where n is the number of satellites in view. A higher number of redundant measurements provides lower estimation error for cycle resolution.

2.3.2 Averaging Code Against Carrier. This method uses the time averaging of the difference of code and carrier to estimate the cycle ambiguity. Because this process is not dependent on the satellite geometry information, it is also called geometry-free cycle resolution.

Updating the cycle ambiguity using the averaging code against carrier is known as code-centered-carrier filtering. It uses the advantage of each measurement. The carrier phase provides an accurate range measurement with unknown bias while the code measurement is noisy but unambiguous.

The traditional implementation of cycle resolution using those two methods will be described in the next section. In addition, a new cycle resolution algorithm using these methods will be explained in Chapter 6.

2.4 Real-Time CDGPS Kinematic Positioning Algorithm

In CDGPS, the integer cycle ambiguities must be resolved to compute the user position with centimeter accuracy. The details of airborne measurement processing, cycle ambiguity and position estimations, are discussed in [Lawrence96]. Recall from Equation (2.3), if a floating cycle ambiguity estimate, \hat{N} , and estimate error covariance, P_N , are available, then the equation can be written as:

$$\Delta\phi - \hat{N} = H \begin{bmatrix} x \\ \tau \end{bmatrix} + (\tilde{N} + \nu) \quad (2.15)$$

where \tilde{N} is the error between \hat{N} and the true integer N and ν is the vector of single difference carrier measurement errors, which are uncorrelated with a variance of $\sigma_{\Delta\phi}^2$.

The estimation of position and receiver clock bias using weighted least squares is shown in Equation (2.16),

$$\begin{bmatrix} \hat{x} \\ \hat{\tau} \end{bmatrix} = \begin{bmatrix} H^T & R_e^{-1} & H \end{bmatrix}^{-1} H^T R_e^{-1} (\phi - \hat{N}) \quad (2.16)$$

where $R_e = \sigma_{\Delta\phi}^2 I + P_N$.

The estimate error covariance for the position and clock bias is

$$P_{xx} = [H^T R_e^{-1} H]^{-1} \quad (2.17)$$

2.4.1 Estimate Initialization. In this process, integer estimates (\hat{N}) and the corresponding covariance matrix (P_N) must be initialized. The initialization of integer estimates is accomplished with the code phase measurements. Differencing equations (2.5) and (2.6) yields the following result (written in simple form)

$$\Delta\phi - \frac{\Delta PR}{\lambda} = N + v_{\Delta\phi - \Delta PR} \quad (2.18)$$

where,

$\Delta PR / \lambda$ is the code phase measurement expressed in L1 cycles,

λ is the L1 wavelength,

N is the cycle ambiguity for L1, and

$v_{\Delta\phi - \Delta PR}$ is the L1 measurement error for carrier minus code.

Finally, the initial integer estimates can be obtained as Equation (2.19).

$$\hat{N}_{L1} = \Delta\phi - \Delta PR / \lambda_{L1} \quad (2.19)$$

$$P_N = (\sigma_{\Delta\phi}^2 + \sigma_{\Delta PR}^2) I \cong \sigma_{\Delta PR}^2 I$$

where $\sigma_{\Delta PR}$ is the one sigma differential code phase measurement error.

2.4.2 Integer Measurement Update. After the integer estimates are initiated, the measurement update can be pursued. The estimation update is done by injecting new information into the following general measurement update form.

$$\begin{aligned} Z &= H_s N + v_z \\ E[v_z v_z^T] &= R \end{aligned} \tag{2.20}$$

where:

Z is the vector of new measurements,

H_s is the observation matrix for the new measurements, and

v_z is the measurement error.

If the linear equation is formed as Equation (2.20), then the Kalman filter algorithm [Gelb74] is applied for the measurement update:

$$\begin{aligned} K &= P_N^- H_s^T [H_s P_N^- H_s^T + R]^{-1} \\ \hat{N}^+ &= N^- + K(Z - H_s \hat{N}^-) \\ P_N^+ &= [I - KH_s] P_N^- \end{aligned} \tag{2.21}$$

where the superscripts ‘-’ and ‘+’ are used to indicate before and after the measurement update, respectively. No Kalman time update is necessary because the states being estimated are constants (cycle ambiguity integers).

2.4.2.1 Using Redundancy of Carrier Phase Measurement. If more than four satellites are in view, we can use the carrier phase measurement update. The differential carrier phase measurement can be cast into the form of Equation (2.20) using Equation (2.3) pre-multiplied by a matrix L_H , whose rows form a basis for the left null space of the matrix H [Lawrence96].

L_H can be obtained from the singular value decomposition of the observation matrix. The details of this singular value decomposition are discussed in [Pervan98]. The observation matrix is decomposed by

$$H = U \begin{bmatrix} S \\ 0 \end{bmatrix} V^T \quad (2.22)$$

where S is a 4×4 diagonal matrix, U is an $n \times n$ unitary matrix, and V is a 4×4 unitary matrix. The matrix, U , can be partitioned by the $n \times 4$ matrix, U_1 , and the $n \times (n - 4)$ matrix, U_2 . The vector form of U can be written as

$$U = [U_1 \quad U_2] \quad (2.23)$$

and

$$L_H = U_2^T. \quad (2.24)$$

The pre-multiplication by L_H eliminates the position and clock terms from the carrier phase measurement equation. Therefore, Equation (2.5) becomes

$$L_H \Delta\phi = L_H N + L_H \nu_{\Delta\phi} . \quad (2.25)$$

Equation (2.25) is substituted into Equation (2.20) using:

$$Z = L\Delta\phi .$$

$$H_s = L_H . \quad (2.26)$$

$$R = \sigma^2 L_H L_H^T = \sigma^2 I$$

2.4.2.2 Averaging Code against Carrier. Equation (2.18) was used to initialize estimates, and it already has the desired format for the estimate update:

$$Z = \Delta\phi - \Delta PR / \lambda$$

$$H_s = I . \quad (2.27)$$

$$R = (\sigma_{\Delta\phi}^2 + \sigma_{\Delta PR}^2) I$$

2.5 Real-Time CDGPS Static Initialization Algorithm

The CDGPS kinematic positioning system is based on the resolution of the carrier cycle ambiguities using satellite motion. Because this motion relative to a ground station or user is slow, the required initialization time is in the 30-45 minute range. In this

context, the static mode is implemented to reduce the amount of time to resolve cycle ambiguity integers.

Given the nature of the static mode, the user position is constant. Therefore, the position terms can be incorporated into the integer estimate. The mathematical expression of eliminating the clock terms in the geometry matrix is as follows:

$$L_{clock}\Delta\phi = L_{clock} \begin{bmatrix} -e_i^T & I \end{bmatrix} \begin{bmatrix} x \\ N \end{bmatrix} + L_{clock}V_{\Delta\phi} \quad (2.28)$$

where the rows of L_{clock} form a basis for the left null space of the $n \times 1$ vector

$$V_{\tau} = \begin{bmatrix} 1 \\ \vdots \\ 1 \end{bmatrix}. \quad (2.29)$$

2.5.1 Static Mode State Initialization. The states and corresponding covariance matrix can be written as

$$\hat{N}_s = \begin{bmatrix} x \\ \dots \\ N \end{bmatrix}, \quad (2.30)$$

and

$$P_{Ns} = \begin{bmatrix} P_x & \vdots & 0 \\ \cdots & & \cdots \\ 0 & \vdots & P_N \end{bmatrix} \quad (2.31)$$

where,

\hat{N}_s is the $(3+n) \times 1$ state vector, which is a combination of static position and integer estimates,

P_{Ns} is the $(3+n) \times (3+n)$ covariance matrix, and

P_x is the covariance of position estimates.

In this case, N and P_N are initialized by the method described in Section 2.4.1. For the position terms, x can be initialized with zeros, and P_x is assigned a big number of 10^6 .

2.5.2 Static Mode Measurements Update. After the initialization, the carrier phase redundant measurement update activates with subjecting Equation (2.28) into (2.21) with

$$\begin{aligned} Z &= L_{clock} \Delta\phi \\ H_s &= L_{clock} [-e^T \quad I]. \\ R &= \sigma_{\Delta\phi}^2 I \end{aligned} \quad (2.32)$$

In the measurement update using averaging code against carrier, we use the same method as Section 2.4.2, but the observation matrix and states are different as shown in Equation (2.33).

$$\Delta\phi - \Delta PR = \begin{bmatrix} \mathbf{0} & \vdots & I \end{bmatrix} \begin{bmatrix} x \\ \cdots \\ N \end{bmatrix} + v_{\Delta\phi - \Delta PR} \quad (2.33)$$

where $\mathbf{0}$ in the observation matrix is the $n \times 3$ matrix filling with zeros. Equation (2.33) is already in the desired form of Equation (2.16) again with

$$\begin{aligned} Z &= \Delta\phi - \Delta PR \\ H_s &= \begin{bmatrix} 0 & \vdots & I \end{bmatrix} \\ R &= (\sigma_{\Delta\phi}^2 + \sigma_{PR}^2)I \end{aligned} \quad (2.34)$$

2.5.3 Cycle Ambiguity Estimation with Known User Position. If we know the user position with centimeter level accuracy, this position vector can be treated as known biases in Equation (2.28) as shown below in Equation (2.35).

$$L_{clock} \Delta\phi - L_{clock} G \hat{x} = L_{clock} [N] + G \tilde{\delta} \tilde{x} + L_{clock} v_{\Delta\phi} \quad (2.35)$$

where,

$$G = \begin{bmatrix} -e_1^T \\ \vdots \\ -e_n^T \end{bmatrix}, \quad (2.36)$$

and $\hat{\delta x}$ is the error in the position estimate.

Finally, Equation (2.35) is substituted into Equation (2.20) using

$$\begin{aligned} Z &= L_{clock} \Delta\phi - L_{clock} G \hat{x} \\ H_s &= L_{clock} \\ R &= GP_x G^T + \sigma_{\Delta\phi}^2 I \end{aligned} \tag{2.37}$$

2.6 CDGPS Test Results

A prototype Carrier Phase Differential GPS (CDGPS) architecture was developed, implemented, and tested with 10 cm accuracy. This section describes some relevant details of the prototype implementation and the test results.

The algorithm of the CDGPS system was tested at the Navigation and Guidance Laboratory (NGL) at IIT prior to a field test with the Autonomous Ground Vehicle (AGV: named Leonard), which was developed by NGL [Mathieu02 and Christ03]. Figure 2.5 shows the estimated user distance from the reference antenna for about 7 hours time with the covariance envelope (dotted line in the figure). In the figure, the estimated distance up to 45 minutes (dash-dot vertical line) is noisy because of initialization time. Figure 2.6 describes the 3-D position estimation error over the same period of time. As you can see, the horizontal and vertical position estimation errors never exceed 5 cm after the 45 minutes initialization. With the small estimation errors, the actual 2-D estimated positions after the initialization are shown in Figure 2.7. The position vectors were computed in terms of the east-north-up local coordinate system, and they are all in the $10\text{ cm} \times 10\text{ cm}$ box.

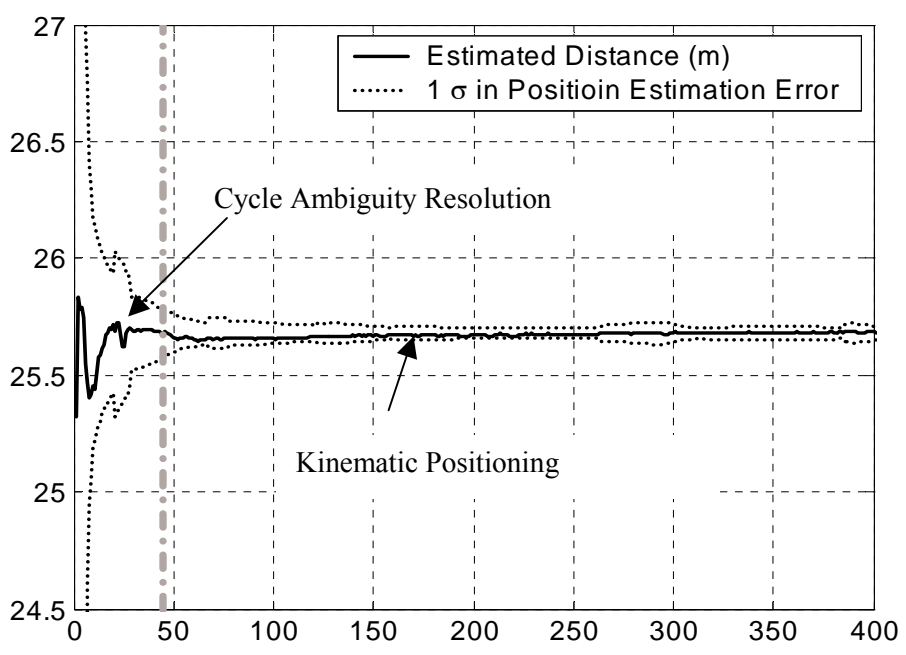


Figure 2.5. Distance Estimation using CDGPS

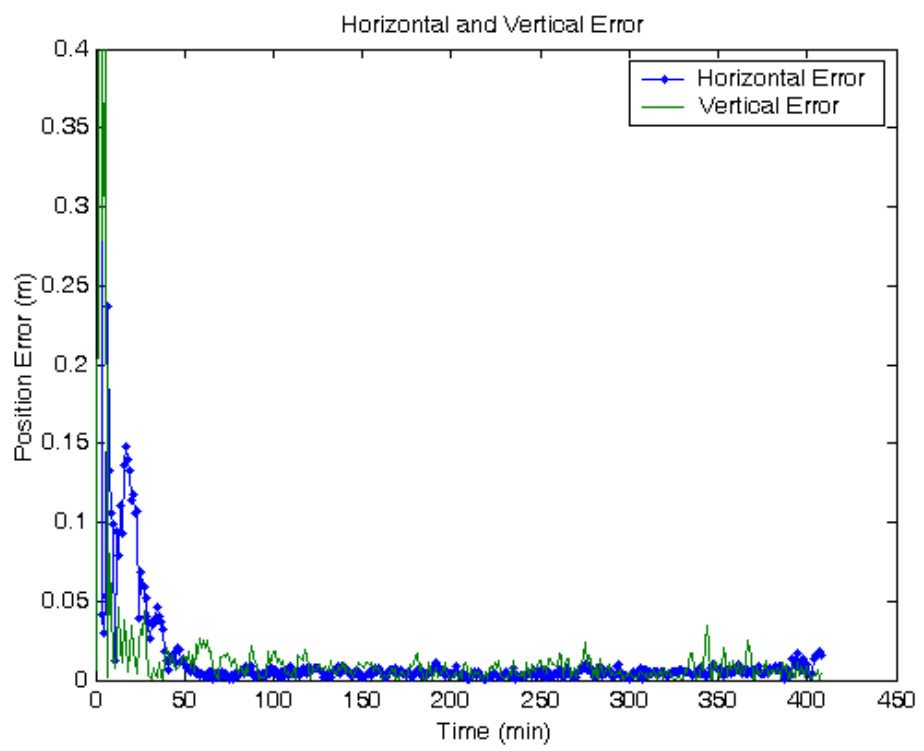


Figure 2.6. 3-D Position Estimation Error

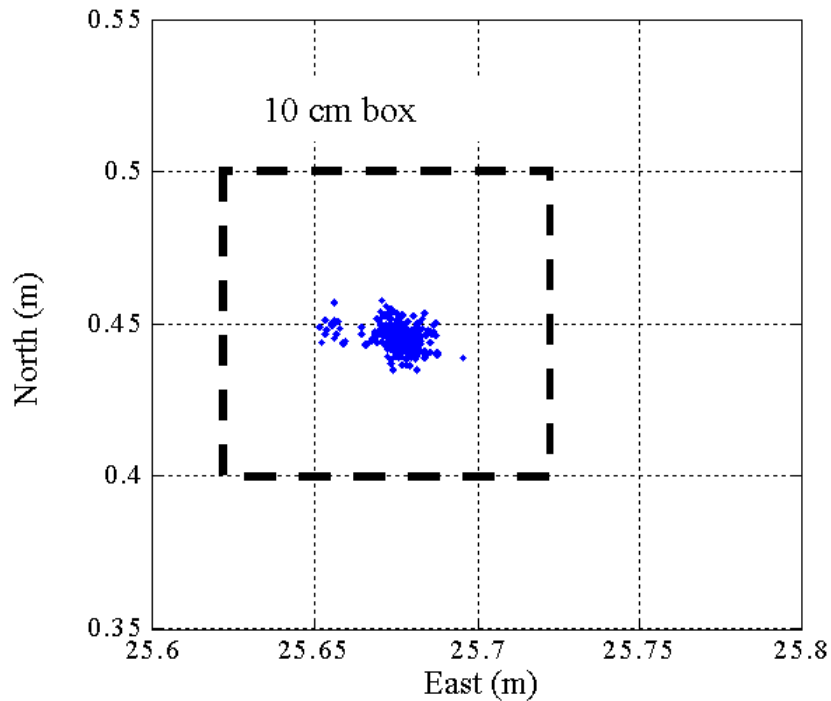


Figure 2.7. 2-D Kinematic Position Estimation

In summary, the experimental results showed position accuracy of approximately 5 cm and were reliably achievable following a 30-45 minute initialization time. The initialization interval ensured sufficient satellite motion to resolve GPS carrier cycle ambiguities.

Leonard (the AGV) was tested on the Illinois Institute of Technology's soccer field. Because the vehicle was designed to support missions that are unsafe or too difficult for human operation, the CDGPS system is required. Leonard has a nominal velocity of 0.7m/s and a controller update rate of 2Hz with a single GPS patch-antenna. The goal of the test was to autonomously find the desired trajectory. In this test, the desired trajectory was a straight line to the north, and Leonard took 40 minutes initialization time. The test result was compared with the simulation result. The result shows that the system achieved

sub-decimeter-level lateral accuracy (including errors from Leonard) as we expected in the simulation. Results are shown in Figure 2.8.

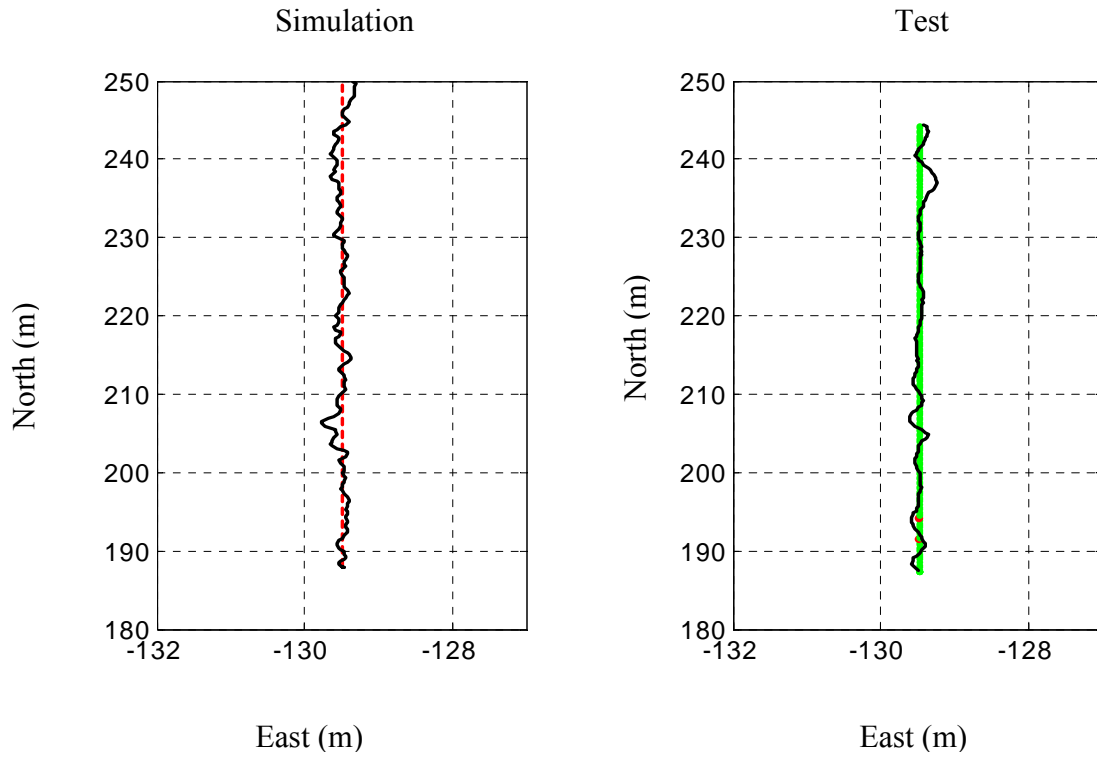


Figure 2.8. AGV CDGPS Kinematic Positioning Real-Time Test

CHAPTER 3

CYCLE SLIP DETECTION

3.1 Introduction

The use of highly precise differential carrier phase measurements in SRGPS enables the high navigation performance required for shipboard landing. However, this performance is dependent on maintaining continuous phase lock on the carrier signals. Interference, jamming, shadowing, and high dynamics may cause loss of phase lock and result in a sudden integer cycle jump in the carrier phase observable. Such an event is known as a cycle slip, and integrity is compromised when it is not detected. Important prior cycle slip detection work focused on the use of geometry-free linear combinations of available observables to test for abrupt discontinuities in the measurements. In this section, the effectiveness of Receiver Autonomous Integrity Monitoring (RAIM) [Lee95, Parkinson88, Pervan98, Sturza88] for cycle slip detection is explored. Single and multiple channel cycle slip threat models are considered for both single and dual frequency SRGPS architectures (using the single difference carrier phase measurements). The traditional RAIM concept (Appendix A) is extended in this research by applying integer and half-integer constraints on failure magnitude. In addition, the availability of the RAIM-based cycle slip detection function is directly evaluated in this work. Cycle ambiguity resolution is not strictly necessary for RAIM-based cycle slip detection because differences between sequential single difference measurements can be used as the basis for detection.

SRGPS can potentially operate in two different modes: a nominal dual frequency architecture and a single frequency backup when interference or jamming exists in either the L1 or L2 band. Single and multi-channel cycle slips are considered for both the single and dual frequency architectures. The availabilities of the RAIM function for cycle slip detection are evaluated independently for the single and dual-frequency architectures.

3.2 RAIM-based Fault Detection

The RAIM concept is based on verification of the consistency of redundant GPS measurements [Kalafus87]. It uses the residual vector as a test statistic against a certain pre-defined threshold to decide whether the navigation system has failed or is in normal operation. RAIM is a useful approach to fault detection because it has the ability to detect many different types of failures in a relatively simple way. However, the performance of RAIM is limited by the need for redundant satellites (at least five are required).

While numerous RAIM methods have been introduced and developed, the use of the norm of the least squares residual vector [Parkinson88] is the most direct. The residual vector (r) can be obtained by taking the difference between true range measurement and predicted range measurement which is computed using the least squares solution. The sum of the squares of the residuals (called the sum of squared error (SSE)) is the basic observable in the RAIM.

The simple form of RAIM fault detection is based on the magnitude of the residual vector as a statistical indicator of possible navigation failure. Under normal error conditions (no failures):

$$\frac{\|r\|^2}{\sigma_z^2} \sim \chi^2(n-m) \quad (3.1)$$

where r is the residual vector, σ_z is the standard deviation of measurement error, n is the number of satellites in view, m is the number of unknowns, and $\chi^2(n-m)$ is the chi-square distribution with $(n - m)$ degrees of freedom (m is always 4 in this research). The generalized residual threshold can be obtained using Equation (3.1). The threshold is a function of the number of degrees of freedom and the desired false alarm probability (for example, 10^{-1} , 10^{-4} , 10^{-7} and 10^{-10}) as shown in Figure 3.1.

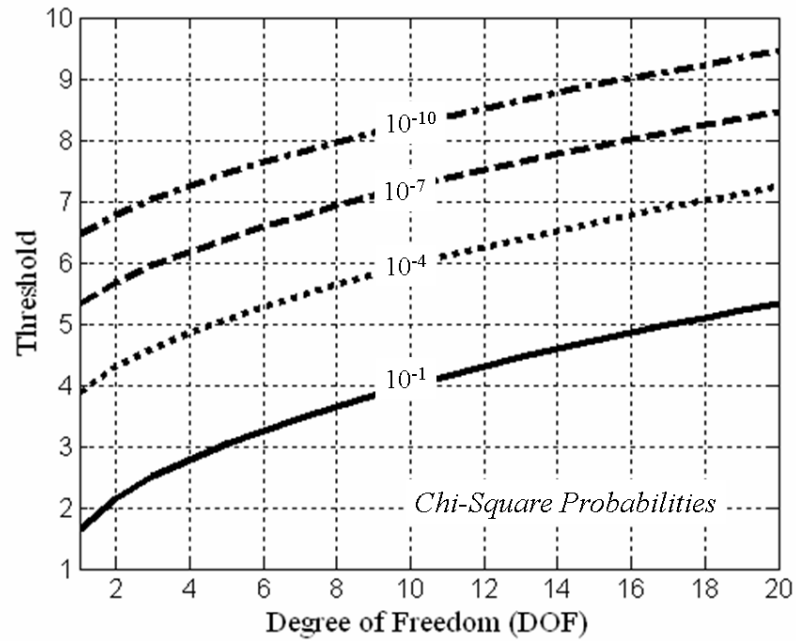


Figure 3.1. RAIM Detection Thresholds

3.3 Single Frequency Architecture

For a single frequency processing architecture (operating on either L1 or L2, in the event of jamming or interference on the other frequency), it is possible to detect single channel cycle slips using carrier phase RAIM. A symbolic illustration of such a scenario is shown in Figures 3.2 and 3.3, which respectively show the nominal case of tracking six satellites in view and a cycle slip occurrence on Channel 6.

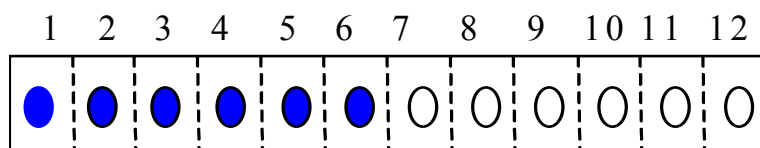


Figure 3.2. Normal Condition

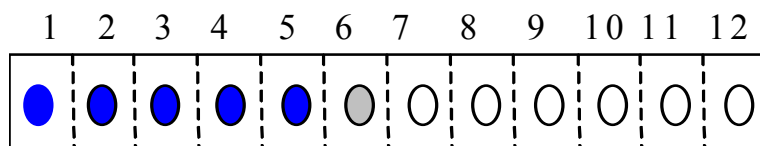


Figure 3.3. Cycle Slip Occurs on a Single Channel

In RAIM fault detection, a missed detection is said to occur when the position error exceeds the required alert limit but the least-squares residual is smaller than a predefined detection threshold. For SRGPS, the Vertical Alert Limit (VAL) is specified to be 1.1 m, and the detection threshold is defined to ensure a specified false alarm probability that is consistent with the continuity requirements for SRGPS. In this analysis, we assume a required false alarm probability of 10^{-7} .

To evaluate RAIM-based cycle slip detection performance, integer constraints on failure magnitude are applied. Specifically, it is assumed that the cycle slip occurs on the worst-case satellite channel with the worst-case bias of integer or half-integer magnitude.

Given a failure on a single satellite channel, the Failure Mode Slope (FMS) for the satellite is defined as the ratio of the vertical position error to the magnitude of the residual vector. As illustrated in Figure 3.4, the normal measurement error dispersion (the ‘ellipse’ shown in the figure) can be envisioned to slide up and down along the FMS depending on the failure magnitude. In the figure, and in the remainder of this dissertation, $\|r\|$ is the norm of the residual vector, and δx_3 is the vertical position error. Because there exist multiple satellite measurements, there are multiple FMSs. Therefore, we consider the limiting case where the cycle slip occurs on the satellite channel with the steepest (worst-case) FMS.

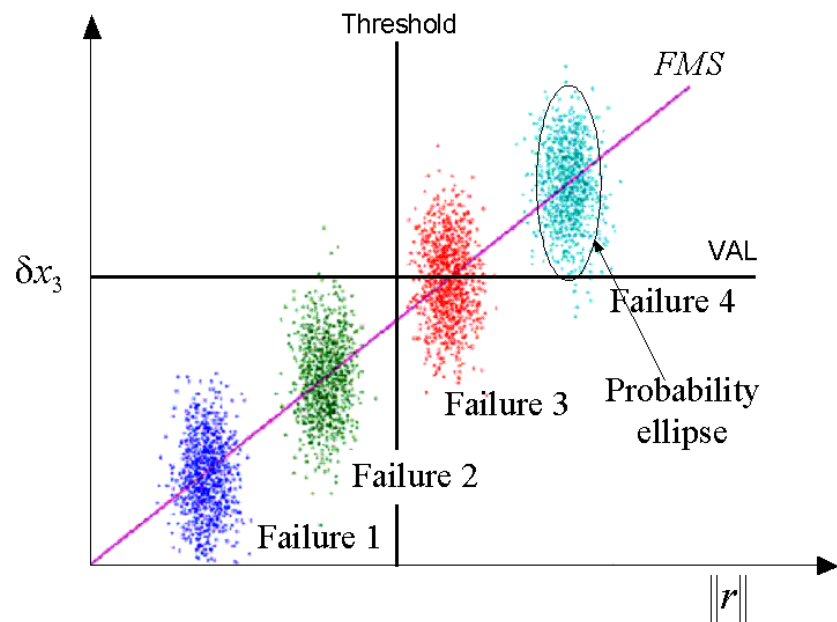


Figure 3.4. Basic RAIM Algorithm

The worst-case failure magnitude can be found by increasing the failure magnitude by half cycle increments along the worst-case FMS. The probability of missed detection is computed at each increment, and the failure magnitude where the probability of missed detection is maximized is selected as the worst-case cycle slip.

The probability of missed detection is defined as the joint probability that the position error is larger than the VAL and that the residual is smaller than the threshold. The mathematical representation of the probability of missed detection is provided in Appendix B. In order to ensure navigation integrity using RAIM, the probability of missed detection must be lower than the ratio of the allocated integrity risk requirement and the prior probability of the failure event. In this work, we typically assume a required missed detection probability of 10^{-4} , but this value is varied in the analysis to observe its influence on overall performance. Given a missed detection probability requirement, the performance of RAIM-based cycle slip detection is quantified by its service *availability*.

3.3.1 Availability Analysis. Availability is defined as the fraction of time a navigation system is usable by the navigator. In the context of our RAIM analysis, a satellite geometry is declared unusable when the probability of missed detection of the worst-case cycle slip is larger than the pre-specified minimum required to ensure integrity. RAIM availability is fundamentally limited by the ‘raw’ availability of having at least five satellites in view. This raw availability is the maximum theoretical RAIM availability a user can achieve.

The effect of depleted GPS satellite constellations were also included in these results—and all subsequent availability results in this dissertation—using the ‘minimum

standard' constellation state probability model provided in the GPS Standard Positioning Service Performance Standard (GPS SPS) [SPS]. The state probability model used is given in Table 3.1.

Table 3.1. GPS Constellation Availability

Number of Healthy Satellites	State Probability
24	0.95
23	0.03
22	0.12
21	0.005
20	0.003

3.3.2 Simulation Results. For a single frequency processing architecture, the service availability of carrier phase RAIM has been evaluated for the detection of full and half cycle slips on a single-channel. Figures 3.5, 3.6, and 3.7 quantify the sensitivity of RAIM availability to ship location. The RAIM availability results were computed for three different ship longitudes—Indian Ocean (60 deg E), Atlantic Ocean (-60 deg E) and Pacific Ocean (-135 deg E)—and latitudes varying from 5 deg N to 45 deg N. Each figure shows results for a constant longitude and variable latitude assuming a 7.5 deg elevation mask, a single difference measurement error standard deviation of 1 cm, and a required missed detection probability of 10^{-4} . In these figures, the bars represent, from left to right, the RAIM availability for detection of general failures with real-valued magnitude, cycle slips of integer or half-integer magnitude, cycle slips of integer magnitude, and the raw availability of having at least five satellites in view. The worst-case (lowest) service

availability observed in these results occurs in Figure 3.7 (at 15 deg N, -135 deg E). It is clear, however, that even in this case RAIM availability is higher than 97 percent, exceeding significantly the 95 percent target for single frequency operation. It is also evident in the results that minimal availability improvement is derived from the application of integer or half integer constraints on failure magnitude.

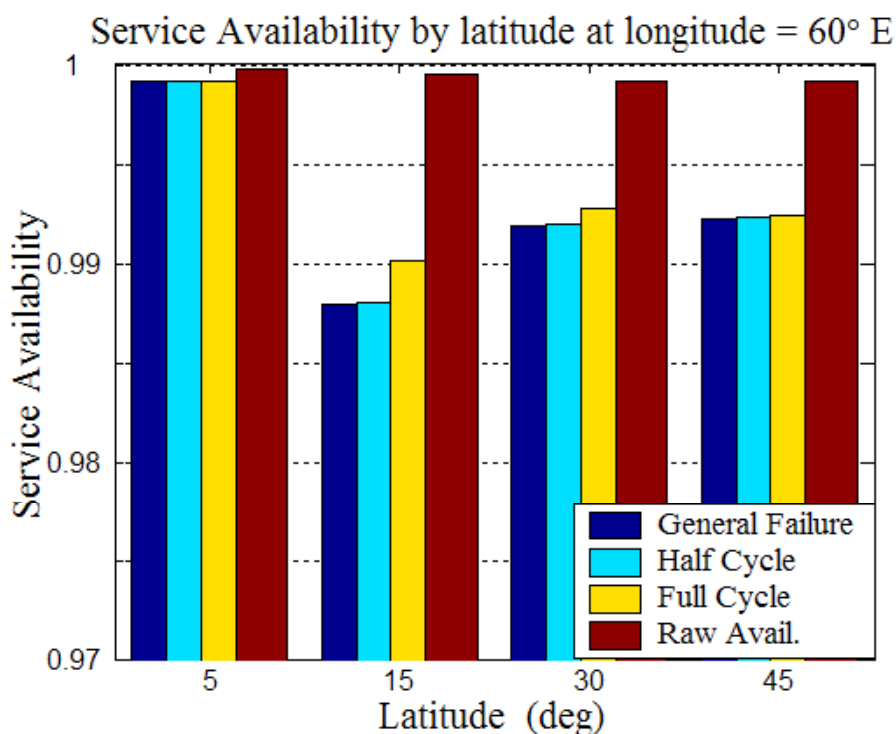


Figure 3.5. Service Availability at Longitude at 60° E

The sensitivity of RAIM availability to elevation mask is shown in Figure 3.8. The results in the figure were computed for the worst observed location found above, a required missed detection probability of 10^{-4} , and a single difference measurement error standard deviation of 1 cm. The results show that RAIM availability is moderately

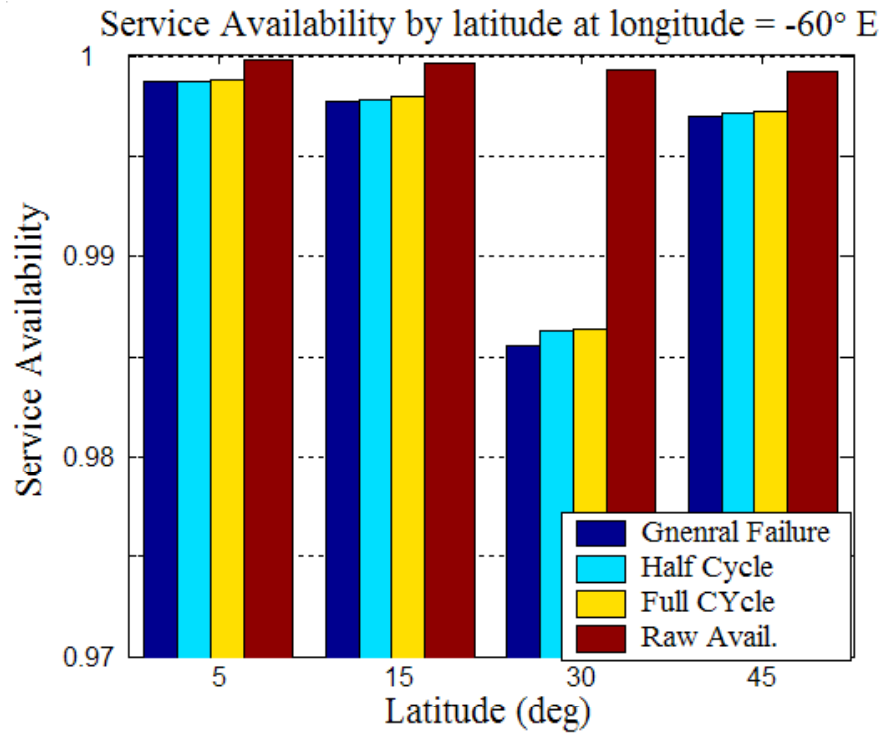


Figure 3.6. Service Availability at Longitude = -60° E

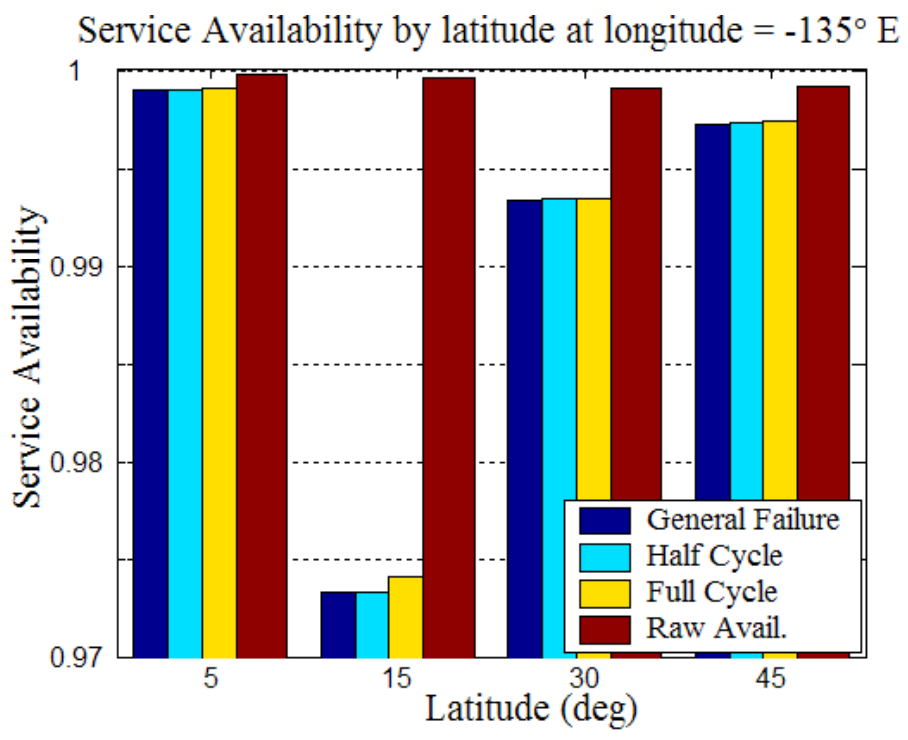


Figure 3.7. Service Availability at Longitude = -135° E

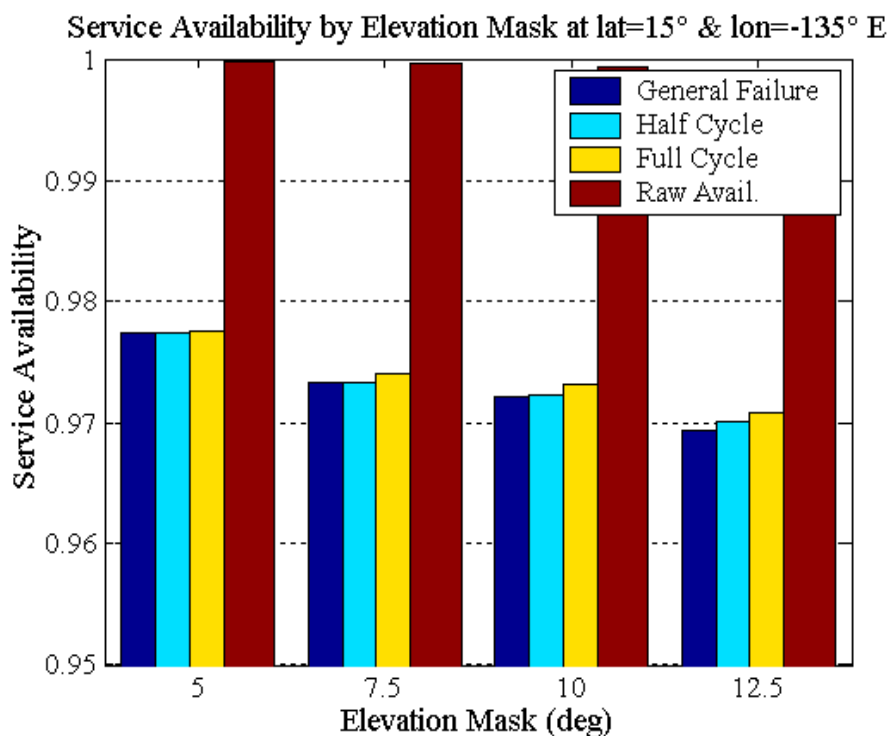


Figure 3.8. Service Availability vs. Elevation Mask

sensitive to elevation mask, but that a 95 percent target for single frequency operation is nevertheless easily achievable even for an elevation mask of 12.5 deg.

The sensitivity of RAIM availability to required missed detection probability is shown in Figure 3.9. The results in the figure were computed for the worst observed location defined above, an elevation mask of 7.5 deg, and a single difference measurement error standard deviation of 1 cm. The results show that RAIM availability exhibits relatively weak sensitivity to required missed detection probability.

Finally, Figure 3.10 quantifies the sensitivity of RAIM availability to carrier phase measurement error standard deviation (σ). Again, the worst-case location, elevation mask of 7.5 deg, and required missed detection probability 10^{-4} were used. Smaller nominal

Service Availability by Required Probability of Missed Detection

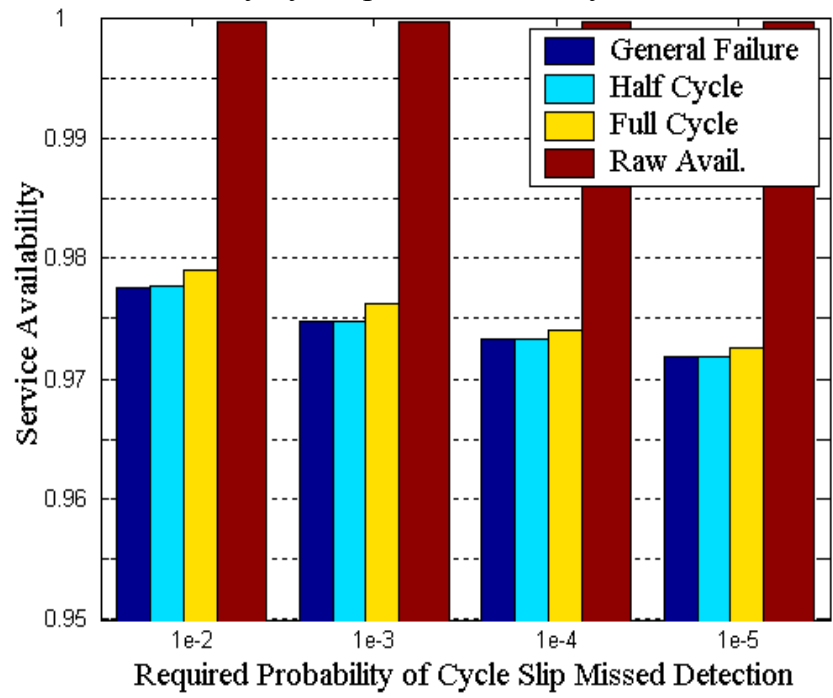


Figure 3.9. Service Availability vs. Required Probability of Cycle Slip Missed Detection

Service Availability by Standard Deviation of Measurement Error

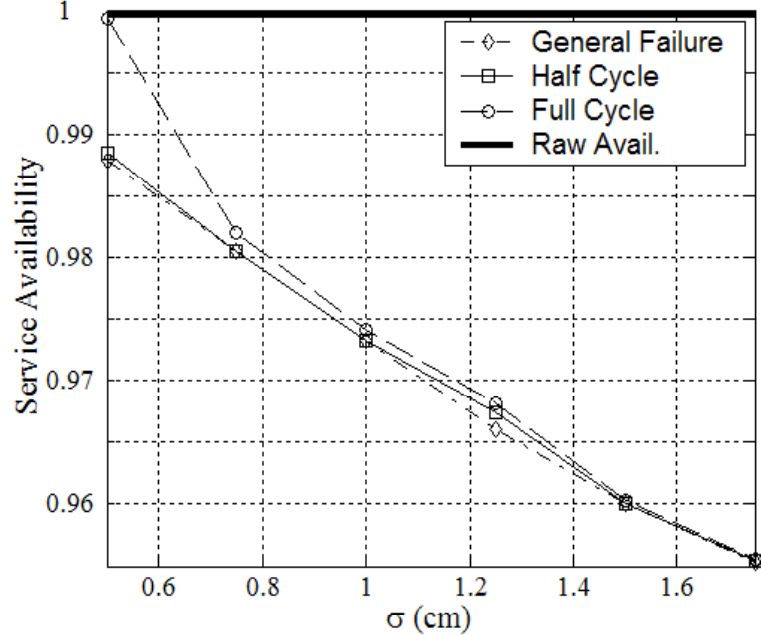


Figure 3.10. Availability vs. Measurement Error

measurement error allows for tighter detection thresholds, thereby reducing the number of satellite geometries that have missed detection probabilities higher than 10^{-4} . As a result RAIM availability is greater when measurement error standard deviation is lower. However, it is clear that service availability greater than 95 percent is achievable for values of σ up to 1.8 cm.

3.4 Dual Frequency Architecture

For a dual frequency processing architecture (the nominal operating mode for SRGPS), greater measurement redundancy exists for the detection of cycle slips. Figures 3.11 and 3.12 show a symbolic illustration of simultaneous multi-channel cycle slips in a dual frequency system.

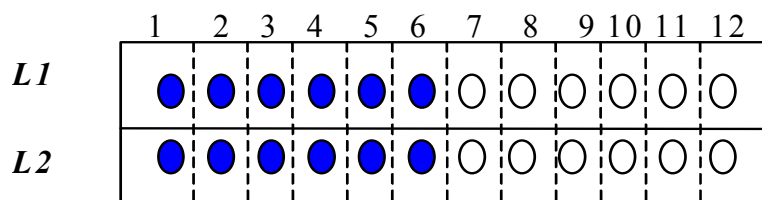


Figure 3.11. Normal Conditions

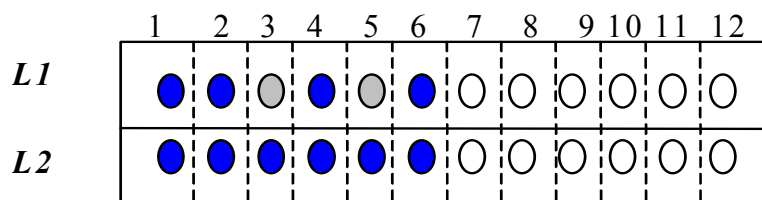


Figure 3.12. Cycle Slips Occur on L1 Channels 3 and 5

We first consider the case where the cycle slips do not simultaneously occur on both frequencies for the same satellite. In this case, cycle slips can be detected by direct differencing of L1 and L2 single difference ranging measurements:

$$\Delta\phi_{L12} = \phi_{L1} - \phi_{L2} = b + \Delta\nu \quad (3.2)$$

where b is the bias due to the failure and $\Delta\nu$ is the nominal double difference measurement error which is distributed as $N(0, \sigma^2)$. Figure 3.13 illustrates a simple detection scenario where a threshold T is set such that, under normal error conditions, the probability of false alarm is sufficiently low to ensure navigation continuity. Given a false alarm probability of 10^{-7} and double difference $\sigma = 1$ cm, a missed detection probability of 10^{-4} can be ensured only if the magnitude of the bias (b) is greater than 0.128 m. Because the magnitude of a full cycle slip on both L1 (19 cm) and L2 (24 cm) is

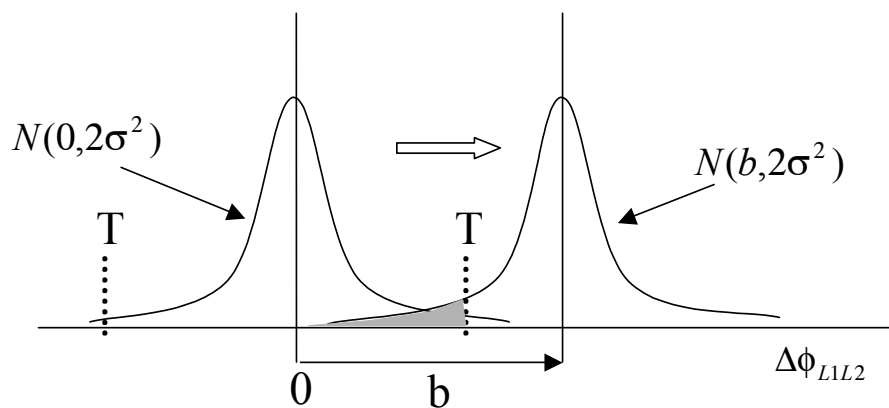


Figure 3.13. Differencing Between L1 and L2

always larger than the minimum detectable bias, the availability of the fault detection function using L1-L2 differencing is 100% for full cycle slips. In contrast, half cycle slips (0.095 m for L1 and 0.12 m for L2) are smaller in magnitude than the minimum detectable bias for $\sigma = 1$ cm, and therefore cannot be detected with the specified missed detection probability. Such events can be detected with full availability only if the double difference $\sigma < 0.74$ cm.

3.5 Summary of Cycle Slip Detection

The availability performance of autonomous cycle slip detection using redundant GPS measurements is encapsulated in Table 3.2. In summary, detection of cycle slips is guaranteed with the required availability for both single and dual frequency architectures provided that:

1. For a single frequency architecture, slips do not simultaneously occur on multiple channels.
2. For a dual frequency architecture, cycle slips are larger than one half integer in magnitude and do not simultaneously occur for the same satellite on both frequencies.

To ensure comprehensive detection of such events, inertial augmentation of the integrity monitor will likely be required [Altmayer00].

Table 3.2. Summary of Cycle Slip Detection

	Single Frequency Algorithm		Dual Frequency Algorithm		
	Single Channel	Multichannel	Single Channel	Same SV	Different SVs
Required Service Availability	95%		99.7%		
Cycle Slip Occur	Yes	No	No*	No	No*
Half Cycle Slip	Yes	No	Yes	No	Yes
Full Cycle Slip	Yes	No	Yes	No	Yes

*RAIM is possible, but availability is lower than 99.7%.

CHAPTER 4

EPHEMERIS ERROR DETECTION

4.1 Introduction

Each satellite broadcasts its own orbit ephemeris so users can compute the satellite location at any time of interest. Because the satellite locations are used to calculate user position, an error in the satellite ephemeris will result in a navigation error. Under normal conditions these errors are negligibly small for differential GPS users. However, integrity considerations for aircraft precision landing navigation dictate that *anomalous* conditions must be quickly detected. Furthermore, orbit ephemeris anomalies cause navigation errors that are dependent on the time-varying displacement between the aircraft and reference receiver. Therefore, the impact of ephemeris anomalies on navigation must ultimately be assessed separately by each individual aircraft within the SRGPS service volume. In this context, carrier phase RAIM is an attractive solution. The basis for observability of ephemeris failures using RAIM is that the magnitude of the residual test statistic will change proportionally during an approach as the distance between the aircraft and ship decreases. The effectiveness of such a ‘relative’ RAIM method is therefore dependent on the magnitude of the observed change in the test statistic, which in turn is dependent on total change in displacement during the approach within the SRGPS service radius.

Figure 4.1 illustrates the basic concept. The ‘Service Entry Point’ is the radius where the aircraft is first able to receive a reference measurement, and the ‘synthetic baseline’ is the distance between service entry point and aircraft location at any given time over the

flight path. As the synthetic baseline increases, the ephemeris error will become detectable using relative RAIM. In this section, the autonomous ephemeris detection algorithm is described, and its effectiveness for SRGPS is evaluated.

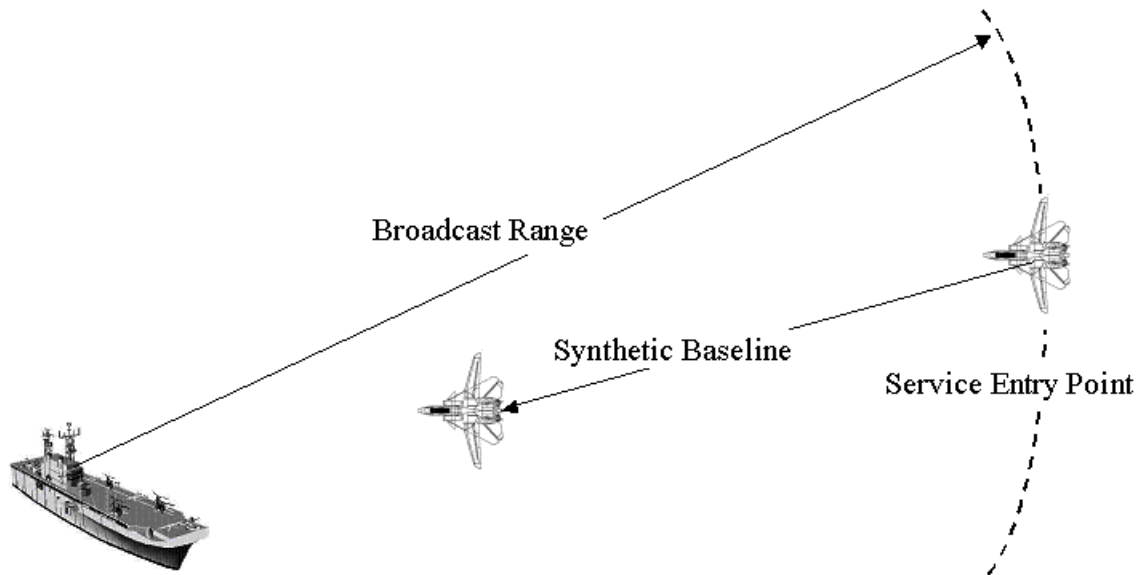


Figure 4.1. Service Entry Point and Synthetic Baseline

Because SRGPS uses carrier phase differential GPS, navigation performance is dependent on the successful resolution of cycle ambiguities corresponding to the GPS satellites in view. During measurement updates, the ephemeris error may affect the cycle ambiguity estimation process. In turn, incorrectly estimated cycle ambiguities can be used later during the approach to compute incorrect user (aircraft) position. To bound the position error caused by an ephemeris anomaly, we consider two limiting cases for cycle estimation implementations:

1. Limit Case 1: Cycle ambiguities are established by averaging code against carrier.
2. Limit Case 2: Cycle ambiguities are established using redundancy of carrier measurements.

Most implementations will use a hybrid of these two limiting scenarios.

4.2 Limit Case 1

In this scenario, which is known as ‘geometry-free’ cycle resolution, the ephemeris error does not affect the cycle ambiguity estimation process because time averaging the difference of code and carrier to measure the cycle ambiguity is not dependent on satellite geometry information. However, given that the cycle ambiguities are correctly estimated, errors will still be incurred during the positioning process because satellite geometry information is used. Specifically, positioning error due to satellite ephemeris error will be proportional to the displacement between the aircraft and reference receiver. In Figure 4.2, the solid line qualitatively illustrates the erroneous vertical position error history over the flight path. The mathematical expression for vertical position error is:

$$\delta x = H_{3,i}^+ \delta H_i u x \quad (4.1)$$

where

H^+ is the pseudoinverse of the observation matrix,

δH_i is the error in the observation matrix due to an ephemeris error on satellite i ,

u is the approach path direction (unit vector),

x is the scalar displacement between the aircraft and reference antennas, and
 δx is the resulting vertical position error due to orbit ephemeris error.

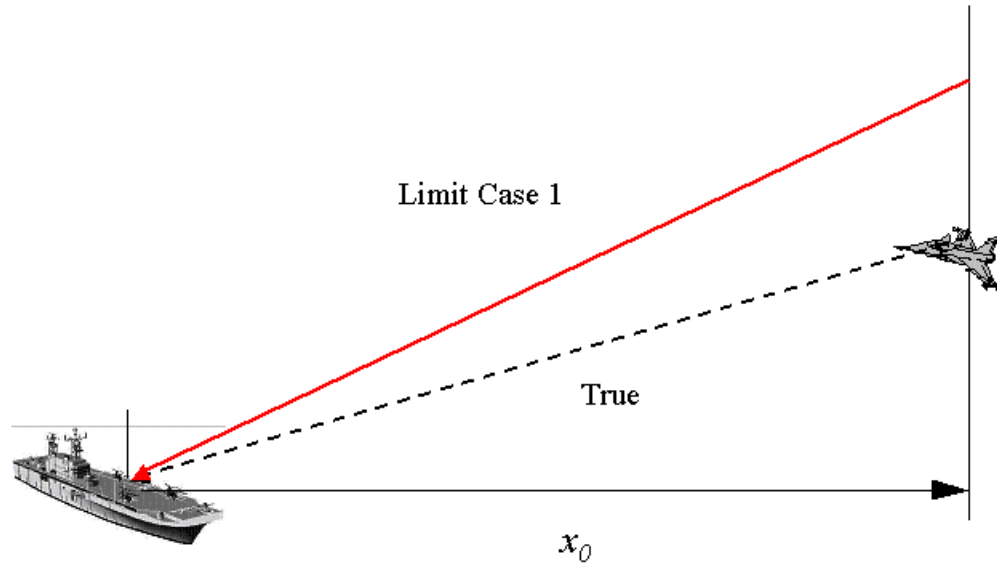


Figure 4.2. Vertical Position Error Due to Orbit Ephemeris Error For Limit Case 1

The relative residual used for detection is

$$\delta r \stackrel{\Delta}{=} r_0 - r = (I - HH^+) \delta H_i u \alpha \quad (4.2)$$

where r_0 is the residual vector at the start (service entry) distance x_0 , r is the residual vector at distance x , and the scalar factor α is defined as $(x_0 - x)/x$. Therefore, at a given distance x , the observable effect of the ephemeris on the residual is magnified by the value of α . From a RAIM interpretation, as illustrated in Figure 4.3, the FMS will

decrease as α increases. We will return to a discussion of the ramifications of the α parameter after Limit Case 2 is developed.

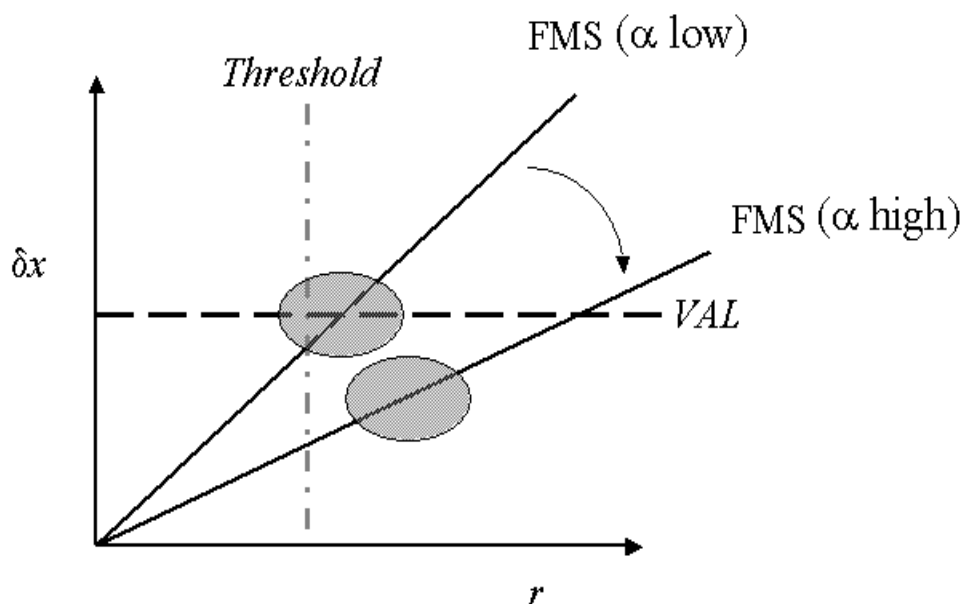


Figure 4.3. Effect of Increasing α

4.3 Limit Case 2

In this scenario, unlike Limit Case 1, orbit ephemeris errors do have an effect on the cycle ambiguity estimation process. In this case, the floating cycle ambiguity estimates will absorb the effective ranging error induced by the ephemeris error. The resulting position error will be small near the effective cycle resolution distance (x_1) because the ephemeris error induced at this distance will be nearly cancelled by the error in the estimated cycle ambiguity. As the aircraft approaches the ship, however, the position error will increase proportionally with the displacement ($x_1 - x$) from the effective cycle resolution point. The maximum position error will occur at the aircraft touch down point

($x = 0$) as shown in Figure 4.4. The mathematical expression for vertical position error in this case is

$$\delta x = H_{3,t}^+ \delta H u x^* \tag{4.3}$$

where $x^* = x_1 - x$, and x_1 is the equivalent cycle resolution distance.

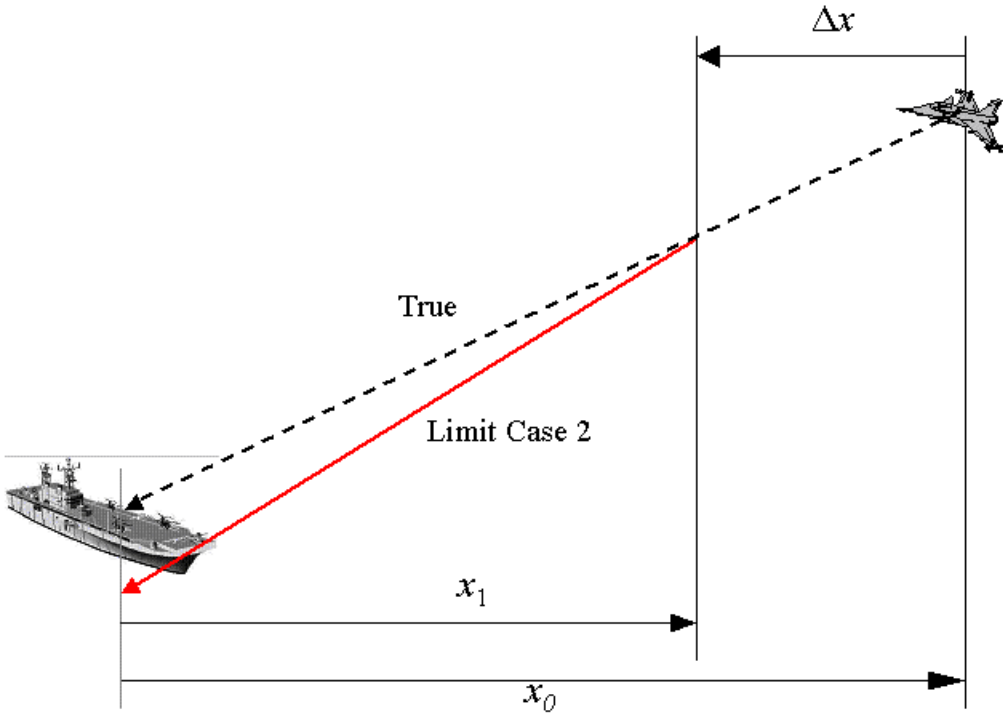


Figure 4.4. Vertical Position Error Due to Orbit Ephemeris Error For Limit Case 2

The relative residual can be computed using Equation (4.4) whose form is identical to (4.2). The difference between the two equations is that x has been replaced by x^* and the scalar factor α is in this case defined to be $(x_0 - x)/x^*$:

$$\delta r \stackrel{\Delta}{=} r_0 - r = (I - HH^+) \delta H_{,u} \alpha x^* \quad (4.4)$$

As qualitatively illustrated in Figure 4.5 for this limiting case, RAIM performance will improve as the distance $x_0 - x_1$ increases because the relative residual will grow larger before the first erroneous CDGPS position fix occurs (at $x = x_1$).

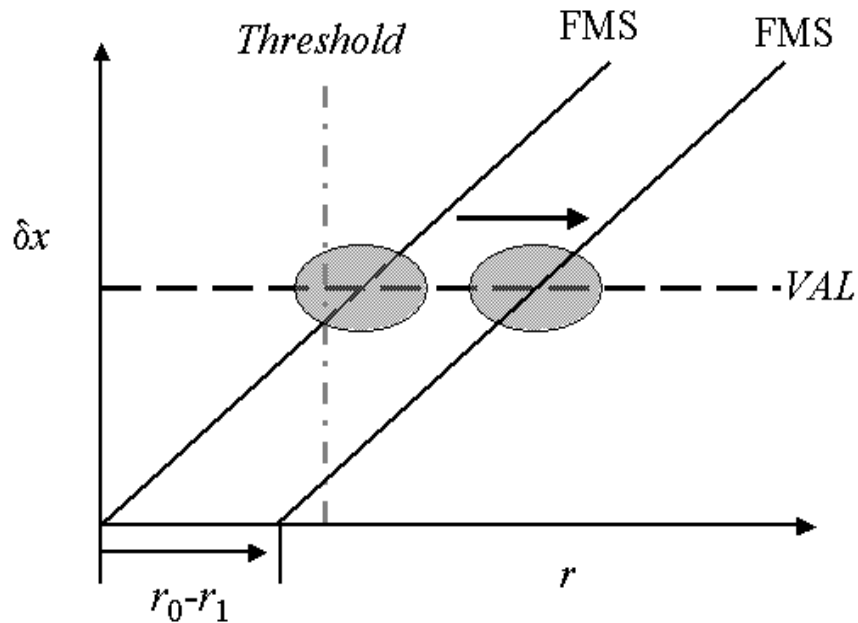


Figure 4.5. Effect on RAIM of Increasing $x_0 - x_1$

4.4 Availability of Ephemeris Error Detection

Because the mathematical structures of Equation Sets (4.1)/(4.2) and (4.3)/(4.4) are identical, it is advantageous to consider both cases simultaneously. In particular, we are interested in the value of α that will result in RAIM availability of 99.7 percent. Recall as α increases, the residual will be magnified relative to the position error for any given geometry; therefore, RAIM availability will be improved. In this regard, Figure 4.6 shows the RAIM availability results as a function of α . (More sensitivity analysis results of ephemeris error detection for different ship locations are shown in Figures G.1-3 in APPENDIX G.) These results assume the worst observed case Central Pacific ship location defined earlier, a missed detection probability of 10^{-4} , single difference $\sigma = 1$ cm, and three different elevation mask angles. The quantitative results clearly show that as α increases, availability is improved. When $\alpha = 5$, the 99.7 percent availability requirement is achieved. We therefore select the desired value $\alpha_{des} = 5$.

Although we want $\alpha \geq \alpha_{des}$ for each of the two limit cases, the interpretation of this requirement is different for each. Using the definition of α for Limit Case 1, it is required that x be smaller than $x_0/(1 + \alpha_{des})$ to ensure RAIM availability. (Conversely, for all distances in excess of $x_0/(1 + \alpha_{des})$, the RAIM function for ephemeris detection is not available with the desired missed detection performance.) Figure 4.7 shows, for several values of α , the maximum distance (x) within which RAIM is available as a function of the service entry distance (x_0). For example, given a service entry distance of 50 nmi, the RAIM-based ephemeris detection is 99.7 percent available ($\alpha = 5$) within a radius of 8.33 nmi of the ship.

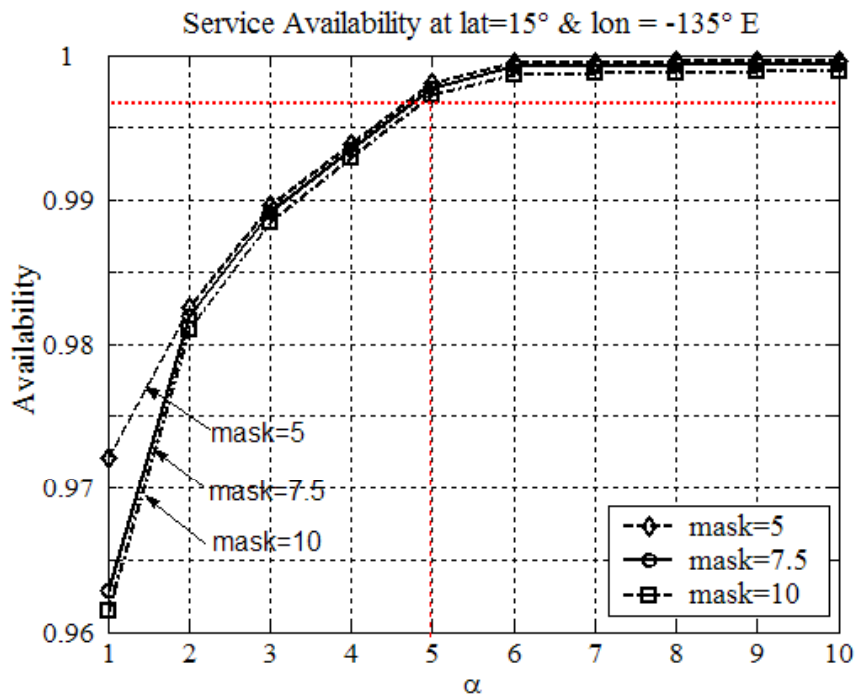
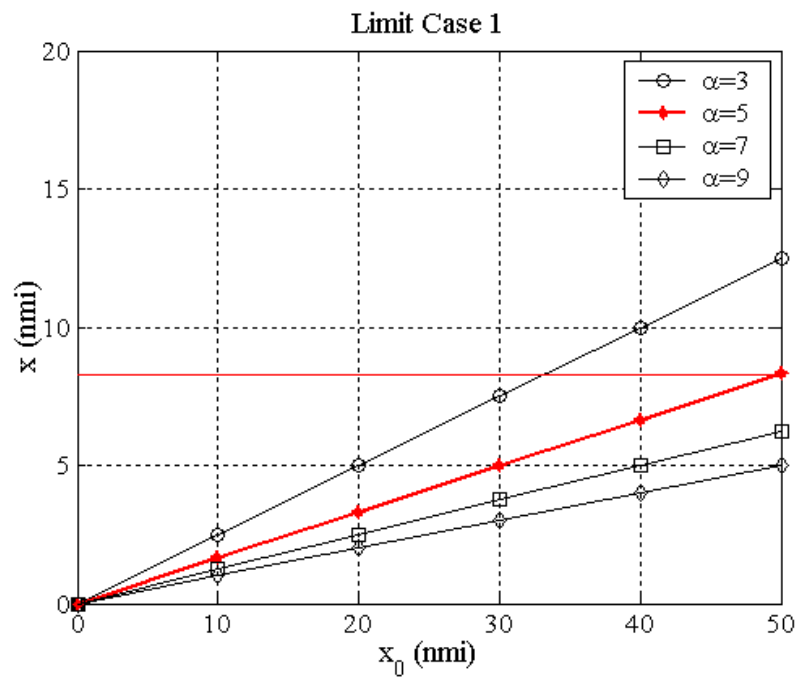


Figure 4.6. Service Availability of Orbit Ephemeris Detection

Figure 4.7. x vs. x_0 for Limit Case 1

Using the definition of α for Limit Case 2, it is required that x_1 (the effective cycle resolution distance) be smaller than x_0/α_{des} to ensure availability for all $x < x_1$. Figure 4.8 shows, for several values of α , the maximum effective cycle resolution distance (x_1) within which RAIM is available as a function of the service entry distance (x_0). For example, given a service entry distance of 50 nmi, the RAIM-based ephemeris detection is 99.7 percent available ($\alpha = 5$) for $x < x_1$, if x_1 is 10 nmi or smaller.

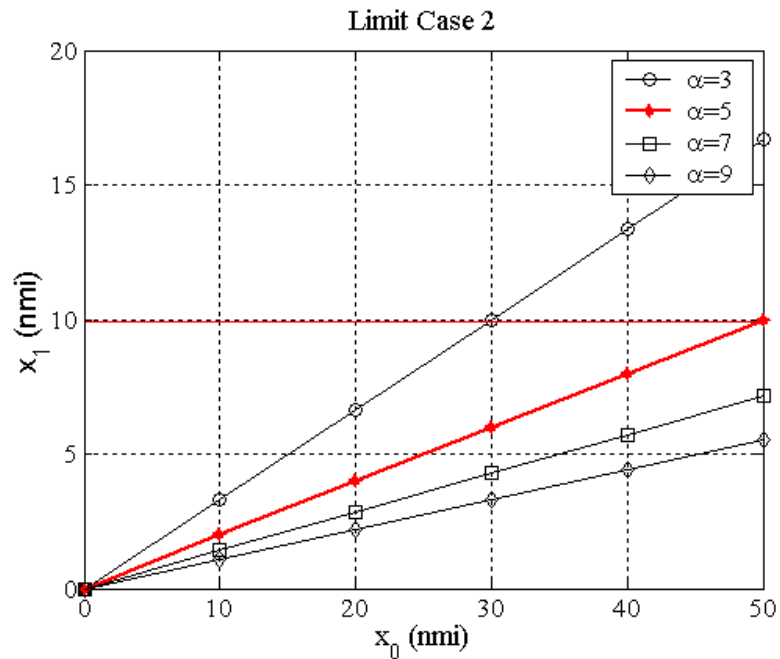


Figure 4.8. x_1 vs. x_0 for Limit Case 2

4.5 Summary of Ephemeris Error Detection

Table 4.1 summarizes the necessary conditions imposed by the two limit cases to achieve 99.7 percent availability ($\alpha = 5$) of the relative RAIM ephemeris fault detection

function. Both conditions should be satisfied to ensure RAIM performance for practical SRGPS navigation architectures.

Table 4.1. Summary of Orbit Ephemeris Error Detection

Required Service Availability	99.7 percent => $\alpha = 5$	
Limit Case	1	2
Necessary Condition	$x < \frac{x_0}{6}$	$x_1 < \frac{x_0}{5}$

CHAPTER 5

IONOSPHERIC ERROR DETECTION

5.1 Introduction

Nominally the effects of ionospheric errors are mitigated by the use of differential GPS. However, large ionospheric spatial gradients will cause differential ranging errors that are dependent on the displacement of the aircraft from the ship. Such sharp gradients are rare, being relatively more common near the auroral and equatorial region where the highest values of range delay are expected. Important prior work in ionospheric gradient detection has focused on code-carrier divergence monitoring [Luo02]. Here, we show that the relative RAIM algorithm discussed above can also be effective against anomalous ionospheric gradients affecting a given satellite. Unfortunately, in contrast to ephemeris failures, ionospheric gradient anomalies can potentially occur on multiple satellites simultaneously. (This is not the case for orbit errors since ephemeris data for each satellite is uploaded independently and at different times.) Nevertheless, because dual frequency measurements will nominally be available with SRGPS, it is possible to use carrier phase measurements to directly detect anomalous ionospheric gradients in real-time during the aircraft approach. Moreover, the SRGPS user can also observe the anomalous ionospheric gradient with single frequency measurements (for example, when interference or jamming are present on one frequency). This is true because of the divergence effect of the ionosphere on code and carrier measurements. In this section, we consider an ionospheric threat model consisting of an anomalously large, constant spatial gradient during the approach. (More complex threat models, such as abrupt, non-linear

changes in ionospheric delay during the approach, will be addressed in future work.) A means for autonomous detection of ionospheric spatial gradients will be described and the effectiveness of the detection algorithms will be explicitly quantified.

5.2 Direct Observation Method

In this section, the differential ionospheric gradient estimation using the single and dual frequency GPS measurements will be described.

5.2.1 Dual Frequency Gradient Estimation. Assuming that a linear gradient model of the differential ionosphere is applicable for each satellite, the magnitude of the gradient can be directly observed using dual frequency measurements taken over the aircraft approach. Taking the difference between L1 and L2 single difference carrier phase measurements when the aircraft is at a distance x from the reference station, we have, for a given satellite,

$$\lambda_{L1}\Delta\phi_{L1} - \lambda_{L2}\Delta\phi_{L2} = (1 - \gamma_{12})kx + bias + \nu \quad (5.1)$$

where k is the differential L1 ionospheric gradient for the satellite, ν is the nominal differential measurement error (assumed to be normally distributed with standard deviation σ_ν), and γ_{12} is equal to $f_{L1}^2/f_{L2}^2 = 1.65$. We can estimate the gradient by applying Equation (5.1) at the service entry distance x_0 and again at some distance x (where $x < x_0$) later during the approach, differencing the results, and dividing by $(\gamma_{12} - 1)(x_0 - x)$. The resulting ionospheric gradient estimate is distributed as

$$\hat{k} \sim N\left(k, \frac{\sigma_{\Delta I, dual}^2}{(x_0 - x)^2}\right) \quad (5.2)$$

where $\sigma_{\Delta I, dual} = \frac{\sqrt{2}}{0.65} \sigma_v$.

5.2.2 Single Frequency Gradient Estimation. The ionospheric gradient can be also directly (but less precisely) estimated using single frequency measurements. Taking the difference between code and carrier single difference measurements when the aircraft is at a distance x from the reference station, we have, for a given satellite,

$$\Delta\rho - \lambda_{L1} \Delta\phi = 2kx + bias + v_{\rho-\phi} \quad (5.3)$$

Following the process above, we estimate the gradient by applying Equation (5.3) at the service entry distance x_0 and again some distance x later during the approach, difference the results, and divide by $2(x_0 - x)$. The resulting ionospheric gradient estimate is distributed as

$$\hat{k} \sim N\left(k, \frac{\sigma_{\Delta I, \rho-\phi}^2}{(x_0 - x)^2}\right) \quad (5.4)$$

where $\sigma_{\Delta I, \rho-\phi} = \frac{\sqrt{2}}{2} \sigma_{\rho-\phi}$.

5.3 Effect of Ionospheric Gradient on Carrier Phase Positioning

As was the case with ephemeris failures, the existence of an anomalous ionospheric gradient may also affect the cycle ambiguity estimation process. In turn, incorrectly estimated cycle ambiguities can be used later during the approach to compute incorrect user (aircraft) position. To bound the position error caused by ionospheric gradient anomalies, we again consider the two limiting cases for cycle estimation already defined.

Let us assume that the effective cycle resolution distance is x_1 and the cycle resolution error due to the existence of the ionospheric gradient is δN . In this case, the effective single difference carrier ranging error experienced at a distance x from the ship is

$$\delta\phi(x) = -\delta N - kx \quad (5.5)$$

where nominal carrier phase measurement errors are neglected for the moment. The error in the cycle ambiguity, δN , will differ for the two limit-case cycle estimation scenarios. Table 5.1 shows the cycle ambiguity estimate errors along with the effective ranging error at $x = 0$ and $x = x_1$ computed from Equation (5.5) for the two limiting cases. (Appendix C provides additional detail). Figure 5.1 is an illustration of the corresponding

Table 5.1. Cycle Resolution and Effective Ranging Measurement Errors

Limit Case	δN	$\delta\phi(0)$	$\delta\phi(x_1)$
1	$-2kx_1$	$2kx_1$	kx_1
2	$-kx_1$	kx_1	0

position error histories. Because Limit Case 1 results in worse position errors throughout the approach, only this case will be considered in the analysis that follows.

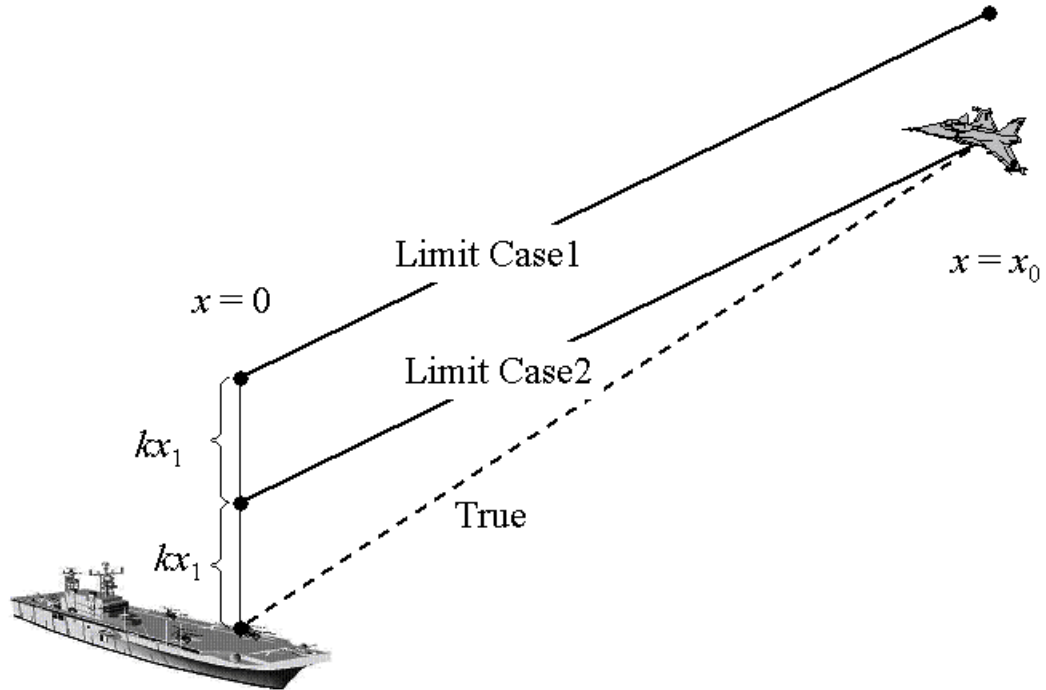


Figure 5.1. Illustrated Position Error Histories Due to Ionospheric Gradient

5.4 Availability of Ionospheric Gradient Detection

Substituting the value of δN for Limit Case 1 in Table 5.1 into the ranging error Equation (5.5), it is possible to write an upper bound on vertical position error as

$$\delta x = \left\| H_{3:1}^+ \right\| b\beta + v_x \quad (5.6)$$

where the following definitions are relevant:

1. $\|H_{3,:}^+\|_1$ is the 1-norm of $H_{3,:}^+$
2. $b \equiv \frac{k_{\max}(x_0 - x)}{\sigma_{\Delta I}}$
3. $\beta \equiv \frac{(2x_1 - x)}{x_0 - x} \sigma_{\Delta I}$ (5.7)
4. $v_x \sim N(0, (H^T H)_{3,3}^{-1} \sigma^2)$, and σ^2 is the single difference measurement variance
5. k_{\max} is the maximum value of the ionospheric gradient for any satellite in view.

The value of $\sigma_{\Delta I}$, defined just below Equations (5.2) and (5.4), will depend on whether dual frequency or single frequency measurements are used to estimate ionospheric gradient. The normalized test statistic used for detection is

$$r \equiv \frac{\hat{k}_{\max}(x_0 - x)}{\sigma_{\Delta I}} = b + \tilde{v}_k \quad (5.8)$$

where $\tilde{v}_k \sim N(0, 1)$ is the normalized test static error.

As the ionospheric gradient (k_{\max}) increases, b also increases, and both the position error, Equation (5.6), and the test statistic, Equation (5.8), become larger. In this case, we wish to find the value of β to attenuate the effect of b on position error such that the availability of the detection function meets the target requirements. The detection function availability results are plotted as a function of β in Figure 5.2 for an elevation

mask of 10 deg. It is evident that values of β smaller than or equal to 0.015 m for the nominal dual frequency case, and 0.0185 m for the single frequency case, will ensure

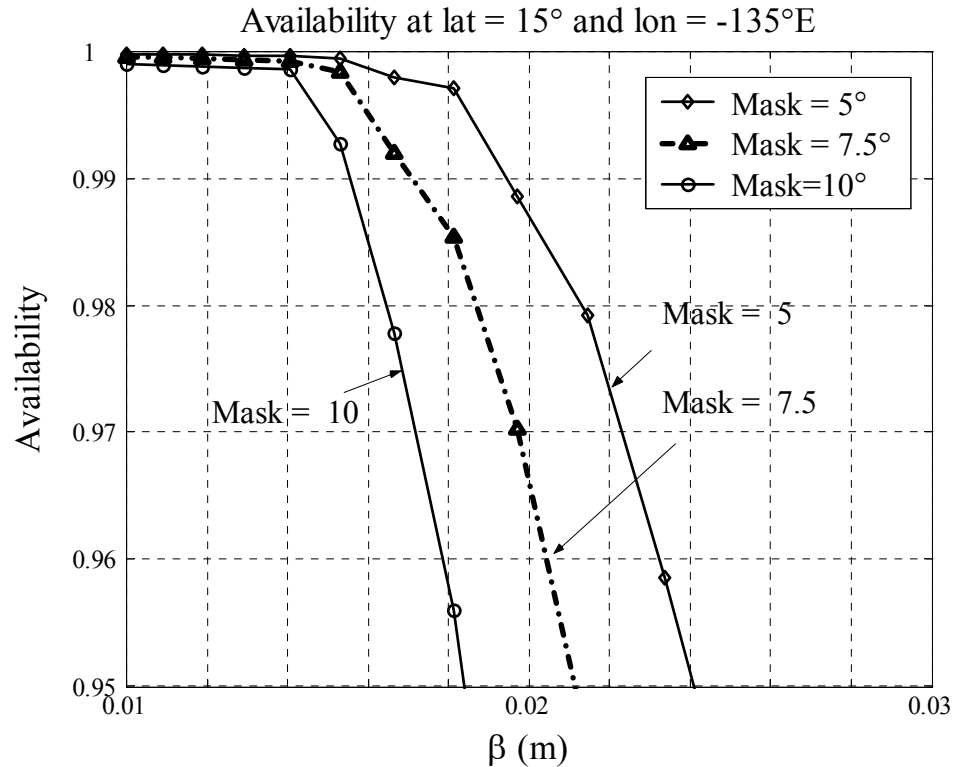


Figure 5.2. Service Availability vs. β

sufficient detection function availability for the SRGPS application. We therefore define $\beta_{req} = 0.015$ and 0.0185 meters for dual and single frequency cases, respectively. More sensitivity analysis results of ionospheric error detection for different ship locations are shown in Figures H.1-3 in Appendix H.

Given the definition of β in Equation (5.7) and its required value (β_{req}) to ensure availability we are able to define necessary conditions on cycle resolution distance as follows:

$$\frac{\beta_{req}}{\sigma_{\Delta}} > 1: \quad \frac{x_1}{x_0} \leq \frac{\beta_{req}/\sigma_{\Delta}}{1 + \beta_{req}/\sigma_{\Delta}} \quad , \quad (5.9)$$

and

$$\frac{\beta_{req}}{\sigma_{\Delta}} < 1: \quad \frac{x_1}{x_0} \leq \frac{\beta_{req}}{2\sigma_{\Delta}} \quad . \quad (5.10)$$

These constraints are expressed graphically in Figure 5.3. For example, given $\sigma_{\Delta, dual} = 0.03$ m (for the nominal dual frequency case) and $\sigma_{\Delta, \rho-\phi} = 0.2$ m (for the single frequency case), and also assuming a service entry distance (x_0) of 50 nmi, hazardous ionospheric gradients are detectable when the effective cycle resolution distance (x_1) is less than 2.3 nmi for the single-frequency case and 12.5 nmi for dual frequency. The results for other values of x_0 are shown in Figure 5.4.

5.5 Summary of Ionospheric Error Detection

The availability performance of autonomous ionospheric error detection using direct GPS measurements is encapsulated in Table 5.2. In summary, necessary conditions to ensure fault detection availability for both dual and single frequency implementations were defined.

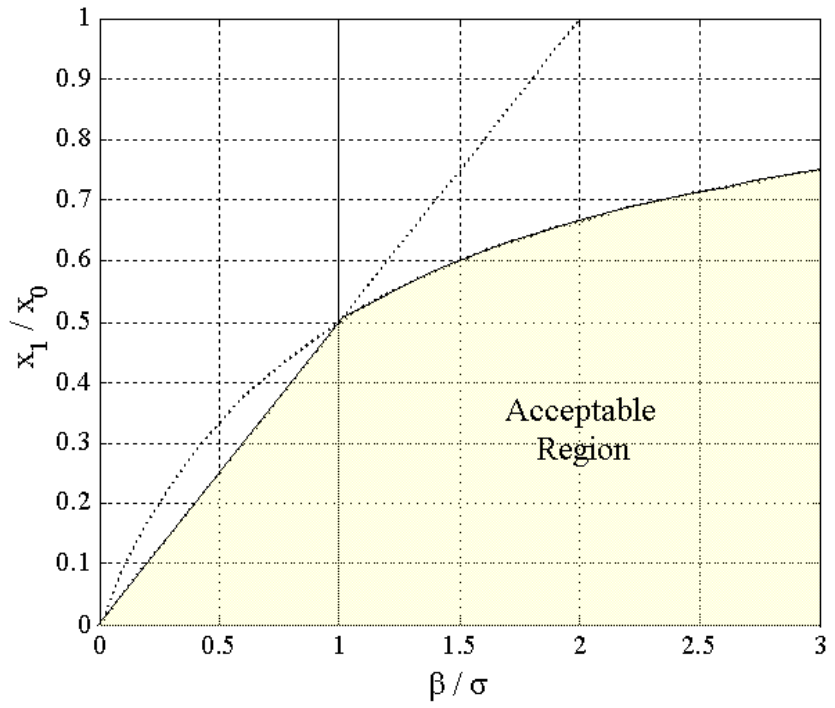


Figure 5.3. Constraint on Cycle Resolution Distance

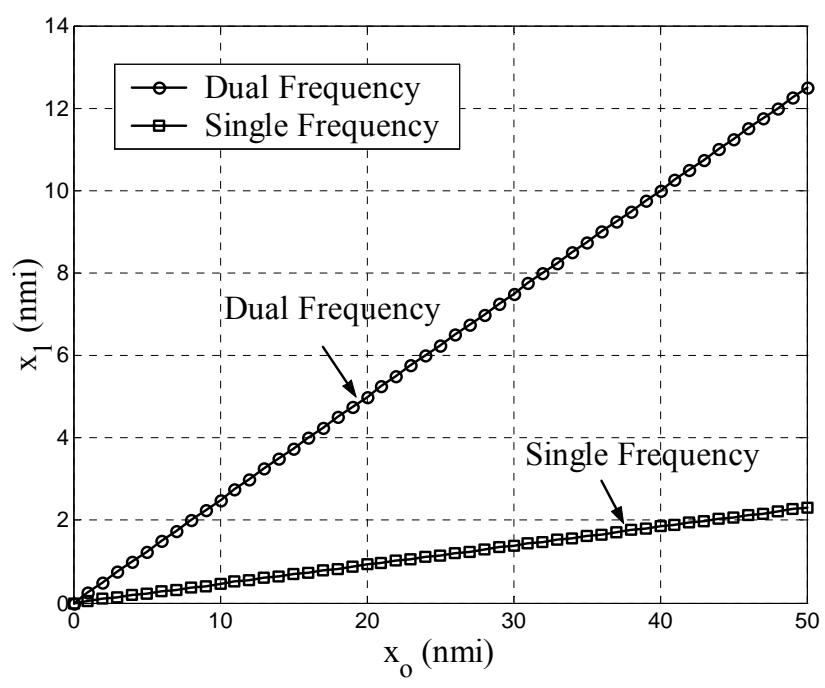


Figure 5.4. Maximum Effective Cycle Resolution Distance Constraint

Table 5.2. Summary of Ionospheric Error Detection

	Single-Frequency	Dual Frequency
Required Service Availability	95 Percent	99.7 Percent
Ionospheric Error (Worst Case)	Limit Case 1	Limit Case 1
β_{des}	0.015	0.0185
Required Maximum Effective Cycle Resolution Distance	$x_1 < 2.3$ nmi	$x_1 < 12.5$ nmi

CHAPTER 6

ROBUST NAVIGATION ALGORITHMS

6.1 Introduction

In previous work [Pervan03b], it was assumed that the filtering of single or double difference ranging measurements was initiated upon aircraft entry into the SRGPS service volume—i.e., within the broadcast range of the shipboard data link. However, it was also noted that it is possible to begin code-carrier smoothing much earlier. For dual-frequency systems such as SRGPS, the effect of prior measurement filtering can be especially important because long filter time constants can be used [Hwang99]. One significant implication of such *pre-filtering* is that system requirements on receiver ranging error and/or data broadcast radius can be significantly relaxed. Another is that an SRGPS solution that does not rely on a large data broadcast radius will be implicitly more robust to spatial decorrelation (tropospheric and ionospheric) error model assumptions.

This research is focused on the design of robust airborne algorithms for SRGPS terminal navigation. In this context, a processing methodology is defined to optimally combine the complementary benefits of geometry-free filtering and geometric redundancy. Specifically, when the aircraft is far from the ship (inside or outside the SRGPS service volume), geometry-free filtering is used for cycle estimation of widelane integers. For dual frequency implementations, the advantage of code/carrier divergence-free filtering prior to SRGPS service volume entry can be especially significant because long filter durations can be used.

In contrast, the use of geometric redundancy for cycle resolution is restricted to the service volume (where the aircraft has access to shipboard reference measurements) and is most robust to ionospheric and tropospheric decorrelation when the displacement between the aircraft and ship is small. Thus, only when the aircraft is near the ship, can carrier phase geometric-redundancy be safely exploited for cycle estimation of any remaining widelane integers and, if needed, L1 and L2 integers. By processing this way, performance is enhanced due to the long duration of code measurement filtering, and cycle resolution is robust to spatial decorrelation error model assumptions (because geometric redundancy is used only when the baseline distance is short).

In this chapter, the robust navigation architecture is detailed and its performance is evaluated relative to the navigation integrity requirements for shipboard landing of aircraft.

6.2 Geometry-free code-carrier Filtering

In pre-filtering processing at the aircraft, geometry-free code-carrier filtering is executed prior to service volume entry and within the service volume until the aircraft is close to the ship. At the shipboard reference station, the same filter operates continuously.

At a given time index k at the aircraft or ship, the differenced L1 carrier measurement between two satellites (i and j) is

$$\lambda_{L1} \Delta \phi_{L1}^{ij}(k) = \Delta \rho_T^{ij}(k) - \Delta I^{ij}(k) + \lambda_{L1} \Delta N_{L1}^{ij} + v_{\Delta \phi, L1}^{ij}(k) \quad (6.1)$$

where,

$\Delta\rho_T^{ij}$ is the difference between of the sums of the true ranges, tropospheric delays, and satellite clock biases for satellites i and j ,

ΔI^{ij} is the differential ionospheric propagation delay for the satellites at L1,

ΔN_{L1}^{ij} is the differential cycle ambiguity, and

$\nu_{\Delta\phi,L1}^{ij}$ is the differential measurement noise, which is assumed to be normally distributed with zero-mean and standard deviation $\sigma_{\Delta\phi,L1}^{ij}$.

The differenced code phase (pseudorange) measurement between satellites is identical to Equation (6.1) except the cycle ambiguity term is absent, the ionospheric term is opposite in sign, and the standard deviation of the measurement noise is $\sigma_{\Delta PR,L1}^{ij}$.

Nominally, L2 measurements will be available with SRGPS as well. The mathematical expressions for these additional measurements follow:

$$\Delta PR_{L1}^{ij}(k) = \Delta\rho_T^{ij}(k) + \Delta I^{ij}(k) + \nu_{\Delta PR,L1}^{ij}(k) \quad (6.2)$$

$$\lambda_{L2}\Delta\phi_{L2}^{ij}(k) = \rho_T^{ij}(k) - \gamma_{12}\Delta I^{ij}(k) + \lambda_{L2}N_{L2}^{ij} + \nu_{\Delta\phi,L2}^{ij}(k) \quad (6.3)$$

$$\Delta PR_{L2}^{ij}(k) = \rho_T^{ij}(k) + \gamma_{12}\Delta I^{ij}(k) + \nu_{\Delta PR,L2}^{ij}(k) \quad (6.4)$$

where ΔPR_{L2}^{ij} is the differenced L2 code phase measurement for satellites i and j and γ_{12} is already defined under Equation (2.10). Equations (6.1)-(6.4) can be stacked as follows

$$\begin{bmatrix} \lambda_{L1} \Delta \phi_{L1}^{ij} \\ \lambda_{L2} \Delta \phi_{L2}^{ij} \\ \lambda_{L1} \Delta PR_{L1}^{ij} \\ \lambda_{L2} \Delta PR_{L2}^{ij} \end{bmatrix} = \begin{bmatrix} 1 & -1 \\ 1 & -\gamma_{12} \\ 1 & 1 \\ 1 & \gamma_{12} \end{bmatrix} \begin{bmatrix} \Delta \rho_T^{ij} \\ \Delta I^{ij} \end{bmatrix} + \begin{bmatrix} \lambda_{L1} & 0 \\ 0 & \lambda_{L2} \\ 0 & 0 \\ 0 & 0 \end{bmatrix} \begin{bmatrix} \Delta N_{L1}^{ij} \\ \Delta N_{L2}^{ij} \end{bmatrix} + \begin{bmatrix} \Delta v_{\Delta \phi, L1}^{ij} \\ \Delta v_{\Delta \phi, L2}^{ij} \\ \Delta v_{\Delta PR, L1}^{ij} \\ \Delta v_{\Delta PR, L2}^{ij} \end{bmatrix}. \quad (6.5)$$

For simplicity of notation, Equation (6.5) is rewritten as

$$z = A \begin{bmatrix} \Delta \rho_T^{ij} \\ \Delta I^{ij} \end{bmatrix} + B \begin{bmatrix} \Delta N_{L1}^{ij} \\ \Delta N_{L2}^{ij} \end{bmatrix} + v_{zz}. \quad (6.6)$$

$$\text{where } A = \begin{bmatrix} 1 & -1 \\ 1 & -\gamma_{12} \\ 1 & 1 \\ 1 & \gamma_{12} \end{bmatrix}, B = \begin{bmatrix} \lambda_{L1} & 0 \\ 0 & \lambda_{L2} \\ 0 & 0 \\ 0 & 0 \end{bmatrix}, \text{ and } v_{zz} = \begin{bmatrix} \Delta v_{\Delta \phi, L1}^{ij} \\ \Delta v_{\Delta \phi, L2}^{ij} \\ \Delta v_{\Delta PR, L1}^{ij} \\ \Delta v_{\Delta PR, L2}^{ij} \end{bmatrix}.$$

Since we are only interested in extracting information on the cycle ambiguities in the pre-filtering phase, Equation (6.6) can be further simplified by pre-multiplying both sides of the equation by a matrix L_p , whose rows form a basis for the left null space of the matrix A :

$$L_p z = L_p B \begin{bmatrix} \Delta N_{L1}^{ij} \\ \Delta N_{L2}^{ij} \end{bmatrix} + L_p v. \quad (6.7)$$

The error in the estimate of differential cycle ambiguities obtained from solving Equation (6.7) is described by the covariance matrix

$$P_{\Delta N} = \left(H_f^T R_e^{-1} H_f \right)^{-1} \quad (6.8)$$

where $H_f = L_p B$, $R_e = L_p V_v L_p^T$, and V_v is the 4×4 diagonal matrix

$$V_v = \begin{bmatrix} (\sigma_{\Delta\phi, L1}^{ij})^2 & 0 & 0 & 0 \\ 0 & (\sigma_{\Delta\phi, L2}^{ij})^2 & 0 & 0 \\ 0 & 0 & (\sigma_{\Delta PR, L1}^{ij})^2 & 0 \\ 0 & 0 & 0 & (\sigma_{\Delta PR, L2}^{ij})^2 \end{bmatrix}. \quad (6.9)$$

In this work, we assume that $\sigma_{\Delta\phi, L1}^{ij} = \sigma_{\Delta\phi, L2}^{ij} \equiv \sigma_{\Delta\phi}$ and $\sigma_{\Delta PR, L1}^{ij} = \sigma_{\Delta PR, L2}^{ij} \equiv \sigma_{\Delta PR}$. An eigenvector decomposition of covariance matrix $P_{\Delta N}$ can be expressed assuming $\sigma_{\Delta\phi} = 1\text{cm}$ and $\sigma_{\Delta PR} = 30\text{cm}$:

$$evalue = \begin{bmatrix} 0.03113 & 0 \\ 0 & 129.71 \end{bmatrix} \quad evector = \begin{bmatrix} 0.70444 & -0.70977 \\ -0.70977 & -0.70444 \end{bmatrix} \quad (6.10)$$

where *evalue* is the eigenvalue of $P_{\Delta N}$, and *evector* is the eigenvector of $P_{\Delta N}$. The analysis result reveals that observability of the individual cycle ambiguities, ΔN_{L1}^{ij} and ΔN_{L2}^{ij} , using Equation (6.7) is poor, but that relatively strong information on the widelane ambiguity, $\Delta N_{L1}^{ij} - \Delta N_{L2}^{ij}$, is gained (See Appendix E for the mathematical derivation.) Widelane ambiguity observability can be greatly enhanced by filtering observable Equation (6.7) over time. Therefore, it is interesting to consider whether a navigation architecture based on knowledge of widelane integers (rather than the individual L1 and

L2 cycle ambiguities) is sufficient to meet SRGPS requirements. This question is answered in the analysis that follows.

Figure 6.1 shows the availability of Vertical Dilution of Precision (VDOP) using only satellites that have been in view for different pre-filtering durations. In Figure 6.1, the vertical axis defines the fraction of time that the VDOP is equal to or smaller than the values defined on the horizontal axis. For this plot a representative central Pacific location (22 deg N, 158 deg W) and 7.5 deg elevation mask angle were used. The effect of depleted GPS satellite constellations was also included in these results using the same constellation state probability model as in Chapter 2. The values in parenthesis next to

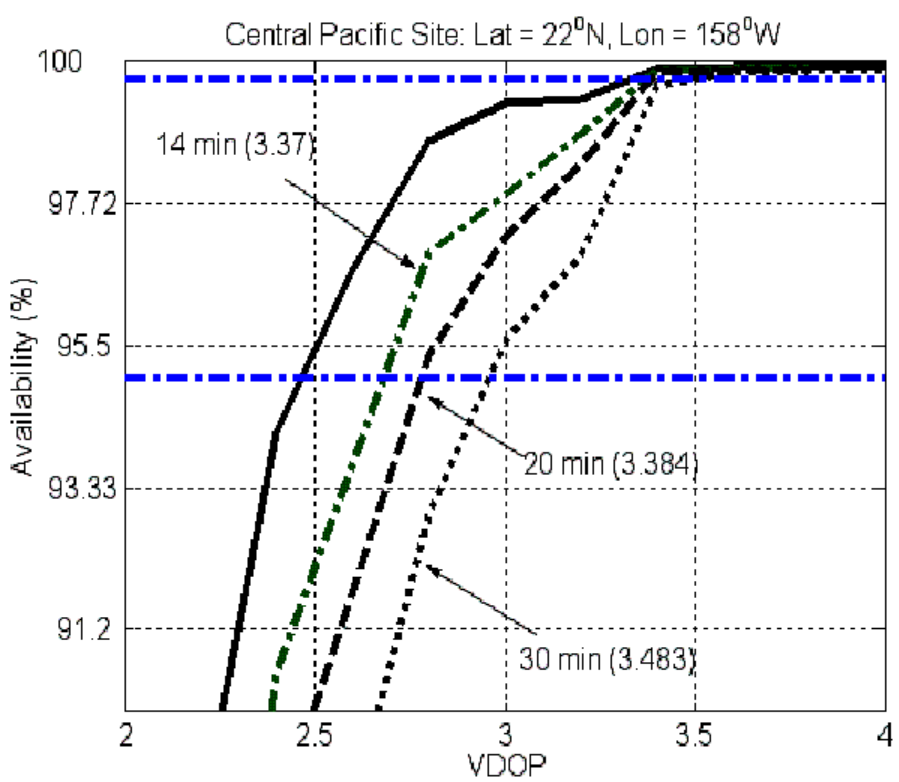


Figure 6.1. Availability vs. VDOP

each curve in Figure 6.1, are the maximum $VDOP$ s that must be managed in order to meet the SRGPS availability requirement of 99.7% using only satellites that have been available for the entire specified pre-filtering time.

Given the required $VDOP$ to meet the SRGPS availability specification, and assuming for the moment that the widelane integers are known and fixed, it is possible to compute the maximum permissible standard deviation for the widelane single difference carrier phase:

$$VPL = \sigma_{\Delta\phi,w} \cdot VDOP \cdot K_{ffd} < 1.1 \text{ m} \quad (6.11)$$

where VPL is the vertical protection level, $\sigma_{\Delta\phi,w}$ is the standard deviation for the widelane single difference carrier phase, and $K_{ffd} = 5.33$ is the integrity multiplier corresponding to the integrity risk requirement of 10^{-7} .

The relevance of inequality Equation (6.11) is readily seen through a simple example. Using only satellites that have been available for 30 minutes of pre-filtering or longer, the maximum $VDOP$ (to ensure 99.7% availability) is 3.483. In this case, using Equation (6.11), it is required that $\sigma_{\Delta\phi,w} < 5.93\text{cm}$. Recall that the relationship between the single difference carrier and single difference widelane carrier standard deviation is

$$\sigma_{\Delta\phi,W} = 5.74\sigma_{\Delta\phi}, \quad (6.12)$$

where $\sigma_{\Delta\phi}$ is the single difference carrier standard deviation (for both L1 and L2). Therefore, the required value of $\sigma_{\Delta\phi}$ is 1.03 cm or less, which is easily achievable using modern GPS receivers.

In this simple analysis to determine the required value of $\sigma_{\Delta\phi}$, it was assumed that the widelane integers were known given 30 minutes of pre-filtering of observable Equation (6.7). We now turn our attention to determine the required value of the raw code difference standard deviation ($\sigma_{\Delta PR}$) to ensure that the cycle likelihood of incorrect cycle resolution is consistent with SRGPS integrity requirements. Figure 6.2 quantifies the sensitivity of floating widelane ambiguity estimate error, σ_w , to $\sigma_{\Delta PR}$, given that

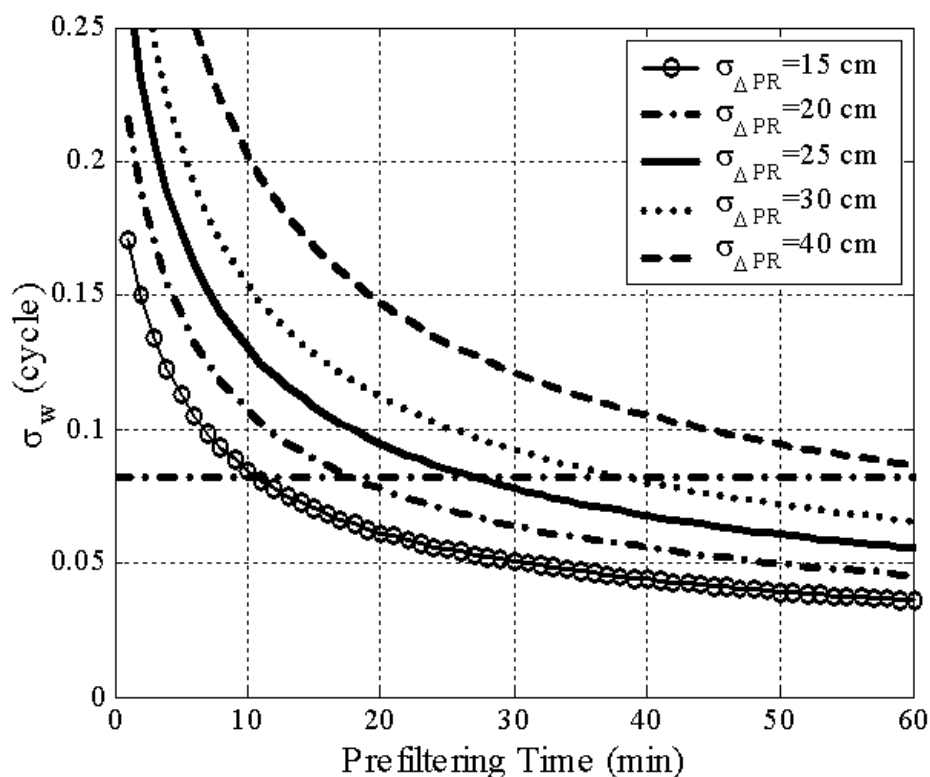


Figure 6.2. Widelane Cycle Resolution

$\sigma_{\Delta\phi}=1$ cm. The dashed-dot horizontal line in the figure is the minimum value of σ_w required to ensure a 10^{-8} total probability of incorrect integer rounding for eight satellites. In these results, code phase error was modeled as a first-order Gauss-Markov random process with a time constant of one minute. (Details of the error model are discussed in Appendix D.) As an example, given a geometry-free filtering duration of 30 minutes, the widelane integers can be fixed with the specified integrity only if $\sigma_{\Delta PR}$ is 27 cm or smaller.

This requirement for raw code error is stringent, but may be achievable using state-of-the-art receivers and antennas currently under development for SRGPS. Nevertheless, in the sections that follow we will show that this requirement can be relaxed by exploiting geometric redundancy when the aircraft is close to the ship, and processing L1 and L2 measurements directly (rather than widelane only). In addition, we will also quantify the sensitivity of performance to $\sigma_{\Delta\phi}$ and $\sigma_{\Delta PR}$, code error time constant, and pre-filtering time.

The output of the pre-filtering process at both the aircraft and ship is a vector of floating widelane cycle ambiguity estimates,

$$\Delta\hat{N}_w = \begin{bmatrix} \Delta\hat{N}_w^{12} \\ \vdots \\ \Delta\hat{N}_w^{1n} \end{bmatrix}, \quad (6.13)$$

where n is the number of satellites, and a satellite which has been in view for the entire pre-filtering duration (arbitrarily chosen to be satellite index 1 here) is selected as the

master for differencing. Because pre-filtering is a double difference geometry-free process, the associated estimate error covariance matrix, $P_{\Delta N,w}$, is not diagonal. Pre-filtering data from the aircraft and ship may be combined when the aircraft is close to the ship to obtain the double difference cycle ambiguity vector

$$\nabla\Delta\hat{N}_w = \begin{bmatrix} \nabla\Delta\hat{N}_w^{12} \\ \vdots \\ \nabla\Delta\hat{N}_w^{1n} \end{bmatrix} \quad (6.14)$$

and associated covariance matrix $P_{\nabla\Delta N,w} = P_{\Delta N,w_{air}} + P_{\Delta N,w_{ship}}$.

6.3 Double Difference Widelane Landing

Within the SRGPS service volume, the double difference carrier phase measurements for L1 and L2 can be written as follows:

Carrier phase L1:

$$\lambda_{L1}\nabla\Delta\phi_{L1}^{ij} = -(e^{iT} - e^{jT})x - \nabla\Delta I^{ij} + \nabla\Delta T^{ij} + \lambda_{L1}\nabla\Delta N_{L1}^{ij} + v_{\nabla\Delta\phi,L1}^{ij} \quad (6.15)$$

Carrier phase L2:

$$\lambda_{L2}\nabla\Delta\phi_{L2}^{ij} = -(e^{iT} - e^{jT})x - \beta_\phi\nabla\Delta I^{ij} + \nabla\Delta T^{ij} + \lambda_{L2}\nabla\Delta N_{L2}^{ij} + v_{\nabla\Delta\phi,L2}^{ij} \quad (6.16)$$

where,

e^i is the line of sight vector to the satellite i ,

x is the aircraft position vector relative to the ship,

$\nabla\Delta I^{ij}$ is the double difference ionospheric propagation delay for the satellites at L1,

$\nabla\Delta T^{ij}$ is the double difference tropospheric delay, and

ν^{ij} terms are the double difference code and carrier measurement errors due to receiver noise and multipath.

When the aircraft is close to the ship (within about 0.25 nmi), the tropospheric and ionospheric spatial decorrelation errors are negligible.

Given the L1 and L2 double difference measurements in Equations (6.15) and (6.16), the double difference widelane code and carrier measurements can be constructed as follows:

Carrier Widelane:

$$\lambda_w \nabla\Delta\phi_w^{ij} = \lambda_w (\nabla\Delta\phi_{L1}^{ij} - \nabla\Delta\phi_{L2}^{ij}) = -(e^{iT} - e^{jT})x + \lambda_w \nabla\Delta N_w^{ij} + \nu_{\nabla\Delta\phi,w}^{ij} \quad (6.17)$$

where the widelane wavelength, λ_w , is defined under Equation (2.11), $\nabla\Delta N_w^{ij}$ is the double difference widelane integer for satellites i and j , and $\nu_{\nabla\Delta\phi,w}^{ij}$ are the double difference widelane carrier measurement errors due to receiver noise and multipath. The widelane measurement equations (6.17) can also be expressed in vector form as follows:

$$[\nabla\Delta\phi_w] = \begin{bmatrix} G_{(n-1)\times 3} & I_{(n-1)\times(n-1)} \end{bmatrix} \begin{bmatrix} x_{3\times 1} / \lambda_w \\ \nabla\Delta N_{w,(n-1)\times(n-1)} \end{bmatrix} + \nu \quad (6.18)$$

where $x_{3 \times 1}$ is the 3×1 aircraft position vector relative to the ship, $\nabla \Delta N_{w, (n-1) \times (n-1)}$ is the $(n-1) \times (n-1)$ double difference widelane integer vector, $I_{(n-1) \times (n-1)}$ is the $(n-1) \times (n-1)$ identity matrix, and $G_{(n-1) \times 3}$ is the $(n-1) \times 3$ geometry matrix

$$G_{(n-1) \times 3} = \begin{bmatrix} -\left(e^{1T} - e^{2T}\right) \\ \vdots \\ -\left(e^{1T} - e^{nT}\right) \end{bmatrix}^T. \quad (6.19)$$

It is relatively simple to fuse the output of the pre-filtering process into double difference widelane positioning because the output of the former is the floating double difference widelane cycle ambiguity vector:

$$\begin{bmatrix} \nabla \Delta \hat{N}_w^{12} \\ \vdots \\ \nabla \Delta \hat{N}_w^{1n} \end{bmatrix} = I_{(n-1) \times (n-1)} \begin{bmatrix} \nabla \Delta N_w^{12} \\ \vdots \\ \nabla \Delta N_w^{1n} \end{bmatrix} + v_N \quad (6.20)$$

where $\nabla \Delta \hat{N}_w^{1n}$ is the floating double difference widelane cycle ambiguity estimate for satellites 1 and n obtained as a result of pre-filtering, $\nabla \Delta N_w^{1n}$ is the true double difference widelane integer, and v_N is the cycle ambiguity estimate error from pre-filtering, which has covariance matrix $P_{\nabla \Delta N, w}$. The initialized covariance corresponding to the integers in the position estimation is updated with the sensor noise. Depending on the duration of pre-filtering for the individual satellites, it may be possible to round widelane ambiguities. In this regard, all possible cycle ambiguities are fixed subject to the

constraint that the probability of having any one incorrect integer is lower than 10^{-8} (comfortably below the overall integrity risk requirement). For the remaining cycle ambiguities, the floating estimates (and variances) must be retained.

Given the available knowledge on the double difference widelane cycle ambiguities from pre-filtering and rounding processes, the aircraft vertical position estimate error standard deviation can be computed using Equations (6.18) and (6.20). System availability is then evaluated by comparing these results to the VAL.

SRGPS availability has been evaluated for the various values of single difference carrier and code phase measurement error standard deviation for a central Pacific ship location (22 deg N and 128 deg W). The satellite outage state probability model in Table 3.1 and a 7.5 deg elevation mask angle were assumed in this analysis. Figures 6.3 to 6.5 quantify the sensitivity of availability to the pre-filtering duration, which is expressed in terms of the nondimensional ratio

$$\psi = \frac{t_f}{\tau} \quad (6.21)$$

where t_f is the filtering time, and τ is the code measurement error time constant. Results were computed for three different values of the ratio ψ (20, 30, and 40). The performance of the pre-filtering process is sensitive to this nondimensional ratio because it defines the maximum effective number of independent measurement updates available during pre-filtering.

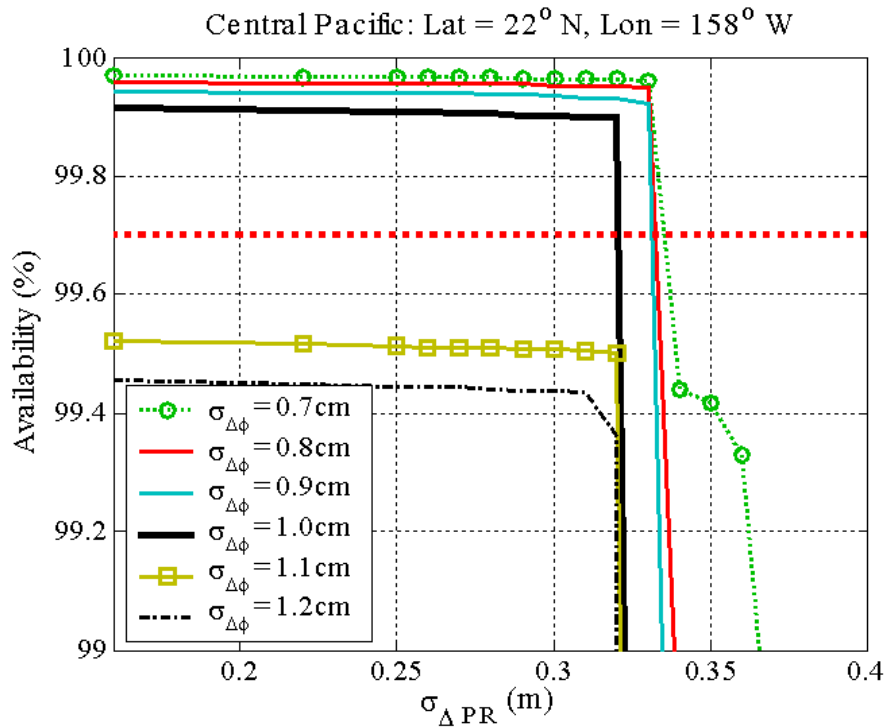


Figure 6.5. Availability of Double Difference Widelane $\psi = 40$

For a given value of ψ , each figure shows the required single difference standard deviation of code ($\sigma_{\Delta PR}$) and carrier ($\sigma_{\Delta\phi}$) phase measurements to ensure 99.7% availability. From the results, it is clear that as ψ increases the required $\sigma_{\Delta PR}$ also increases. It is also evident that the required $\sigma_{\Delta PR}$ is much more sensitive than $\sigma_{\Delta\phi}$ to variations in ψ . For example, as ψ varies from 20 to 40, the required $\sigma_{\Delta PR}$ is relaxed from 22 cm up to 32 cm. In contrast, the required maximum $\sigma_{\Delta\phi}$ remains 1 cm, for all values of ψ .

6.4 Double Difference Widelane Landing with Geometric Redundancy

The use of geometric redundancy provides two significant improvements to the simple processing structure described above:

1. Increased availability
2. Relaxation of the required $\sigma_{\Delta\phi}$ and $\sigma_{\Delta PR}$.

However, the use of geometric redundancy introduces spatial decorrelation error into cycle ambiguity estimation. Therefore, it should be used only if the displacement between the aircraft and ship is small (0.25 nmi in this work).

A correct fix of those widelane cycle ambiguities not fixed using geometry-free filtering, or some subset linear combination of these, will improve positioning performance [Pervan01]. Obviously, for any implementation of geometric redundancy it is desired that the probability of incorrect fix be small. In this work, Teunissen's 'Integer Bootstrapping' algorithm with LAMBDA cycle ambiguity decorrelation is used as the fixed integer implementation model [Teunissen98]. The Integer Bootstrapping implementation is a successive rounding approach that has two significant benefits for our application:

1. The probability of correct fix can be computed directly.
2. Fixing can be restricted to only those cycle ambiguities (or linear combinations thereof) which have high probability of correct fix.

For this application, it was determined whether for some (or all) linear combinations of cycle ambiguities the probability of correct fix is larger than $1-10^{-8}$. If so, the position error covariance was updated assuming the associated integers were precisely known. For the remaining cycle ambiguities, the floating estimates (and variances) were retained.

The availability of the double difference widelane architecture using geometric redundancy was evaluated for various values of $\sigma_{\Delta\phi}$ and $\sigma_{\Delta PR}$. The sensitivity of availability to non-dimensional time, ψ , is shown in Figures 6.6 to 6.8 (for the same ship location and elevation mask used in the last section). When compared to the previous results (which used the double difference widelane without geometric redundancy) for any given value of ψ , the new results show that the required $\sigma_{\Delta PR}$ is relaxed

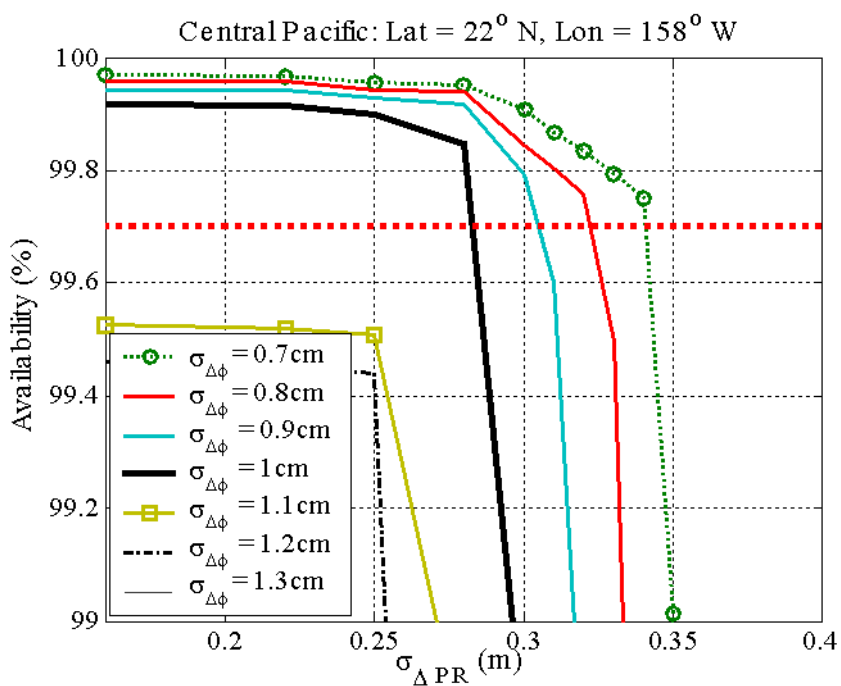


Figure 6.6. Availability of Double Difference Widelane using Geometric Redundancy
 $\psi = 20$

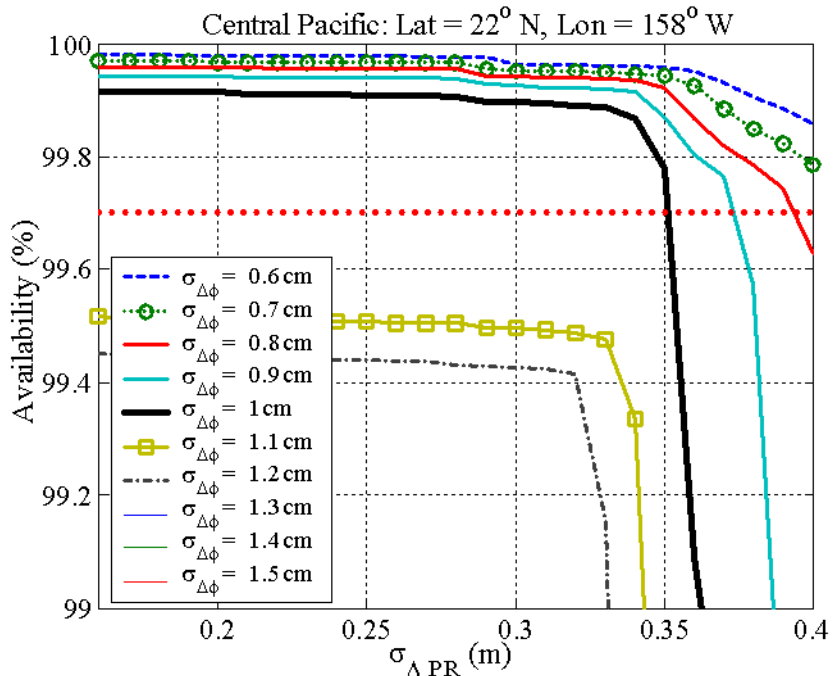


Figure 6.7. Availability of Double Difference Widelane using Geometric Redundancy $\psi = 30$

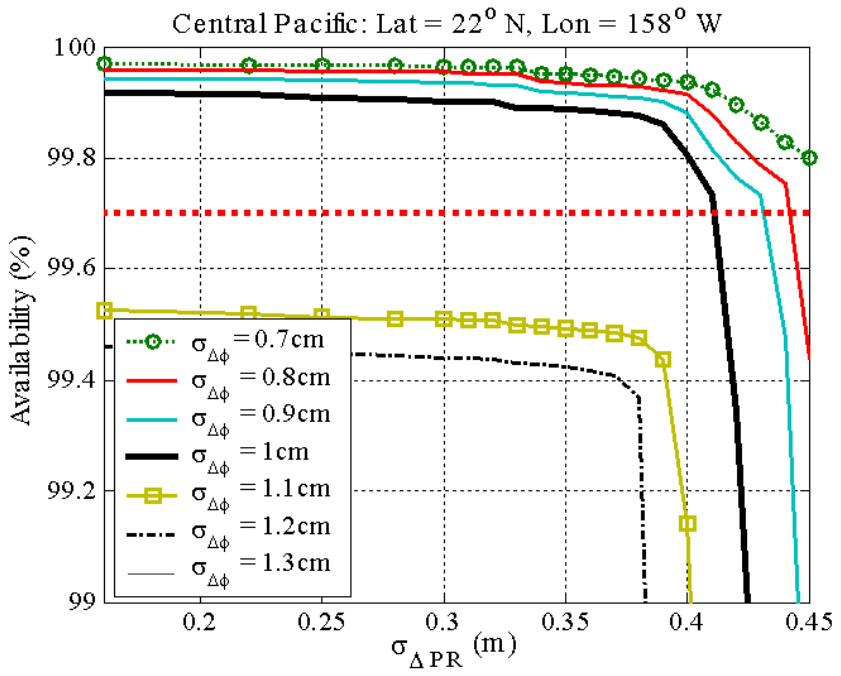


Figure 6.8. Availability of Double Difference Widelane using Geometric Redundancy $\psi = 40$

significantly. As an example, given $\sigma_{\Delta\phi} = 1$ cm and $\psi = 30$, the required $\sigma_{\Delta PR}$ is 35 cm or less with geometric redundancy and 28 cm or less without. However, it is also evident in the comparison between the results in Figures 6.3 to 6.5 and 6.6 to 6.8 that the required $\sigma_{\Delta\phi}$ does not deviate from 1 cm. This is due to the fact that a single difference standard deviation of 1 cm is necessary to ensure widelane carrier phase positioning availability even if all cycle ambiguities are correctly fixed. It is natural then to consider the potential benefits of processing L1 and L2 measurements directly (rather than using widelane measurements) when the aircraft is close to the ship. This approach is explored in the next section.

6.5 Double Difference L1/L2 Landing with Geometric Redundancy

The double difference measurement Equations (6.15) and (6.16) in cycles can be written as

$$\begin{bmatrix} \nabla\Delta\phi_{L1} \\ \nabla\Delta\phi_{L2} \end{bmatrix} = H \begin{bmatrix} x_{3 \times 1} / \lambda_{L1} \\ \nabla\Delta N_{L1, (n-1) \times (n-1)} \\ \nabla\Delta N_{L2, (n-1) \times (n-1)} \end{bmatrix} + v_{\nabla\Delta} \quad (6.22)$$

where $\nabla\Delta N_{L1, (n-1) \times (n-1)}$ is the $(n-1) \times (n-1)$ double difference integer for the L1 carrier measurements, $\nabla\Delta N_{L2, (n-1) \times (n-1)}$ is the $(n-1) \times (n-1)$ double difference integer for the L2 carrier measurements, and $v_{\nabla\Delta}$ is the double difference measurement noise in cycles. The position states in Equation (6.22) are expressed in L1 cycles. The observation matrix H is

$$H = \begin{bmatrix} G_{(n-1) \times 3} & I_{(n-1) \times (n-1)} & 0_{(n-1) \times (n-1)} \\ G_{(n-1) \times 3} \times \lambda_{L1} / \lambda_{L2} & 0_{(n-1) \times (n-1)} & I_{(n-1) \times (n-1)} \end{bmatrix} \quad (6.23)$$

where $G_{(n-1) \times 3}$ is the double difference geometry matrix which was defined below Equation (6.18). To fuse the prefiltering information (the double difference widelane cycle ambiguity estimate vector and covariance matrix) into Equation (6.22), we need to express the double difference widelane integer observable in terms of the double difference L1 and L2 carrier phase integers. In this case, the appropriate mathematical expression is

$$\begin{bmatrix} \nabla \Delta \hat{N}_w^{1j} \\ \vdots \\ \nabla \Delta \hat{N}_w^{1j} \end{bmatrix} = H' \begin{bmatrix} \nabla \Delta N_{L1}^{12} \\ \vdots \\ \nabla \Delta N_{L1}^{1n} \\ \nabla \Delta N_{L2}^{12} \\ \vdots \\ \nabla \Delta N_{L2}^{1n} \end{bmatrix} + v_N \quad (6.24)$$

where $\nabla \Delta N_{L1}^{1n}$ is the true double difference L1 integer, $\nabla \Delta N_{L2}^{1n}$ is the true double difference L2 integer, and v_N is the widelane cycle ambiguity estimate error from pre-filtering, which has covariance matrix $P_{\nabla \Delta N, w}$. H' is simply the coefficient matrix which defines the relationship between the double difference widelane carrier and double difference L1/L2 carrier integers. Its mathematical expression is

$$H' = \begin{bmatrix} I_{(n-1) \times (n-1)} & -I_{(n-1) \times (n-1)} \end{bmatrix}. \quad (6.25)$$

Given Equation (6.21), the covariance matrix of double difference L1/L2 carrier phase integers was extracted from the covariance matrix from the pre-filtering process. Then the cycle ambiguity states (Equation (6.22)) were refined (fixed) using geometric redundancy, as described in the previous section for widelane ambiguities. The aircraft vertical position error covariance was computed and compared to the VAL.

The simulation results, using the same ship location, elevation mask, and measurement error parameters as those in Figures 6.3 to 6.8, are shown in Figures 6.9 to 6.11. In comparison with the results on the prior figures, Figures 6.9 to 6.11 show that L1/L2 processing provides further performance improvement. Specifically, it is evident that for any given time ratio ψ , L1/L2 processing enables relaxation of the required

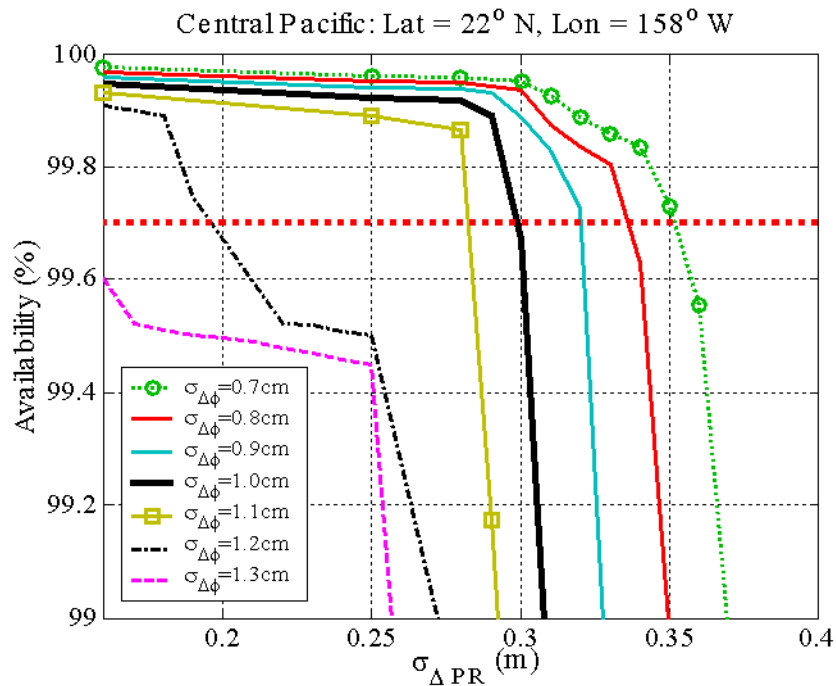


Figure 6.9. Availability of Double Difference L1/L2 Carrier Phase using Geometric Redundancy $\psi = 20$

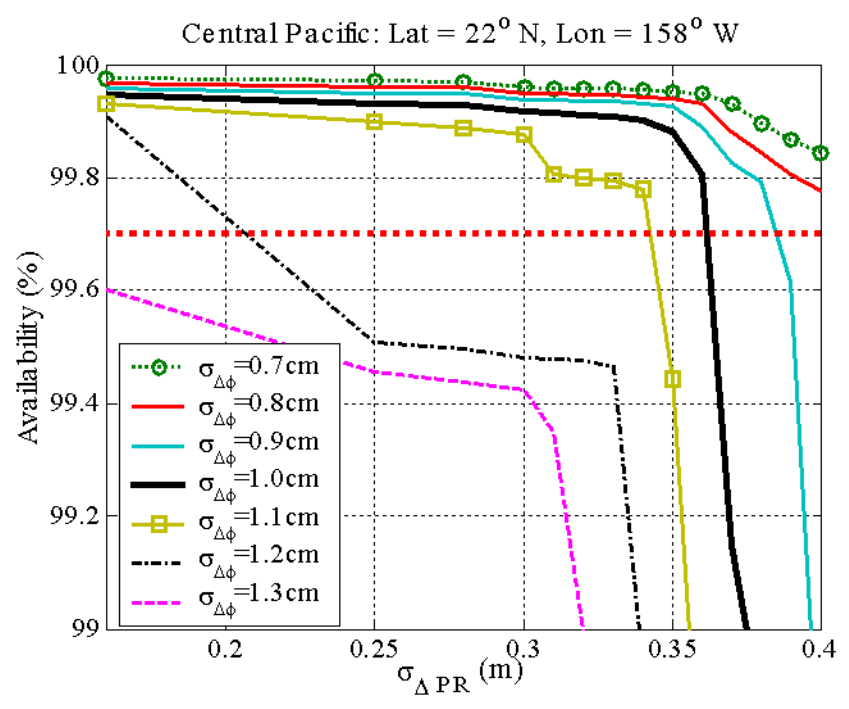


Figure 6.10. Availability of Double Difference L1/L2 Carrier Phase using Geometric Redundancy $\psi = 30$

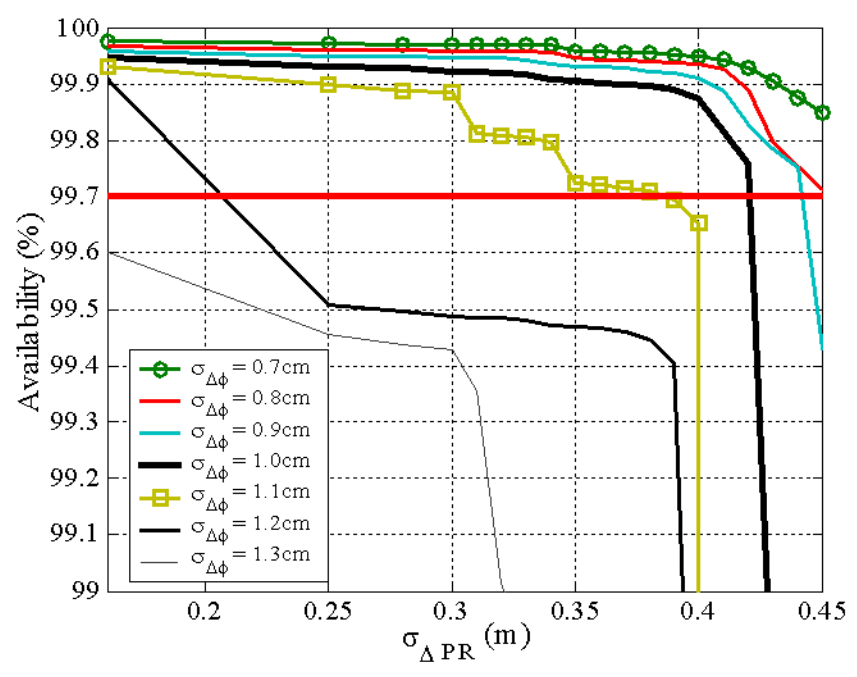


Figure 6.11. Availability of Double Difference L1/L2 Carrier Phase using Geometric Redundancy $\psi = 40$

values of both $\sigma_{\Delta PR}$ and $\sigma_{\Delta\phi}$. The effect on the required $\sigma_{\Delta\phi}$ is especially notable, since it was invariant in the previous results and showed significant performance degradation below 1 cm. While the relaxation in $\sigma_{\Delta\phi}$ is modest here, it is important to observe that performance degrades more gracefully as $\sigma_{\Delta\phi}$ increases. In contrast, the performance of both widelane architectures is severely affected when $\sigma_{\Delta\phi}$ is larger than 1 cm.

Figures 6.12 to 6.14 quantify the sensitivity of availability of L1/L2 processing to ship location. The availability results were computed for three different ship locations—near China (latitude = 20 deg N, longitude = 120 deg E), Atlantic Ocean (latitude = 25 deg N, longitude = -30 deg E) and Pacific Ocean (latitude = 35 deg N, longitude = -158

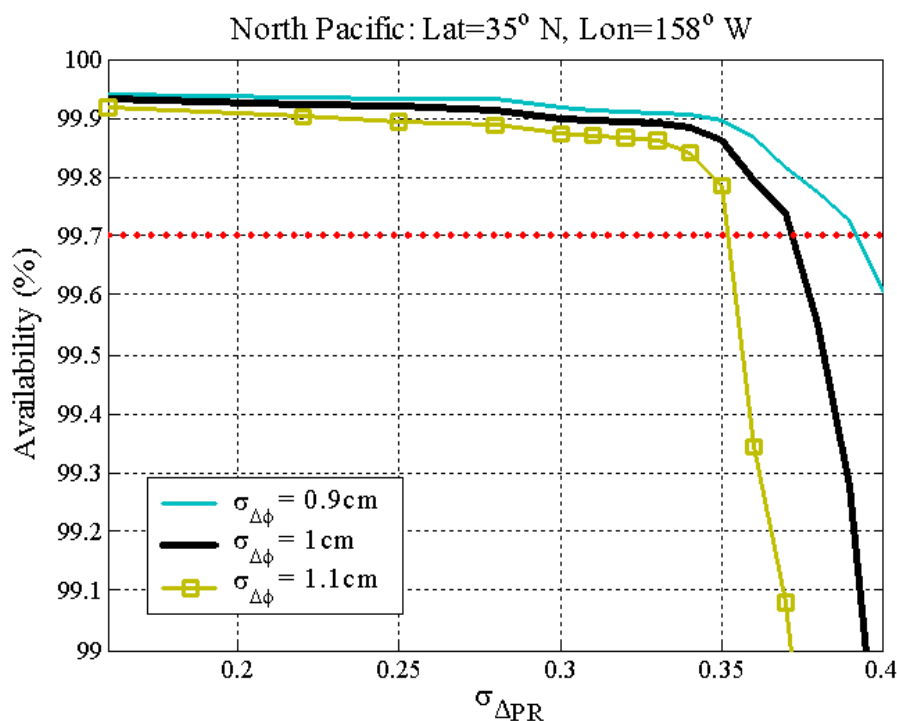


Figure 6.12. Availability of Double Difference L1/L2 Carrier Phase using Geometric Redundancy at the Pacific Ocean with $\psi = 30$

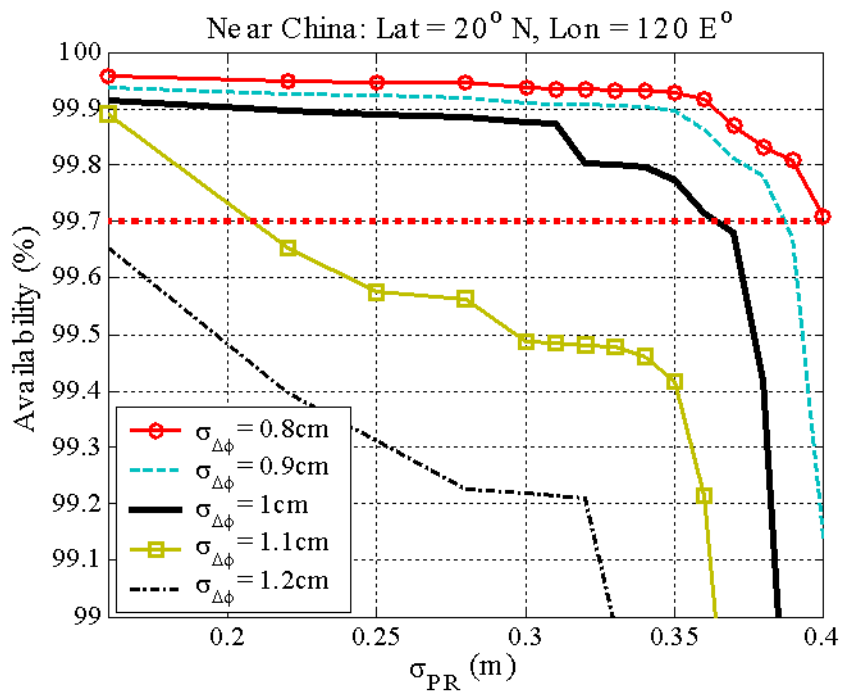


Figure 6.13. Availability of Double Difference L1/L2 Carrier Phase using Geometric Redundancy Near China with $\psi = 30$

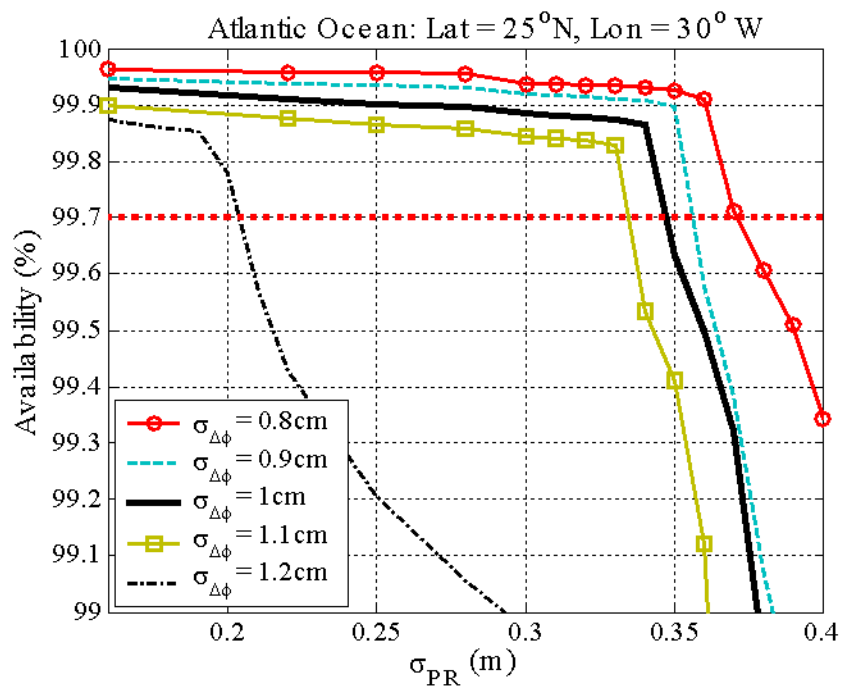


Figure 6.14. Availability of Double Difference L1/L2 Carrier Phase using Geometric Redundancy at the Atlantic Ocean with $\psi = 30$

deg E). The simulation results use the same elevation mask, and measurement error parameters as those in Figure 6.3 to 6.14 (considering only the time ratio $\psi=30$). The figures show that the required single difference code measurement errors associated with SRGPS availability, $\sigma_{\Delta\phi} = 1$ cm, are between 34.5-37 cm. Based on the result, the availability is moderately sensitive to ship locations.

6.6 Experimental Results

In April 2001, the JPALS test team successfully performed the first global positioning system (GPS)-based automatic landing to an aircraft carrier aboard the USS THEODORE ROOSEVELT (Carrier Vessel Nuclear (CVN)-71) [Waters01]. A total of 19 flights and 23.1 flight hours were flown over a three month period. The test results provided L1/L2 code and carrier phase range measurements for ship and aircraft, along with navigation information.

The geometry-free prefiltering algorithm was tested in post-processing of the flight test data. For the process, we needed a set of data (L1/L2 code and carrier for the ship and aircraft) for prefiltering. The selection was based on data requiring at least 30 minutes or longer for validation. PRN 2 was one of the valid data sets. The estimated widelane integer of PRN 2 dramatically converged over about 33 minutes as shown in Figure 6.15. Due to the large magnitude of the cycle ambiguity integer, the bias (the integer) has been removed for clarity in the plot. Based on the result, the performance of prefiltering is efficient.

6.7 Summary of Robust Navigation Algorithm

Figure 6.16 summarizes three proposed processing methodologies, which were defined to robustly combine the complementary benefits of geometry-free filtering and geometric redundancy. Route 1 is the double difference widelane positioning, Route 2 is the double difference widelane positioning with geometric redundancy, and Route 3 is the double difference L1/L2 positioning with geometric redundancy. The performance of the algorithms was expressed in terms of the required code measurement error associated with SRGPS required availability for various parameters. The results show that the best performance for SRGPS is achieved using the third method. However, in the third method, the ship has to broadcast more data (L1 and L2 raw carrier phase measurements) to the aircraft than in the first and second methods.

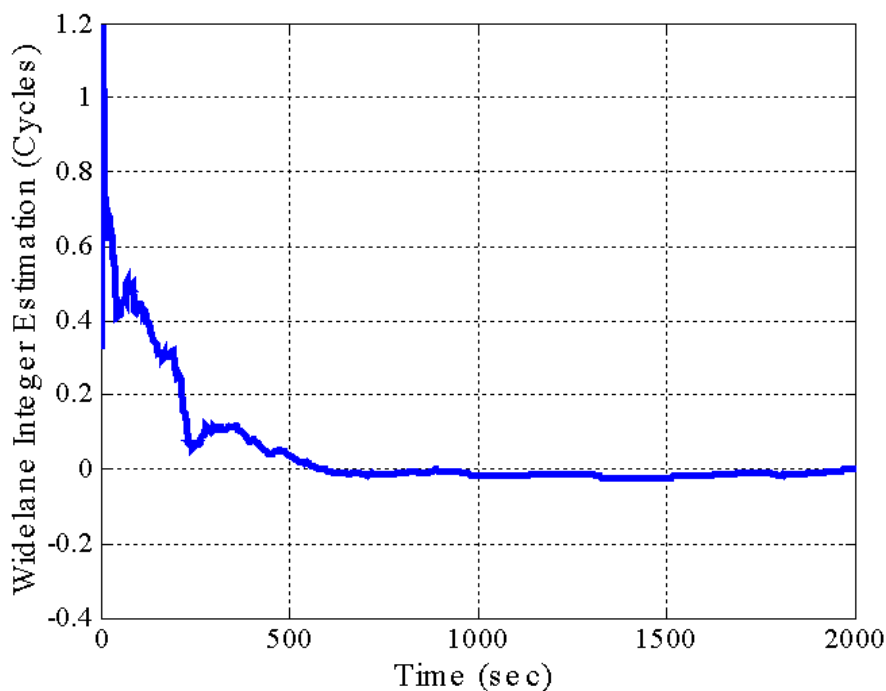


Figure 6.15. Widelane Integer Estiamtion

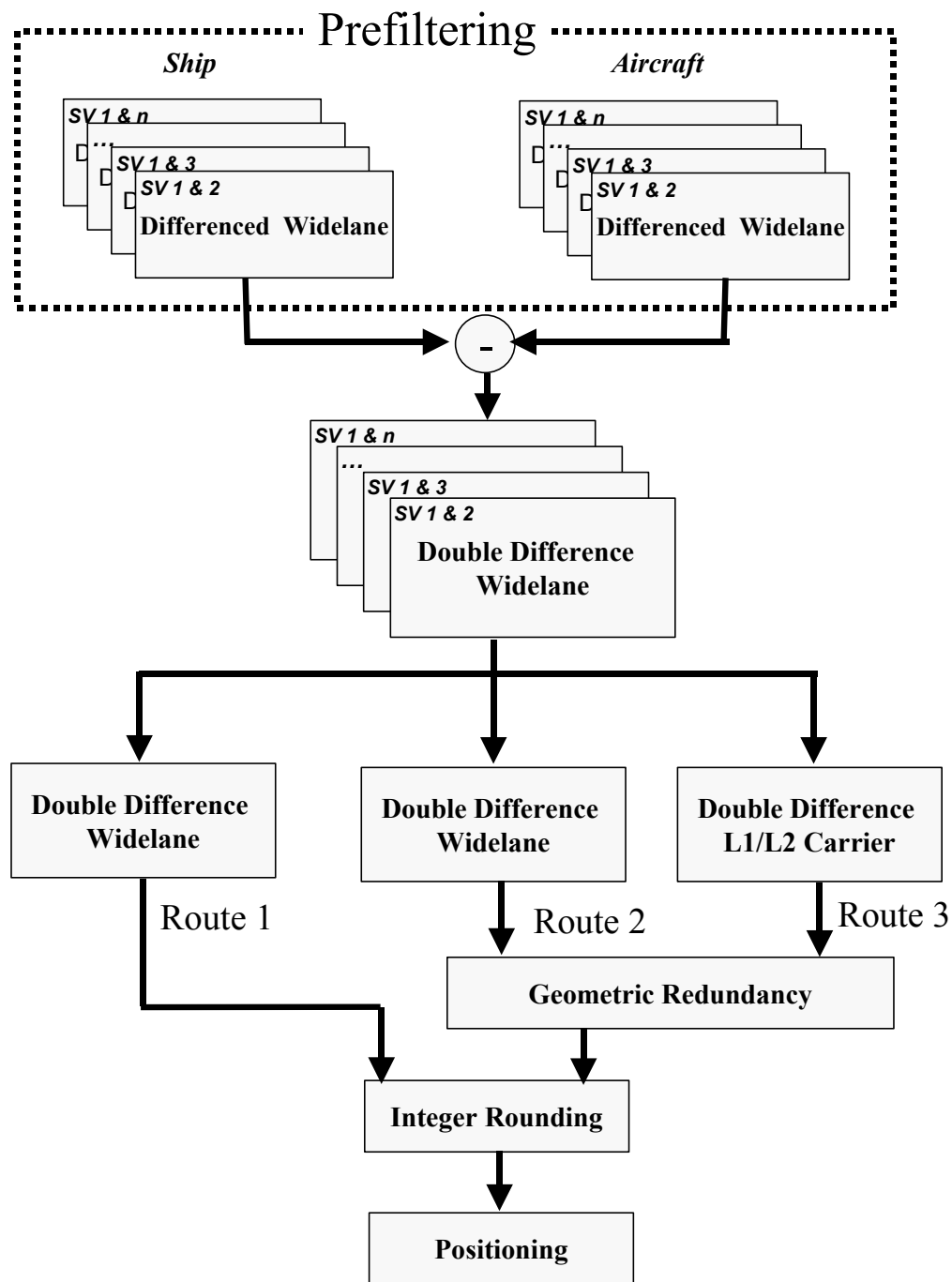


Figure 6.16. Geometry-Free Prefiltering Algorithm Diagram

CHAPTER 7

CONCLUSIONS

Shipboard-Relative GPS (SRGPS) is an architectural variant of JPALS that will provide high accuracy and high integrity DGPS navigation for automatic shipboard landings. Unlike similar operations at ground-based airports, shipboard landing calls for higher navigation performance because of the mobility of the landing platform. In this dissertation, design of a GPS-based aircraft navigation system that meets the stringent SRGPS requirements has been addressed.

7.1 Autonomous Fault Detection

This dissertation has addressed the design of SRGPS airborne integrity monitor algorithms to detect and isolate navigation threats that are otherwise undetectable by integrity monitors at the shipboard differential reference station. Three specific navigation integrity threats were addressed in this work: airborne receiver cycle slips, orbit ephemeris anomalies, and ionospheric gradient anomalies.

7.1.1 Cycle Slip Detection. A RAIM-based cycle slip detection algorithm was developed and evaluated using integer and half-integer constraints on failure magnitude. Based on the results, it was determined that while RAIM can be effective for specific cycle slip threat models, the availability of the RAIM function is insufficient to protect against all classes of cycle slip threats.

7.1.2 Ephemeris Error Detection. A relative RAIM-based autonomous orbit ephemeris fault detection algorithm was also developed, evaluated, and shown to be sufficient to provide protection against ephemeris threats. Necessary conditions for operational distance requirements were specifically defined to ensure availability of the fault detection function.

7.1.3 Ionospheric Error Detection. Finally, autonomous ionospheric gradient detection algorithms were designed using direct observation methods. Necessary conditions to ensure fault detection availability for both dual and single frequency implementations were defined.

7.2 Robust Navigation Algorithm

The design of robust airborne algorithms for SRGPS terminal navigation was discussed. In this context, three processing methodologies were defined to robustly combine the complementary benefits of geometry-free filtering and geometric redundancy. These algorithms were:

1. geometry-free pre-filtering and near-ship positioning using the widelane observable exclusively,
2. geometry-free pre-filtering with near-ship geometric redundancy and positioning using the widelane observable exclusively, and
3. geometry-free widelane pre-filtering and L1/L2 near-ship geometric redundancy and positioning.

The results show that the best performance for SRGPS is achieved using the third method, though the ship must broadcast more data (L1 and L2 raw measurements) to the aircraft in this method than in the first and second methods (widelane measurements only). Based on the results, the navigation performance is observed to be moderately sensitive to ship locations. In addition, the sensitivity of navigation performance to the standard deviations of raw carrier and code phase measurements, the code measurement error time constant, and the filtering time was quantified. Necessary conditions on these parameters to ensure SRGPS availability were specifically defined.

7.3 Recommendations and Future Work

1. Cycle Slips: Because the RAIM function is insufficient to protect against all classes of cycle slip threats, it is recommended that the RAIM-based cycle slip detection function be augmented in future work with the integration of INS measurements.
2. Ionospheric Error Detection: In 2000, a severe ionospheric storm was observed by WAAS. This ionospheric storm is exhibited abrupt changes in ionospheric delay. In this context, the detection of such abrupt ionospheric wave fronts must be addressed in future work.
3. Robust Navigation Algorithm: Based on the results in this dissertation, the performance of the prefiltering algorithm is known to be sensitive to the nondimensional ratio ψ (prefiltering time/multipath time constant). Therefore, the robustness of algorithm performance to the multipath time constant must be carefully investigated.

4. When new flight data is available, the proposed algorithms in this dissertation should be tested in post-processing of that flight-test data (F-18 aircraft carrier landing) by deliberate injection of failure into raw measurements.

APPENDIX A
BASIC RAIM CONCEPTS

Consider the generalized linear observation equation

$$z = (H - \delta H)x + v \quad (\text{A.1})$$

where H is the observation matrix, z is the measurement vector, x is the vector to be estimated, and v and δH are the unknown errors in the measurement vector and observation matrix.

The least squares solution to Equation (A.1) is

$$\hat{x} = H^+ z \quad (\text{A.2})$$

where \hat{x} is the estimated vector, and $H^+ \equiv (H^T H)^{-1} H^T$. The corresponding least squares estimate error under normal conditions is defined as

$$\delta x \equiv \hat{x} - x \quad (\text{A.3})$$

The least square residual vector, r , is a measure of the consistency of the measurement vector, z , subject to the observation matrix, H , and is expressed simply as

$$r \equiv z - H\hat{x} \quad (\text{A.4})$$

Combining Equations (A.1), (A.2), and (A.4), the residual vector can be expressed in terms of the measurement and observation matrix errors,

$$r = (I - HH^+)(\delta z - \delta Hx) \quad (\text{A.5})$$

where under normal error conditions

$$\delta H \cong 0 \text{ and } \nu \sim N(0, \sigma_z^2 I_n). \quad (\text{A.6})$$

For the case of correlated measurement error with covariance matrix, W , relations equivalent to (A.5) can be obtained if both sides of Equation (A.1) are multiplied by a ‘weighting matrix,’ $W^{-\frac{1}{2}}$ [Walter95]. The details will be explained in Appendix F.

APPENDIX B
COMPUTATION OF MISSED DETECTION PROBABILITY

Consider a failure of magnitude b on channel i . The vertical position error i can then be expressed as

$$\delta x = H_{3,i}^+ b + H_{3,i}^+ v \quad (\text{B.1})$$

where $H_{3,i}^+$ is the third row of the pseudo-inverse (i.e., the row corresponding to the vertical position state) of the observation matrix, H .

Using Equation (B.1), the probability that the position error is larger than the VAL can be expressed mathematically as

$$\text{P}(|\delta x_3| > VAL | b) = \text{P}(H_{3,i}^+ v > VAL - H_{3,i}^+ b) + \text{P}(H_{3,i}^+ v < -VAL - H_{3,i}^+ b) \quad (\text{B.2})$$

where the terms on the right-hand side of Equation (B.2) represent the tail probabilities of a normal distribution.

Because the $n \times 1$ vector, r , is orthogonal to the columns of the $n \times 4$ observation matrix, H , the elements of r are not all independent. Therefore, it is enough to consider the $(n - 4)$ -space orthogonal to the columns of H . This is called parity space, and details of the parity space method are explained in [Pervan98, Sturza88].

Given a bias failure of magnitude b on channel i , the $(n - 4) \times 1$ parity vector p can be expressed as

$$p \sim N(C_{:,i} b, \sigma_v^2 I_{n-m}) \quad (\text{B.3})$$

where C is the left null space of H . It is shown in [Lee95] that

$$\mathbb{P}(\|r\| < T \mid b) \cong \mathbb{P}(\nu > \|C_{:,i}\|_2 b - T) \quad (\text{B.4})$$

where $\mathbb{P}(\nu > \|C_{:,i}\|_2 b - T)$ represents the tail probability of a normal distribution.

Finally, the joint probability of missed detection given a failure b can be expressed simply as,

$$\begin{aligned} \mathbb{P}(MD \mid b) &= \mathbb{P}(\delta x_3 > VAL, \|r\| < T \mid b) \\ &= \left[\mathbb{P}(H_{3,i}^+ \nu > VAL - H_{3,i}^+ b) + \mathbb{P}(H_{3,i}^+ \nu > -VAL - H_{3,i}^+ b) \right] \mathbb{P}(\nu > \|C_{:,i}\|_2 b - T). \end{aligned} \quad (\text{B.5})$$

where ν is distributed as in Equation (A.6).

APPENDIX C**RANGE MEASUREMENT ERROR DUE TO IONOSPHERIC GRADIENT**

The observation equation for carrier positioning can be expressed as

$$\phi(x) = e^T x + N - I(x) \quad (\text{C.1})$$

Given an estimate of the cycle ambiguity,

$$\hat{N} = N + \delta N, \quad (\text{C.2})$$

the adjusted carrier phase observable is

$$\phi(x) - \hat{N} = e^T x + \delta\phi(x), \quad (\text{C.3})$$

where

$$\delta\phi(x) = -\delta N - I(x), \quad (\text{C.4})$$

δN is the error in the cycle ambiguity, and nominal carrier phase measurement errors are neglected for the moment.

Let us assume that the cycle is resolved at distance x_1 . The limit case effective cycle ambiguity errors are:

1. Limit Case 1: $\delta N = \delta\phi - \delta\rho = -2I(x_1)$
 2. Limit Case 2: $\delta N = -I(x_1)$
- (C.5)

where $I(x_1)$ is the differential ionospheric delay at the distance of x_1 . When expressed in terms of the differential ionospheric gradient k , we have

$$I(x_1) = kx_1. \quad (\text{C.6})$$

Finally, substituting Equations (C.4) and (C.5) into Equation (C.6), the limit case effective range measurement errors due to the ionospheric gradient in Table 5.1 can be computed.

APPENDIX D
VARIANCE ESTIMATE

Suppose that $x(t)$ is the stationary random process and exists over a finite time T . The mean of $x(t)$ can be estimated by averaging over the interval T . The variance of the estimate error can be expressed as [Bendat00]:

$$\text{var} = \frac{1}{T} \int_{-T}^T \left[1 - \frac{|\tau|}{T} \right] C_{xx}(\tau) d\tau \quad (\text{D.1})$$

where $C_{xx}(\tau)$ is the autocovariance function of $x(t)$. The mathematic expression of $C_{xx}(\tau)$ is

$$C_{xx}(\tau) = R_{xx}(\tau) - \mu_x^2 \quad (\text{D.2})$$

where $R_{xx}(\tau)$ is the autocorrelation function of the random process and μ_x is the mean value of the random process.

In this work, the code phase error was modeled as a first-order Gauss-Markov random process, and its autocovariance function is

$$C_{xx}(\tau) = \sigma^2 e^{-\beta|\tau|} \quad (\text{D.3})$$

where σ is the standard deviation of measurement error and $1/\beta$ is the correlation time.

Substituting (D.3) into (D.1)

$$\text{var} = \frac{1}{T} \int_{-T}^T \left[1 - \frac{|\tau|}{T} \right] \sigma^2 e^{-\beta|\tau|} d\tau = \frac{2\sigma^2}{T\beta} - \frac{2\sigma^2}{T^2\beta^2} (1 - e^{-T\beta}) . \quad (\text{D.4})$$

APPENDIX E
WIDELANE IONOSPHERIC FREE ESTIMATION

The widelane carrier phase observable can be directly obtained by subtracting Equation (6.3) from (6.1)

$$\Delta\phi_{L1} - \Delta\phi_{L2} = \rho \left(\frac{1}{\lambda_{L1}} - \frac{1}{\lambda_{L2}} \right) + \Delta I \left(-\frac{1}{\lambda_{L1}} + \beta \frac{1}{\lambda_{L2}} \right) + (N_{L1} - N_{L2}) + \left(\frac{\varepsilon_{\Delta\phi,L1}}{\lambda_{L1}} - \frac{\varepsilon_{\Delta\phi,L2}}{\lambda_{L2}} \right) \quad (\text{E.1})$$

where $\Delta\phi_{L1}$ is the differenced L1 carrier phase measurement and $\varepsilon_{\Delta\phi} \sim N(0, \sigma_{\Delta\phi}^2)$.

Given differenced code measurement Equations (6.2) and (6.4), adding between L1 and L2 measurements produces a new signal with shorter wavelength. It is called ‘narrow lane.’ The mathematical expression is

$$\frac{\Delta PR_{L1}}{\lambda_{L1}} + \frac{\Delta PR_{L2}}{\lambda_{L2}} = \rho \left(\frac{1}{\lambda_{L1}} + \frac{1}{\lambda_{L2}} \right) + \Delta I \left(\frac{1}{\lambda_{L1}} + \frac{1}{\lambda_{L2}} \right) + \left(\frac{\varepsilon_{\Delta PR,L1}}{\lambda_{L1}} + \frac{\varepsilon_{\Delta PR,L2}}{\lambda_{L2}} \right) \quad (\text{E.2})$$

where ΔPR_{L1} is the differenced L1 code phase measurement and $\varepsilon_{\Delta PR} \sim N(0, \sigma_{\Delta PR}^2)$.

Equations (E.1) and (E.2) can be rearranged to obtain

$$\Delta\phi_{L1} - \Delta\phi_{L2} = \rho \left(\frac{\lambda_{L2} - \lambda_{L1}}{\lambda_{L1}\lambda_{L2}} \right) + \Delta I \left(\frac{\lambda_{L2} - \lambda_{L1}}{\lambda_{L1}^2} \right) + (N_{L1} - N_{L2}) + \left(\frac{\varepsilon_{\Delta\phi,L1}}{\lambda_{L1}} - \frac{\varepsilon_{\Delta\phi,L2}}{\lambda_{L1}} \right), \quad (\text{E.3})$$

and

$$\begin{aligned} & \left(\frac{\lambda_{L2} - \lambda_{L1}}{\lambda_{L1} + \lambda_{L2}} \right) \left(\frac{\Delta PR_{L1}}{\lambda_{L1}} + \frac{\Delta PR_{L2}}{\lambda_{L2}} \right) \\ & = \rho \left(\frac{\lambda_{L2} - \lambda_{L1}}{\lambda_{L1} \lambda_{L2}} \right) + \Delta I \left(\frac{\lambda_{L2} - \lambda_{L1}}{\lambda_{L1}^2} \right) + \left(\frac{\lambda_{L2} - \lambda_{L1}}{\lambda_{L1} + \lambda_{L2}} \right) \left(\frac{\mathcal{E}_{\Delta PR, L1}}{\lambda_{L1}} + \frac{\mathcal{E}_{\Delta PR, L2}}{\lambda_{L2}} \right) \end{aligned} \quad (E.4)$$

Differencing eliminates the ionospheric terms between the widelane carrier phase Equation (E.3) and the narrowlane Equation (E.4)

$$\begin{aligned} & (\Delta \phi_{L1} - \Delta \phi_{L2}) - \left(\frac{\lambda_{L2} - \lambda_{L1}}{\lambda_{L1} + \lambda_{L2}} \right) \left(\frac{\Delta PR_{L1}}{\lambda_{L1}} + \frac{\Delta PR_{L2}}{\lambda_{L2}} \right) \\ & = (N_{L1} - N_{L2}) + \left(\frac{\mathcal{E}_{\Delta \phi, L1}}{\lambda_{L1}} - \frac{\mathcal{E}_{\Delta \phi, L2}}{\lambda_{L2}} \right) - \left(\frac{\lambda_{L2} - \lambda_{L1}}{\lambda_{L1} + \lambda_{L2}} \right) \left(\frac{\mathcal{E}_{\Delta PR, L1}}{\lambda_{L1}} + \frac{\mathcal{E}_{\Delta PR, L2}}{\lambda_{L2}} \right) \end{aligned} \quad (E.5)$$

The right hand side of Equation (E.5) contains the widelane integers. Consequently, Equation (E.5) can be simplified as

$$Z_w = N_w + \nu_w \quad (E.6)$$

where

$$Z_w = (\Delta \phi_{L1} - \Delta \phi_{L2}) - \left(\frac{\lambda_{L2} - \lambda_{L1}}{\lambda_{L1} + \lambda_{L2}} \right) \left(\frac{\Delta PR_{L1}}{\lambda_{L1}} + \frac{\Delta PR_{L2}}{\lambda_{L2}} \right),$$

$$N_w = (N_{L1} - N_{L2}), \text{ and}$$

$$\nu_w = \left(\frac{\mathcal{E}_{\Delta \phi, L1}}{\lambda_{L1}} + \frac{\mathcal{E}_{\Delta \phi, L2}}{\lambda_{L2}} \right) - \left(\frac{\lambda_{L2} - \lambda_{L1}}{\lambda_{L1} + \lambda_{L2}} \right) \left(\frac{\mathcal{E}_{\Delta PR, L1}}{\lambda_{L1}} + \frac{\mathcal{E}_{\Delta PR, L2}}{\lambda_{L2}} \right).$$

Recalling that $\sigma_{\Delta\phi,L1}^{ij} = \sigma_{\Delta\phi,L2}^{ij} \equiv \sigma_{\Delta\phi}$ and $\sigma_{\Delta PR,L1}^{ij} = \sigma_{\Delta PR,L2}^{ij} \equiv \sigma_{\Delta PR}$, the variance of the differential widelane cycle ambiguity estimate error for a single measurement sample of (E.6) is

$$\sigma_w^2 = \left(\frac{1}{\lambda_{L1}^2} + \frac{1}{\lambda_{L2}^2} \right) \left(\sigma_{\Delta\phi}^2 + \left(\frac{\lambda_{L2} - \lambda_{L1}}{\lambda_{L1} + \lambda_{L2}} \right)^2 \sigma_{\Delta PR}^2 \right). \quad (\text{E.7})$$

Equation (E.7) yields precisely the same numerical results as the state vector approach described in Chapter 6.

APPENDIX F
WEIGHTED RAIM

If the measurements error is correlated, the weighted least squares estimate of x in Equation (A.1) is given as follows:

$$\hat{x} = (H^T W H)^{-1} H^T W z \quad (\text{F.1})$$

where

$$W^{-1} = \begin{bmatrix} \sigma_1^2 & & 0 \\ & \ddots & \\ 0 & & \sigma_n^2 \end{bmatrix}. \quad (\text{F.2})$$

For weighted RAIM, Equation (A.1) can be normalized by pre-multiplying by $W^{-\frac{1}{2}}$ [Walter95]:

$$W^{-\frac{1}{2}} z = W^{-\frac{1}{2}} H x + W^{-\frac{1}{2}} v. \quad (\text{F.3})$$

Normalized measurement Equation (F.3) can be simplified as

$$Z' = H' x + v' \quad (\text{F.4})$$

where $Z' = W^{-\frac{1}{2}} z$, $H' = W^{-\frac{1}{2}} H$, and $v' = W^{-\frac{1}{2}} v$. The weighted RAIM function can be expressed using Equation (F.4)

$$\begin{aligned}
 r &= Z' - H' \hat{x} \\
 &= W^{-\frac{1}{2}} z - W^{-\frac{1}{2}} H \hat{x} = W^{-\frac{1}{2}} (I - HH^{w+}) z
 \end{aligned}
 \tag{F.5}$$

where $H^{w+} = (H^T W H)^{-1} H^T W$.

Finally the norm of the residual vector is obtained simply as

$$\|r\|^2 = z^T (I - HH^{w+}) W (I - HH^{w+}) z.
 \tag{F.6}$$

APPENDIX G
AVAILABILITY OF EPHEMERIS ERROR DETECTION FOR DIFFERENT
SHIP LOCATIONS

The availability of ephemeris error detection has been evaluated for the various ship locations—latitude = 20 deg N, longitude = 60 deg -E, latitude = 5 deg N, longitude = -135 deg E and latitude = 10 deg N, longitude = -30deg E. The satellite outage state probability model in Table 3.1, a single difference measurement error standard deviation of 1 cm, and a required missed detection probability of 10^{-4} were assumed in this analysis.

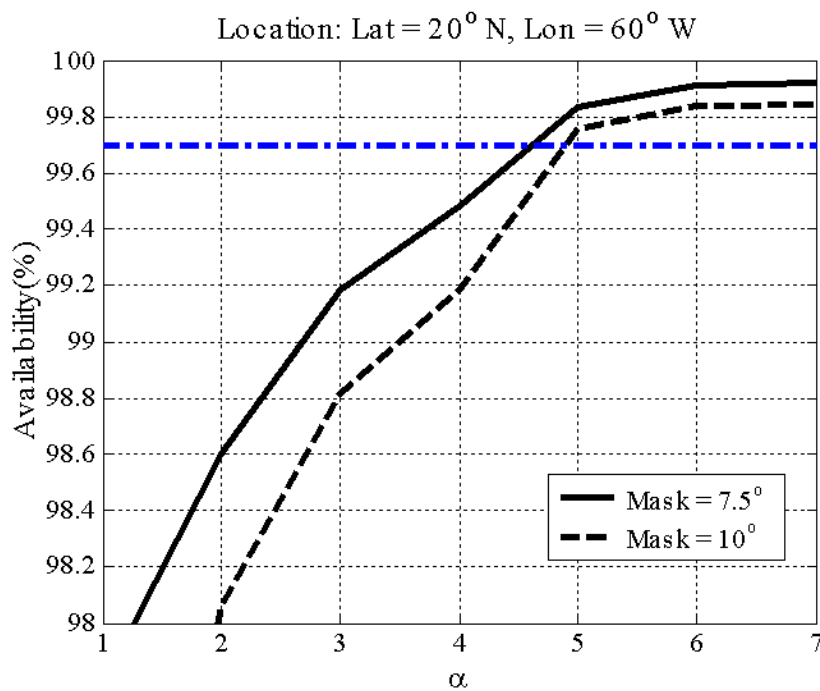


Figure G.1. Availability of Ephemeris Error Detection at Lat = 20° N and Lon = 60° W

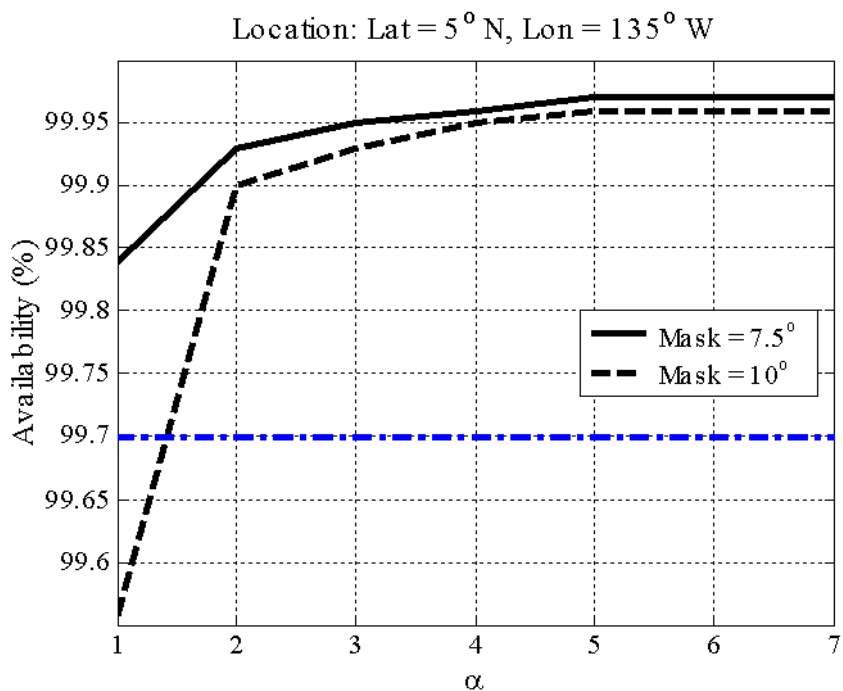


Figure G.2. Availability of Ephemeris Error Detection at Lat = 5° N and Lon = 135° W

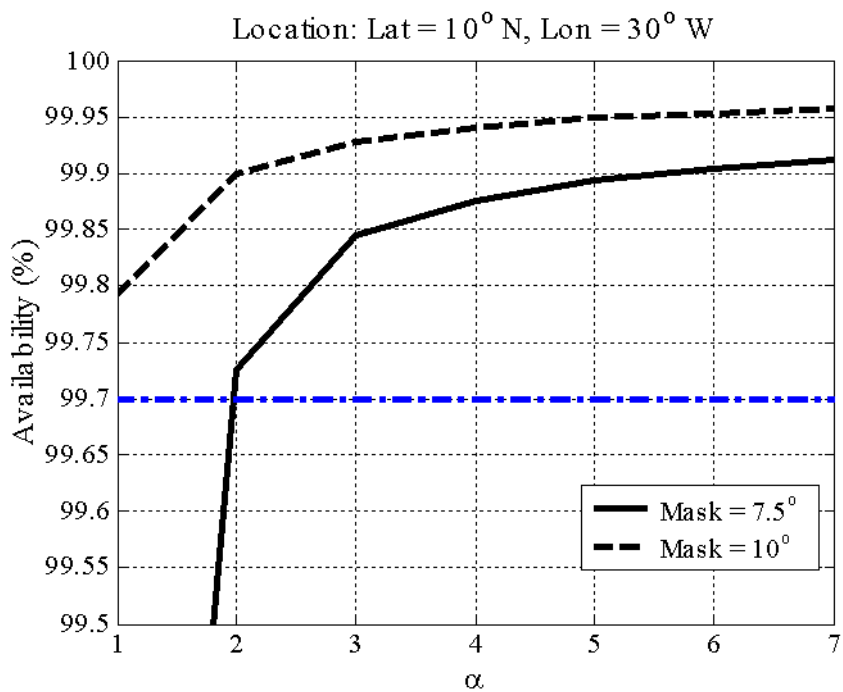


Figure G.3. Availability of Ephemeris Error Detection at Lat = 10° N and Lon = 30° W

APPENDIX H
AVAILABILITY OF IONOSPHERIC ERROR DETECTION FOR DIFFERENT
SHIP LOCATIONS

The availability of ionospheric error detection has been evaluated for the various ship locations—latitude = 20 deg N, longitude = 60 deg -E, latitude = 5 deg N, longitude = -135 deg E and latitude = 10 deg N, longitude = -30deg E. The satellite outage state probability model in Table 3.1, a single difference measurement error standard deviation of 1 cm, and a required missed detection probability of 10^{-4} were assumed in this analysis.

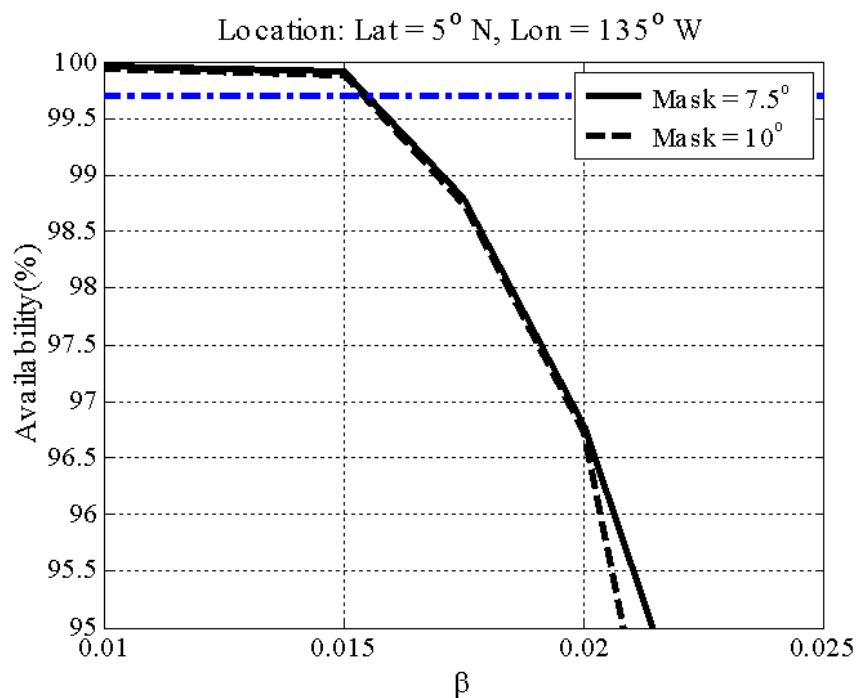


Figure H.1. Availability of Ionospheric Error Detection at Lat = 5° N and Lon = 135° W

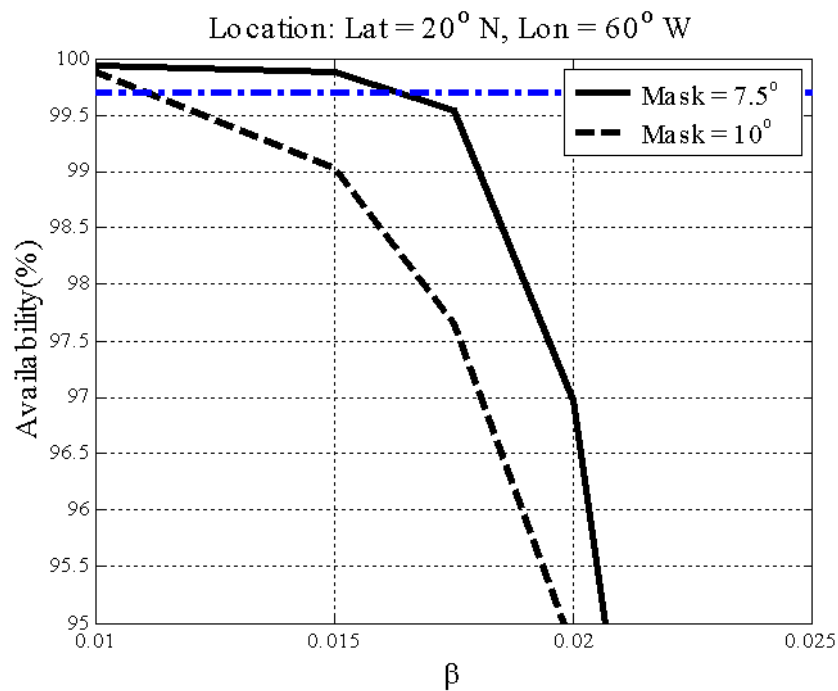


Figure H.2. Availability of Ionospheric Error Detection at Lat = 20° N and Lon = 60° W

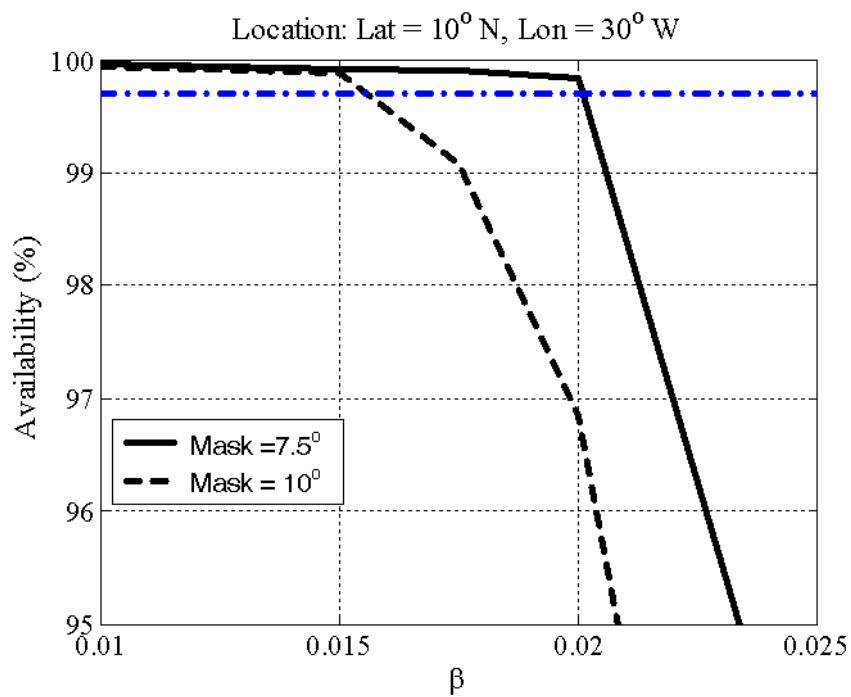


Figure H.3. Availability of Ionospheric Error Detection at Lat = 10° N and Lon = 30° W

BIBLIOGRAPHY

- [AFCS] “Automatic Flight Control Systems AN/ASW-16 and AN/ASW-42, Navy Models A-6E and KA-6D Aircraft,” NAVAIR 01-85 ADA-2-5.1, Naval Air Systems Command, Washington, D.C., 15 July 1974; Rapid Action Change 2, 15 May 1991.
- [Altmayer00] Altmayer, C., “Cycle Slip Detection and Correction by Means of Integrated Systems,” Proceedings of the Institute of Navigation National Technical Meeting, Anaheim, CA, January 2000.
- [Bendat00] Bendat, J. S. and Piersol, A. G., “Random Data: Analysis and Measurement Procedures,” 3rd Ed, John Wiley & Sons, 2000.
- [Beser82] Beser, J., and Parkinson, W.B., “The Application of NAVSTAR Differential GPS in the Civilian Community,” Journal of the Institute of Navigation, Vol. 29, No.2, Summer 1982.
- [Bisnath00] Bisnath, S. B., “Efficient, Automated Cycle Slip Correction of Dual-Frequency Kinematic GPS Data,” Proceedings of the Institute of Navigation GPS 2000, Salt Lake City, UT, September 2000.
- [Blewitt90] Blewitt, G., “An Automatic Editing Algorithm for GPS Data,” Geophysical Research Letters, Vol. 13, No.4, pp 199-202, 1990.
- [Carson86] Carlson, A. B., “Communication Systems,” McGraw Hill, Inc., New York, NY, 1986.
- [Christ03] Christ, J., “Development of an Autonomous Ground Vehicle and Implementation of a GPS-Based Navigation System,” Masters Thesis, MMAE, IIT, Chicago, IL, 2003.
- [Christie99] Christie J. R. I., Ko, P.-Y., Hansen, A., Dai, D., Pullen, S., Pervan, B., and Parkinson, B. W., “The Effects of Local Ionospheric Decorrelation on LAAS: Theory and Experimental Results,” Proceedings of the Institute of Navigation National Technical Meeting 1999 (ION NTM '99), San Diego, Ca, January 1999.
- [Cohen93] Cohen, C. E., Pervan B., Cobb, H. S., Lawrence, D., Powell, J. D., and Parkinson, B. W., “Real-Time Cycle Ambiguity Resolution using a Pseudolite for Precision Landing of Aircraft with GPS,” Second International Conference on Differential Satellite Navigation System (DSNS-93), March 30-April 2, 1993, Amsterdam, The Netherlands.

- [Doherty97] Doherty, P. and Gendron, P. J., "The Spatial and Temporal Variations in Ionospheric Range Delay," Proceedings of the Institute of Navigation GPS 1997(ION GPS97), Kansas City, Mo, September 1997.
- [Gao99] Gao, Y. and Li, Z., "Cycle Slip Detection and Ambiguity Resolution Algorithms for Dual-Frequency GPS Data," Marine Geodesy, Vol. 22, No. 4, pp 169-181, 1999.
- [Gelb74] Gelb, A., "Applied Optimal Estimation," MIT Press, Cambridge, MA, 1974.
- [Gratton04] Gratton, L., Pervan, B., and Pullen, S., "Orbit Ephemeris Monitors for Category I LAAS," Proceeding of the IEEE Position, Location, and Navigation Symposium (PLANS '2004), Monterey, CA, April 2004.
- [Hatch82] Hatch, R. R., "The System of Code and Carrier Measurements," Proceedings of the Third Internal Geodetic Symposium on Satellite Doppler Positioning, Las Cruces, NM, February 1982.
- [Hwang99] Hwang, P. Y., McGraw, G. A., and Bader, J. R., "Enhanced Differential GPS Carrier-Smoothed Code Processing using Dual-Frequency Measurements," NAVIGATION: Journal of the Institute of Navigation, Vol. 46, No. 2, 1999.
- [JPALSTPWG] JPALS Test Planning Working Group, "Architecture and Requirements Definition: Test and Evaluation Master Plans for JPALS," January 19, 1999.
- [Kalafus87] Kalafus R. M., "Receiver Autonomous Integrity Monitoring of GPS", Project Memorandum DOT-TSC-FAA-FA-736-1, U.S. DOT Transportation System Center, Cambridge, MA, 1987.
- [Lawrence96] Lawrence, D., "Aircraft Landing using GPS: Development and Evaluation of a real Time System for Kinematic Positioning using the Global Positioning System," Stanford University Ph.D. Dissertation, Department of Aeronautics and Astronautics, 1996.
- [Lee95] Lee, Y., "New Techniques Relating Fault Detection and Exclusion Performance to GPS Primary Means Integrity Requirements", Proceedings of the Eighth International Technical Meeting of the Satellite Division of the Institute of Navigation, Palm Springs, CA, September 1995.
- [Luo02] Luo, M., Pullen, S., Akos, D., Xie, G., Datta-Barua, S., Walter, T., and Enge, P., "Assessment of Ionospheric Impact on LAAS Using WAAS Supertruth Data," Proceedings of Institute of Navigation's Annual Meeting, Albuquerque, NM, June 2002

- [MASPS98] “Minimum Aviation System Performance Standards for The Local Area Augmentation System,” RTCA Paper No. 037-98/SC159-778, February 1998.
- [Mathieu02] Mathieu, J., “Development of a GPS-Based Navigation and Guidance System for an Automated Ground Vehicle,” Masters Thesis, MMAE, IIT, Chicago, IL, December 2002.
- [Misra01] Misra, P. and Enge, P., “Global Positioning System Signals, Measurements, and Performance,” Lincoln, MA: Ganga-Jamuna Press, 2001.
- [ORD] “Operational Requirements Document (ORD) for Joint Precision Approach and Landing System (JPALS),” USAF 002-94-I.
- [ORDLAAS] “Operational Requirements Document (ORD) for Local Area Augmentation System (LAAS),” Satellite Navigation program Office, Federal Aviation Administration, February 28, 1995.
- [PALC] “Precision Approach and Landing Capability Joint USAF-USN Mission Need Statement,” USAF 002-94.
- [Parkinson88] Parkinson B. W. and Axelard, P., “Autonomous GPS Integrity Monitoring Using the Pseudorange Residual,” Navigation: Journal of the Institute of Navigation, Vol.35, No.2, pp. 255-274, 1988.
- [Parkinson96] Parkinson, B. W., Spilker, J. J., and Axelrad, P., “Global Positioning System: Theory and Applications,” AIAA Progress in Aeronautics and Astronautics, Vol. 163-4, Washington, DC, 1996.
- [Pervan96] Pervan, B., “Navigation Integrity for Aircraft Precision Landing using the Global Positioning System,” Stanford University Ph.D. Dissertation, Department of Aeronautics and Astronautics, 1996.
- [Pervan98] Pervan, B. and Parkinson, B. W., “Autonomous Fault Detection and Removal Using GPS Carrier Phase,” IEEE Transactions on Aerospace and Electronic Systems, Vol.34, No.3, July 1998.
- [Pervan01] Pervan, B. and Chan, F.-C., “System Concept for Cycle Ambiguity Resolution and Verification for Aircraft Carrier Landings,” Proceedings of the Fourteenth International Technical Meeting of the Satellite Division of the Institute of Navigation, Salt Lake City, UT, September 2001.

- [Pervan03a] Pervan, B. and Chan, F.-C., "Detecting Global Positioning Satellite Orbit Errors Using Short-Baseline Carrier-Phase Measurements," Journal of Guidance, Control, and Dynamics, Vol.26, No.1, January-February 2003.
- [Pervan03b] Pervan, B., Chan F.-C., Gebre-Egziabher D., Pullen, S., Enge, P., and Colby, C., "Performance Analysis of Carrier-Phase DGPS Navigation for Shipboard Landing of Aircraft," Navigation: Journal of the Institute of Navigation, Vol. 50, No.3, Fall 2003.
- [Romrell95] Romrell, G., Brown, R., Johnson, G., and Kaufman, D., "FAA/FEDSIM-E-System Cat IIIB Feasibility Demonstration Flight Test Preliminary Results," Proceedings of the Institute of Navigation GPS 1995 (ION GPS95), Palm Springs, CA, September 1995.
- [Spilker94] Spilker, Jr., J.J., "Satellite Constellation and Geometric Dilution of Precision," Global Positioning System: Theory and Applications, Vol. I, pp. 177-208, AIAA, 1994.
- [SPS] "Global Positioning System Standard Positioning Service Performance Standard," October 2001.
- [Sturza88] Sturza, M. A., "Navigation System Integrity Monitoring Using Redundant Measurements," Navigation: Journal of the Institute of Navigation, Vol. 35, No. 4, Winter 1988-89.
- [Teasley80] Teasley, S. P., Hoover, W. M., and Johnson, C. R., "Differential GPS Navigation," Proceedings of Position, Navigation, and Location Symposium (PLANS 80), Atlantic City, New Jersey, December 1980.
- [Teunissen98] Teunissen, P., Odijk, D., and Joosten, P., "A Probabilistic Evaluation of Correct GPS Ambiguity Resolution," Proceedings of the Tenth International Technical Meeting of the Satellite Division of the Institute of Navigation, Nashville, TN, September 15-18, 1998.
- [Van Grass93] Van Grass, F., Diggle, D., and Hueschen, R., "Interferometric GPS Flight Reference/Autoland System," Proceedings of the Institute of Navigation National Technical Meeting 1993 (ION NTM 93), Salt Lake City, UT, September 1993.
- [Walter95] Walter, T., and Enge, P., "Weighted RAIM for Precision Approach," Proceedings of the Institute of Navigation GPS 1995 (ION GPS95), Palm Springs, CA, September 1995.

- [Waters01] Waters, L. J., Sousa, P., Wellons, L., Colby G., Weir, J., and Taylkor, J. F., "Test Results of an F/A-18 Automatic Carrier Landing Using Shipboard Relative GPS," Proceedings of Institute of Navigation's Annual Meeting, Albuquerque, NM, June 2001
- [Wu93] Wu, J.T., Wu, S. C., Hajj, G.A., Bertiger, W.I., and Lichten, S.M., "Effects of Antenna Orientation on GPS Carrier Phase," Man. Geodetica 18, pp. 91-98, 1993.